Non-uniform Emission Studies of a Magnetron Injection Gun

by

Chad D. Marchewka

B.S. (ECE), University of Wisconsin – Madison (2003)

Submitted to the
Department of Electrical Engineering and Computer Science
in partial fulfillment of the requirements for the degree of

Master of Science
at the
MASSACHUSETTS INSTITUTE OF TECHNOLOGY

February 2006

Signature of Author ....
Department of Electrical Engineering and Computer Science
17 January 2006

Certified by ....

Senior Scientist, Department of Physics
Thesis Supervisor

Accepted by ....
....
Smith
Chairman, Committee on Graduate Students
Department of Electrical Engineering and Computer Science

Non-uniform Emission Studies of a Magnetron Injection Gun

by

Chad D. Marchewka

Submitted to the Department of Electrical Engineering and Computer Science on
17 January 2006, in partial fulfillment of the
requirements for the degree of
Master of Science

Abstract

This thesis investigates the experimental measurement and theoretical simulation of the effects of azimuthal emission non-uniformity of a 96 kV, 40 amp magnetron injection gun (MIG) used in a gyrotron. The accomplishments of this thesis include: Experimental measurement of the azimuthal emission non-uniformity of the MIG gun; Simulation of the beam quality of the MIG gun using MICHELLE 3-D, the first simulation of a MIG electron beam with azimuthal non-uniformity; Benchmarking the MICHELLE 3-D code to other established gun optics codes; Evaluation of the effects on the velocity spread and pitch factor of azimuthal non-uniformity in the MIG gun, showing that the direct effect on the beam quality is very small; Design, fabrication, and testing in the gyrotron of a capacitive probe system divided into four quadrants to measure azimuthal asymmetries of the electron beam; Use of the capacitive probes to measure low-frequency (100 - 160 MHz) oscillations on the beam, the first measurement of such oscillations in a microsecond pulse length gyrotron; First results on testing a new MIG cathode for emission non-uniformity using a special test chamber built by Calabazas Creek Research. This research will contribute to our understanding of the properties of intense electron beams produced by MIG guns in high-power gyrotrons.

MIG's are widely used in gyrotron oscillators and amplifiers for fusion applications to create a beam of gyrating electrons generally operating in the temperature limited regime of emission. Due to this dependence on the temperature of the cathode, variation of the emitter surface temperature will result in inhomogeneous emission. Non-uniform emission is attributed to a deviation in the cathode work function as well. Studies have shown this inhomogeneous beam current density can lead to increased mode competition and velocity spread contributing to an overall decreased efficiency of the gyrotron. This research focuses on the effects on velocity spread and in turn the efficiency of the device from non-uniform current emission.

Initially, we measured experimentally the detailed azimuthal non-uniformity profile of an existing 110 GHz gyrotron oscillator at MIT. Using a rotating collector current probe the current density of different emitter angles was extracted. These results agreed fairly well with previous measurements of Anderson et al. This non-uniformity profile was then used with a 3-D simulation code to do the first complete 3-D model from the cathode to the cavity of a MIG. In order to investigate these effects of beam non-uniformity with simulation, we use MICHELLE 3-D developed by SAIC. MICHELLE 3-D has been benchmarked to MICHELLE 2-D and EGUN in the case of a uniform beam. The non-uniform beam measurements are entered into MICHELLE and results are computed at four different azimuthal quadrants of different current densities and for the overall beam, giving special attention to the differences in the beam pitch factor and perpendicular velocity spread. MICHELLE found azimuthal non-uniformity to be a fairly small effect on the overall beam quality.

Concurrently with the MICHELLE 3-D simulations, segmented pitch factor probes are implemented to measure the pitch factor in the four azimuthal quadrants. In an attempt to compare with MICHELLE's results, these four capacitive probes measure the induced image charge of different azimuthal sections of the electron beam, enabling an estimation of differences in the pitch factor between quadrants. Unfortunately, the experimental error is found to be quite high (±15%) rendering differences in the pitch factor to be contained within the error boundaries.

Though the capacitive probes are found to have too much error for adequate resolution of the pitch factor, they are also used to discover the first observations of low-frequency oscillations in a short pulse MW gyrotron. These frequencies, from 100-160 MHz, are found to be dependent on the beam parameters such as the beam voltage, current, magnetic field, and magnetic compression ratio. The frequency range is remarkably close to the frequency of an electron in the adiabatic trap and the experimental as well as the predicted theoretical oscillation behavior of trapped electrons are discussed.

Last, initial progress has been made to test three new cathodes on the Calabazas Creek Research cathode tester. This tester is a dedicated test stand for azimuthal non-uniformity able to obtain a measurement directly at the cathode instead of at the collector end of the device. The setup procedure and results on the first cathode test for the 96 kV, 40 amp gun are reported and future tests are summarized.

Thesis Supervisor: Richard J. Temkin
Title: Senior Scientist, Department of Physics

Acknowledgements

This thesis represents the product of two years of research under the guidance and help of so many people. Without their knowledge, patience, and inspiration, the work presented here would not have been possible.

First and foremost, I would like to thank my thesis supervisor and mentor Rick Temkin. Rick has been a constant source of encouragement and knowledge since my first time meeting him. With an extraordinary expertise in experimental and theoretical research, he has built the gyrotron program at MIT with determination to make significant advances to the field and doing so with a particular interest in teaching the next generation of vacuum device engineers and scientists. A constant advocate of education, he always finds time for his students despite his vast responsibilities and limited time. I would also like to thank my previous undergraduate research advisor, Professor John Booske for initially exposing me to vacuum electronics and for three great years of learning and research at the University of Wisconsin.

In addition to the help of my advisors, none of my research would have been possible without the exceptional scientists in my research group. I could thank every person in my group for at different times providing me with some sort of help or advice. Though incomplete, I will mention just a few of them here: Jagadishawar Sirigiri for helping me with pretty much everything during my time at MIT. There really isn't anything he doesn't know. Eunmi Choi for running the experiments with me and providing constant advice and discussion. Roark Marsh for reminding me what physics is and just how awesome it can be in our numerous office exchanges. Michael Shapiro for his help and expertise in theory and subtle humor. Colin Joye for his knowledge of

MatLab and advice on classes. Jim Anderson for initially teaching me how to run the gyrotron and guidance about graduate life in general. And of course, Ivan Mastovsky and Bill Mulligan in the gyrotron lab. Without their help, nothing in lab would ever get done. Also, much thanks to John Petillo of SAIC, Inc. for all his guidance in the use of MICHELLE 3-D.

Last, I would like to thank my friends and family. Throughout my life, I have been lucky to have very supportive parents, Steve and Debra Marchewka, and a brilliant sister Jeanne. They have pushed me to excel while giving me the freedom and opportunity to pursue what interests me. To my girlfriend Kate, who has always been there, and always believed that I can do anything. To my friends who have provided me with support and inspiration in science and life in general- Pete, Tom, Kyle, Luke, John, Tony, Alex, Amy, Manas, Mike, and countless others....thanks.

For M.K.K

Contents

List of Figures

List of Tables

Chapter 1

Introduction

1.1 The Legacy of High Power Microwaves

The distinguished beginnings of vacuum electron devices began as early as 1875 when G.R. Carey invented the phototube [1]. Three years later Sir William Crookes invented an early precursor of the cathode-ray tube. Most notably though is the inadvertent invention of the world's first diode by Thomas Edison [2]. Edison found that by putting a piece of metal between two glowing filaments of an incandescent bulb, current between the two filaments would be hindered. Current would only flow from the positive side of the current to the metal and not from the negative. This so called "Edison Effect" was the beginning of vacuum tube science and laid the foundation for microwave and solid state diodes that over the next 120 years would revolutionize technological progress.

Throughout the late 19th and early 20th centuries, many advances were made in the field of vacuum devices, but it wasn't until the Second World War that the potential of vacuum electron devices (VEDs) was truly exploited by way of the cavity magnetron radar [3]. The cavity magnetron, most notably developed in early 1940 at the University of Birmingham, United Kingdom [4], was extremely sought after for mountable radar systems that went on to make a considerable impact on the outcome of the war. The magnetron along with the invention of the klystron oscillator and amplifier by the Varian brothers [5] in 1939 and the Traveling Wave Tube Amplifier (TWT) in the early 1940's revolutionized high power microwave technology.

During the 1950's, adding global conflict continued to emphasize VED technology development producing other notable slow-wave devices such as the backward wave oscillator (BWO) [6]. Fast-wave devices such as the ubitron [7], the free electron laser [8], and perhaps the most significant fast-wave device, the electron cyclotron maser, were also discovered. These fast-wave devices were based upon the principle of coherent radiation from oscillating electrons and allowed for much higher order modes and frequencies. The constant trend in the development of microwave devices pushed for higher frequency and power. This trend essentially secured the existence for vacuum tube technology throughout the second half of the 20th century and well into the 21st century.

Beginning in the 1960s, VEDs became under increasing competition from newly developed solid-state transistors. Soon vacuum diodes were being replaced with junction transistors in almost every kind of electronic device. There was, however, one regime that solid-state transistors could not match: high power and frequency. A solid-state device by the same nature that allows it to be compact and easily manufactured also creates limitations on the efficiency and heat load that can be maintained. Since a solid-device consists of electrons diffusing through a solid lattice, much of the electrons' kinetic energy is lost due to collisions with the lattice [4], converting a considerable portion of its energy into heat that must be dissipated by the device. On the other hand, vacuum tubes are essentially collisionless, not losing electron inertial energy to heat, and thus can be made with very high efficiency and at very high powers. With each year the gap between needed microwave sources and amplifiers and the state of the art solid-state devices continues to widen. As frequencies continue to push further into the millimeter regime (.3 to 300 GHz) and as power levels continue to rise, solid-state no longer has an advantage over VEDs. Vacuum devices, a technology over 100 years old, have survived simply because it is the only device to produce what other technologies cannot: high power millimeter wave microwaves. The intrinsic high efficiency of vacuum tubes has enabled them to remain a pervasive force in the field of microwave technology.

The maturity of VEDs in the 60's and 70's led to hybrid devices such as the twystron [9] and improvements upon existing technology such as Tunable BWO's [10]. This time period also led to an emergence of many applications for high power microwaves. In the area of national defense, VEDs were incorporated into military and civilian radar systems, missiles, electromagnetic countermeasures (ECM), and decoys. High-energy physics was made possible with powerful klystrons to supply linear accelerators with RF energy [11]. For instance, the Stanford Linear Accelerator completed in 1967, uses 250 klystron amplifiers to provide 65 MW of peak S-band power. Energy research was also fueled by the continuing advancement of vacuum electronics, most extensively for thermonuclear fusion. With progression of the electron cyclotron maser in the USSR in the early 70s, high power microwaves were used to superheat plasma for controlled fusion experiments [12], [13]. The electron cyclotron maser, commonly referred to as the gyrotron, was then and remains today as the most efficient, effective, and technologically feasible device for thermonuclear plasma fusion heating via electron cyclotron resonance heating. The cyclotron resonance affords very strict control over heating particular regions of plasma. Gyrotrons are one of few devices capable of producing the high frequency (>100 GHz) and power (several MW CW) necessary for controlled thermonuclear fusion to occur.

New applications continued to drive the demand for millimeter wave frequency sources and amplifiers propelling VEDs to new levels throughout the 80's and 90's. For longer life, efficiency, reliability, TWT's became increasingly important for satellite communications [14]. Proposals for the Next Linear Collide (NLC) [15] and the superconducting cavity collider Tesla [16] have spurred development of higher power and multi-beam klystrons [17, 18] Gyro-devices became increasingly valuable for producing frequencies in excess of 90 GHz for a variety of purposes. Though the gyrotron family initially found success for electron cyclotron heating in the 70's, soon other applications followed as the physics of gyrotrons were better understood and the range of available frequencies continued to climb. The Naval Research Lab (NRL) developed a space radar prototype system [19] called WARLOC based on a 94 GHz gyro-twt. The Air Force Research Lab (AFRL) has initiated a program called Active Denial [20] which uses a gyrotron to produce non-lethal microwaves to deter unruly adversaries from an appreciable distance. The National Institute of Health has been funding gyrotron research for use in Dynamic Nuclear Polarization in conjunction with Nuclear Magnetic Resonance spectroscopy to increase sensitivity by several orders of magnitude. Two distinguished CW gyrotrons resulting from this research at MIT are a 250 GHz gyrotron [21], and the recently tested second-harmonic 460 GHz gyrotron [22]. Gyrotrons have also found other industrial uses in materials processing providing microwave power for annealing, sintering, and curing among others [23]. Last, the driving force behind gyrotron research remains on plasma heating in fusion tokamaks. With the recent approval of the site of the International Thermonuclear Experimental Reactor (ITER), an agreement over twenty years in the making, fusion gyrotron research is poised to continue if not increase in the near future.

High power microwaves have a celebrated history with vacuum electronics. Over the last 100 years, huge strides have been taken in the development of VEDs producing many remarkable results. As of this date, throughout the world there are many prominent universities with well established VED programs. The Multi University Research Initiative (MURI) has provided universities with exceptional funding for the support of graduate students and researchers. In addition, recent intern programs for VED engineers have spurred the interest of many promising undergraduate and graduate students to the field. Through sustained education and research funding with an emphasis on human resource development, the devices will only prove to be more valuable in the future. With continued demand for vacuum products and an industry committed to investing in its future, vacuum tube devices will persist to push the state of the art and in doing so maintain its dominance over the high power microwave regime.

1.2 Summary of Vacuum Devices

All vacuum electron devices produce coherent radiation based upon very similar physics. The underlying mechanism for microwave generation is the radiation of coherent photons from a bunched electron beam. The types of radiation can be split into three distinct categories:

- Transition radiation
- Bremsstrahlung radiation
- Cherenkov radiation

Transition radiation occurs when a charged particle traverses a medium with a varying dielectric constant. The particle and its image charge create an effective dipole with its electric field changing over time. Through this varying electric field, the particle beam will emit coherent electromagnetic radiation.

Bremsstrahlung radiation takes place when a charged particle undergoes acceleration. Sometimes called "stopping" or "braking" radiation, it is often employed in vacuum devices when an electron oscillates around a magnetic field line experiencing centripetal acceleration. Devices incorporating this type of radiation are known as fast-wave devices.

Cherenkov or Smith-Purcell radiation is a result of an electron beam passing through a medium faster than the speed of light in that medium. Devices of this nature incorporate a slow-wave structure such as a grating or helix to slow down the phase velocity of light.

Table 1-1 summarizes the types of radiation and some of their common corresponding vacuum devices. All of these devices have there own specific advantages. For instance, TWT's have the ability for ultra-high bandwidths in excess of two octaves [24] whereas klystrons produce unparalleled efficiency and have demonstrated peak power up to 150 MW [25]. Cyclotron resonance masers on the other hand have the ability to achieve a frequency regime that is otherwise elusive to slow-wave devices. The CRM or gyrotron is the only device presently able to produce significant power for frequencies greater than 50 GHz and all the way to the terahertz level. It is this capability that gives the CRM an indisputable advantage in high power microwaves.

Category	Type of Radiation	Devices
Parametric Devices	Transition	Klystron
Slow-Wave Devices	Cherenkov	Magnetrons Traveling Wave Tubes Backward Wave Oscillators Orotron
Fast-Wave Devices	Bremsstrahlung	Cyclotron Resonance Masers (Gyrotrons) peniotrons CARM's FELs Ubitrons

Table 1-1: Summary of vacuum devices

1.3 The Cyclotron Resonance Maser

The cyclotron resonance maser (eventually called the gyrotron) began with a series of theoretical proposals in the 1950s concluding that oscillating electrons can lock into a phase "sorting out" mode or a "phase-focusing" mode [4] and produce coherent electromagnetic radiation. This initial observation can be attributed to Alfven and Rommell [26] in 1954. Four years later, Twiss discovered that a gyrating beam of electrons in a constant magnetic field would emit coherent radiation from azimuthal bunching [27] in a phase-focusing type mode. This azimuthal bunching was the direct result of the effect of changes to an electron's relativistic mass on its cyclotron frequency of oscillation. At essentially the same time, Schneider [28] and Gaponov [29] independently reported similar findings as Twiss. Pantell achieved experimental validation [30] in 1959 and extensive research in the USSR would eventually lead to the

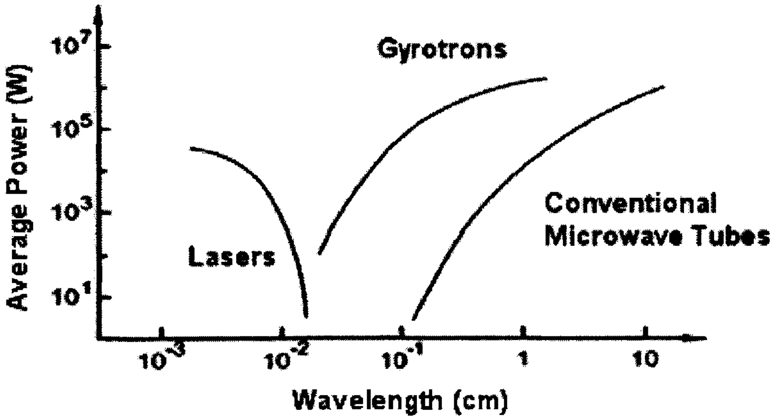

Figure 1-1: Attainable average power capabilities of lasers, gyrotrons, and conventional microwave tubes (Recreated from [32]).

first modern gyrotron configuration in approximately 1965. The actual term "cyclotron resonance maser" was coined in Hirshfield and Wachtel's seminal article in 1964 [31].

The fast-wave mode in the CRM allows it to bridge the gap bordering the limitations of classical devices (conventional microwave tubes) and quantum-mechanical devices (lasers). The CRM accomplishes this by employing the advantages of multiple photon emission per electron like conventional microwave tubes as well as resonance with a higher order mode similar to quantum devices [32]. These advantages allow for high frequency devices in the millimeter and submillimeter gap and at the same time high power and efficiency (Fig. 1-1).

The modern CRM or gyrotron based on the design originating in the USSR consists of an annular electron beam oscillating helically around magnetic field lines. The common gyrotron configuration consists of a Magnetron Injection Gun (MIG), a thermionic cathode, a microwave resonator, a superconducting magnet, and a collector.

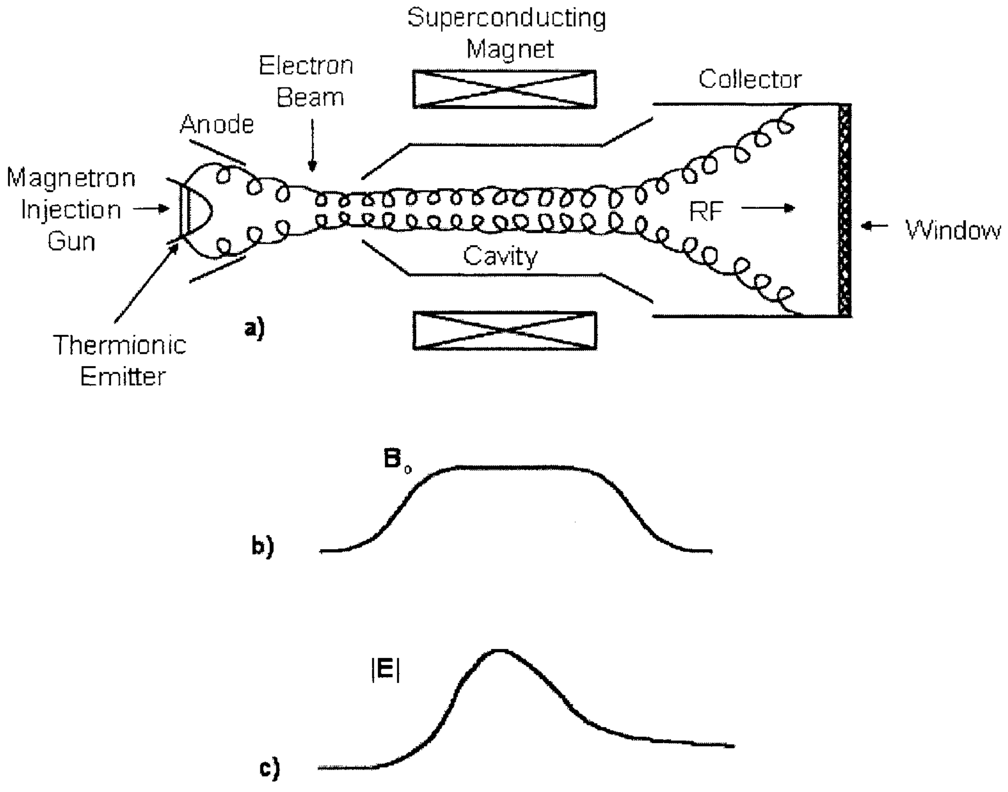

Figure 1-2: General gyrotron schematic and field profiles.

The MIG launches the electron beam from a thin emitting strip on the cathode. The magnetic field force causes the electrons to orbit in helical paths around field lines and compresses the beam to the mode resonant radius. The energy is extracted from the beam in the microwave resonator. Common resonator choices are cylindrical or coaxial and the collector may be depressed relative to the anode to lower the effective voltage. Figure 1-2 shows a typical schematic and field profiles associated with a gyrotron.

Since its conception in the late 1950s, a flurry of development has surrounded the gyrotron. Initial experiments from Pantell's .4 watts at 2.5-4.0 GHz [30] to long pulse or

Institution	Year	Frequency(GHz)	Power	Pulse Duration	Harmonic
CPI [34]	2004	140	.9 MW	30 min	1
IPPMT [35]	2002	165	2.2 MW	short pulse ~ms	1
Gycom [36]	2004	170	1.15 MW	100 ms	1
JAERI [37]	2005	170	.9 MW	9 s	1
MIT [38]	1998	250	25 W	CW	1
IAP [39]	1973	326	1.5 kW	CW	2
MIT [40]	2004	460	8 W	CW	2
Fukui [41]	1998	889	~W	CW	2

Table 1-2: State of the art gyrotrons

CW power levels of over a MW at frequencies ranging from 75-170 GHz [33]. These significant improvements come as the result of advances in manufacturing, materials such as diamond windows, and design tools commonly in the form of computer simulations. Some notable gyrotrons are shown above in Table 1-2.

1.4 Electron Cyclotron Resonance Heating

One of the gyrotron's first applications remains as one of its most important. In the quest for an economical, environmentally friendly, and essentially limitless energy source, developed nations have poured funding into fusion research programs. The basic design shown in Figure 1-3 involves a toroidal structure called a tokamak that confines plasma. The plasma is then superheated to a temperature that atoms will fuse together, releasing an enormous amount of energy in the process. Electron Cyclotron Resonance Heating (ECRH) is the primary heating source for large fusion tokamaks. ECRH via

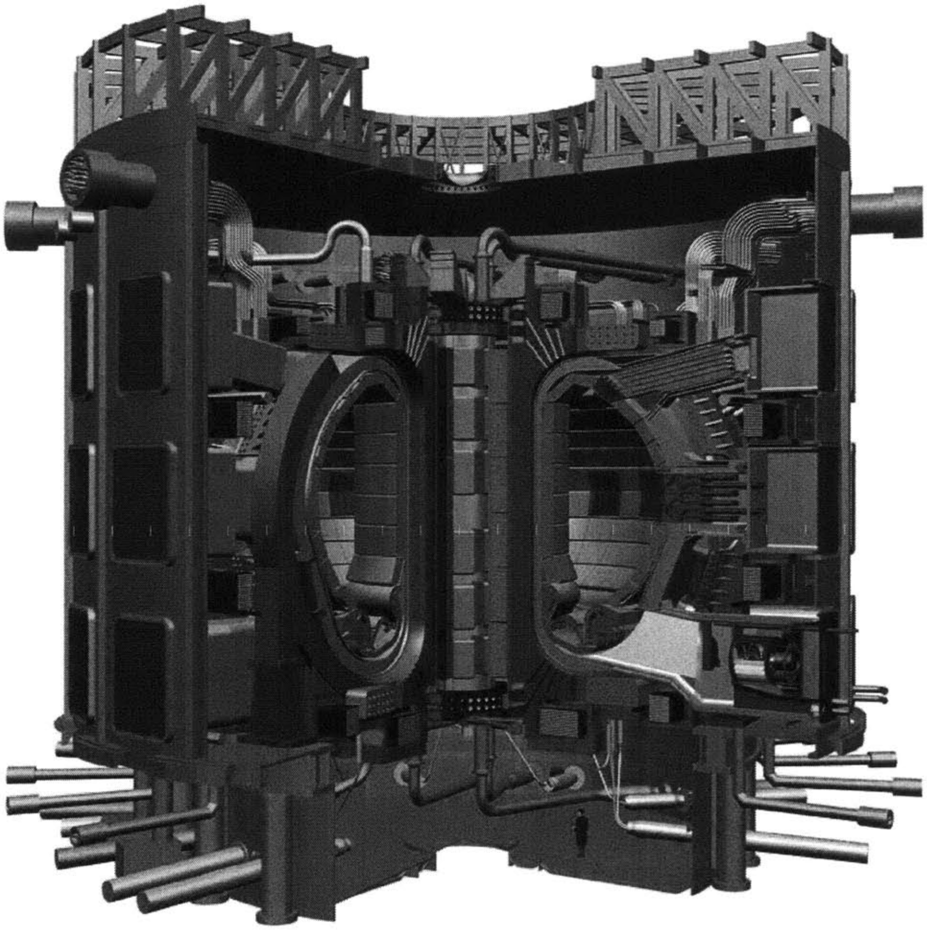

Figure 1-3: The proposed ITER tokamak [43].

gyrotron sources injects microwaves near the cyclotron frequency of the electrons in the plasma, and through collisionless (Landau) damping, the wave transfers a net energy gain to the electrons, thus heating the entire plasma. Tokamaks such as DIII-D General Atomics, JT 60-U JAERI, and the W7-AS stellarator at IPP [42] all rely on ECRH as will the International Thermonuclear Experimental Reactor (ITER) when it's complete circa 2014.

Though expensive, ECRH is arguably the most efficient means of plasma heating. Efficiency truly is the ultimate goal of experimental fusion reactors and in turn the primary goal of high power gyrotron research. As of now, there are no experimental fusion reactors that create net power. The amount of energy extracted is always less than the amount necessary to induce the reaction. Fusion becoming a viable energy source is dependent upon efficient fusion. Necessary improvements are needed in plasma confinement, plasma heating, and energy extraction among others. Since gyrotrons are responsible for plasma heating in tokamaks, gyrotron efficiency is directly related to the overall fusion reactor efficiency. ITER stipulates that overall gyrotron efficiency must exceed 50%. Unfortunately, present performances of high power gyrotrons are quite lower than what ITER demands. Table 1-3 [44] summarizes current progress made in high power long-pulse gyrotrons for ECRH applications. All of them fall below ITER's specifications in not only efficiency, but also in pulse length and most often power. The low efficiency of industrial gyrotrons is the catalyst for the research leading to this thesis on the effect of non-uniform emission on efficiency. Only with a better understanding of the fundamental physics of gyrotron efficiency will fusion become a reality.

Institution	Frequency (GHz)	Cavity Mode	Power (MW)	Efficiency (%)	Pulse Length (s)	Fusion Device
CPI	110	$TE_{22,6}$	1.05	31	5	DIII-D
			0.6	31	10	
	140	$TE_{28,7}$	0.9	34 (SDC)	1800	W7-X
GYCOM	110	$TE_{19,5}$	0.93	36	2	DIII-D
			0.5	35	5	
			0.35	33	10	
	140	$TE_{22,6}$	0.96	36	1.2	ASDEX-U
			0.54	36	3	W7-AS
	170	$TE_{25,10}$	0.85	44 (SDC)	19	ITER
			0.54	40 (SDC)	80	
	140	$TE_{22,6}$	0.8	32	0.8	W7-AS
			0.88	50.5 (SDC)	1	
	158.5	$TE_{24,7}$	0.5	30	0.7	T 10
JAERI	110	$TE_{22,6}$	1.2	39 (SDC)	4.1	JT 60-U
			1	39 (SDC)	5	
	170	$TE_{31,8}$	0.9	43.4 (SDC)	9.2	ITER
			0.5	33 (SDC)	100	
Thales	118	$TE_{22,6}$	0.53	32	5	TORE SUPRA
			0.35	23	97	
	140	$TE_{28,8}$	1	49 (SDC)	12	W7-X
			0.89	41 (SDC)	180	
			0.54	42 (SDC)	940	
			0.26		1300	

Table 1-3: Summary of long-pulse gyrotron development status for ECRH applications.

1.5 Thesis Outline

This thesis research was initiated in an attempt to better understand an azimuthally non-uniform electron beam and accurately ascertain its effect on gyrotron efficiency. As previously stated, gyrotron performance is very important for fusion applications. Pervasive understanding of the factors that affect gyrotron efficiency is imperative for gyrotron operation improvement.

The work presented here is divided into four core chapters. Chapter two is an introduction to the theory describing gyrotron interactions as well as some of the design tools for gyrotron development. Chapter three discusses the measurement of azimuthal current emission variation for two different cathodes. Chapters four and five investigate efficiency effects and azimuthally segmented alpha measurements from the beam non-uniformity study in simulation (chapter four) and experimentally (chapter five). Chapter five also reports the observation of low-frequency oscillations on the gyrotron beam. The thesis is then summarized in chapter 6.

Chapter 2

Theory of Gyrotrons

The theory of gyrotron operation is a very complex but elegant theory with a variety of different analytical and numerical approaches. To provide a comprehensive overview of related gyrotron physics, this chapter will explore a multitude of facets surrounding theoretical gyrotron operation. First a detailed explanation of azimuthal bunching mechanism will be given qualitatively for the electron beam. The relativistic dependence of azimuthal bunching will be shown graphically in simple electron phase space figures as will the dispersion relationship between a cylindrical cavity and the gyrating electron beam. The cyclotron resonance maser interaction is then modeled as a plasma instability revealing the linear kinetic dispersion relationship. Following the kinetic theory summary, the results of a generalized non-linear single particle theory are given, expressing three normalized parameters describing the beam-wave interaction. At the end of the chapter, a thorough description of Magnetron Injection Gun design is presented, beginning with some important design considerations and ending with a synopsis of velocity spread considerations and types of electron emission. This chapter will provide important general information on gyrotron operation necessary for better comprehension of the subsequent chapters. A complete discussion on the physics of gyrotrons can be found in the books of Nusinovich [45] and Kartikeyan [46].

2.1 The Cyclotron Resonance Interaction – A Qualitative Description.

There are several different ways to describe the cyclotron interaction. There are classical methods such as the kinetic plasma instability theory. There is single particle linear and non-linear theory. Also since cyclotron resonance masers are related to quantum mechanical devices, there is also an established quantum theory [47]. However, the most intuitive way to understand the CRM interaction is to look at a phenomenological picture [32], [48], [49] of the CRM bunching mechanism. This physical insight provides a framework in which more abstract analysis can be better understood. Kinetic and single particle theory will then be outlined in sections 2.3 and 2.4.

2.1.1 CRM Resonance

The CRM interaction begins with an electron orbiting its guiding center as shown in Figure 2-1.This single electron beamlet is part of a collection of electrons forming a symmetric annular beam as in Figure 2-2. All of the electrons are initially uniformly distributed in velocity space. For this discussion, we will be concerned with velocity phase angle φ (Fig. 2-1b), which is related to physical space phase by $\varphi = \theta + \pi/2$.

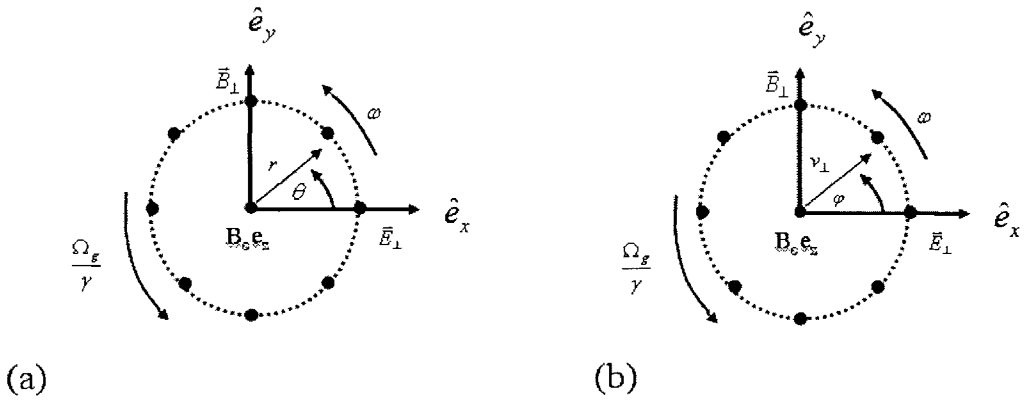

Figure 2-1: a) Uniform distributions of electrons orbiting the guiding center at a distance of the Larmor radius in physical space. b) The same distribution but in velocity space.

At the entrance to the microwave resonator, each electron orbits its guiding center at a constant Larmor radius r_L defined by

$$r_L = \frac{V_\perp}{\omega_c} \tag{2.1}$$

where ω_c is the relativistic cyclotron frequency determined by

$$\omega_c = \frac{qB}{\gamma m_e} \tag{2.2}$$

and γ is the relativistic mass correction factor related to the velocity by

$$\gamma = \frac{1}{\sqrt{1 - \frac{v^2}{c^2}}} \tag{2.3}$$

where v is the velocity of the electron and c is the speed of light.

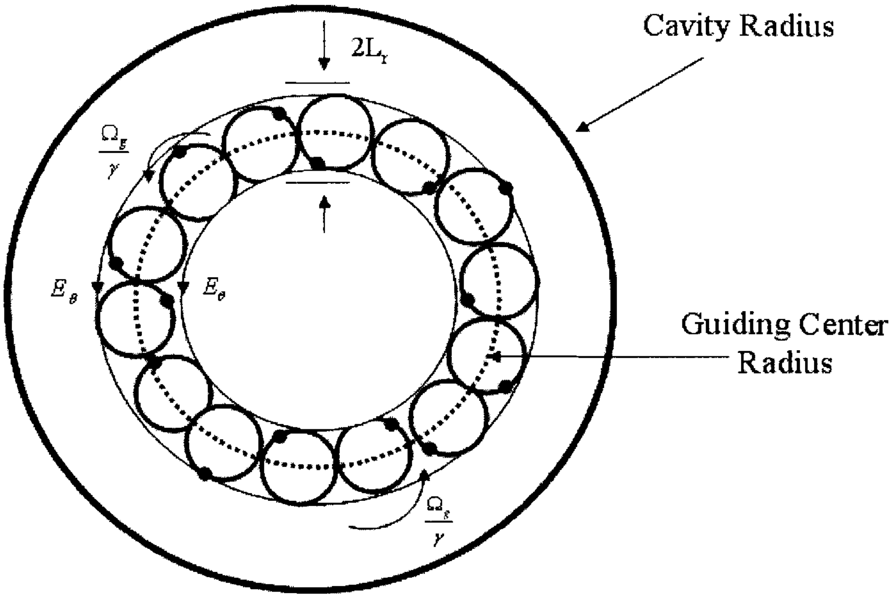

Figure 2-2: Cross section of an annular electron beam in a cylindrical cavity. Each electron orbits its guiding center with an initial uniform distribution in phase space.

Upon entering the microwave resonator, each electron will experience a force from the resonator's transverse electric field and will either gain or lose energy depending on its velocity phase. The quantity of importance here is the rate of change in the electron kinetic energy given by the derivative of the energy equation

$$\frac{d}{dt}W = -e\mathbf{v}_\perp \cdot \mathbf{E}_\perp \tag{2.4}$$

Equation 2.4 governs whether an electron will either gain or lose energy depending on its direction of transverse velocity. $\mathbf{v}_\perp \cdot \mathbf{E}_\perp < 0$ will gain energy from the wave while $\mathbf{v}_\perp \cdot \mathbf{E}_\perp > 0$ will lose energy to the wave. If the electric field is characterized as a circularly polarized wave rotating in the same direction as the electrons, substituting

$\mathbf{v}_\perp = v_\perp(\cos\varphi\mathbf{e}_x + \sin\varphi\mathbf{e}_y)$ and $\mathbf{E}_\perp = E_o[\cos(\omega t - k_z z)\mathbf{e}_x + \sin(\omega t - k_z z)\mathbf{e}_y]$ into equation 2.4 can be written as [32]

$$\frac{d}{dt}W = -e\mathbf{v}_\perp \mathbf{E}_o \cos(\omega t - k_z z - \phi) \qquad (2.5)$$

Here the phase φ of the electron is determined by $\omega_c t$. Electron cyclotron resonance will occur when the phase of the electron remains in phase with the wave. Taking the derivative of the phase condition of (2.5) one can arrive at the resonance condition defined by

$$\frac{d}{dt}(\omega t - k_z z - \omega_c t) \cong \omega - k_z v_z - \omega_c \cong 0 \qquad (2.6)$$

An electron beamlet orbiting at the resonance condition entering the cavity begins to experience either a decelerating or accelerating force depending on its initial azimuthal phase (Fig. 2-3) due to the transverse electric field ($E_\perp$) of the microwave resonator. Since an electron's cyclotron frequency is related to its energy via equations 2.2 and 2.3 changes in electron energy will affect the cyclotron frequency of the electrons. For instance, test particle electron 1 in the left half of Fig 2-3 ($\mathbf{v}_\perp \cdot \mathbf{E}_\perp < 0$) will increase energy, increase in relativistic mass, decrease its cyclotron frequency and experience a relative phase lag whereas test particle 2 in the right half ($\mathbf{v}_\perp \cdot \mathbf{E}_\perp > 0$) will decrease energy and experience a relative phase advance. Eventually the electrons will tend to bunch at the top of Fig. 2-3 where there is no net energy transfer.

Now this bunching mechanism by itself does not transfer a net amount of energy to the wave. If initially a uniform phase distribution of electrons enters the cavity, an equal number of electrons will be in the energy-losing as will be in the energy-gaining phase.

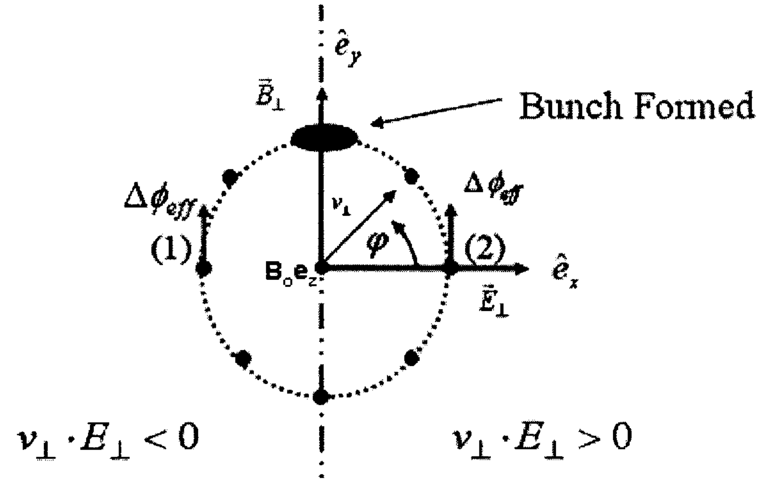

Figure 2-3: Changes in effective phase depending on a particle's velocity phase position. Particles in the left hand side will gain energy and decrease in velocity phase while particles in the right will lose energy to the wave and experience a phase increase.

However, if you slightly detune from the resonance condition such that $k_z v_z + \omega_c \leq \omega$, the electrons will rotate clockwise relative to the wave phase and the bunch will gradually fall into the energy-losing phase resulting in a net transfer of energy to the wave. Figure 2-4 displays the phase bunching as the beam propagates through the cavity.

Thus it is shown that the CRM bunching process is completely a relativistic effect where phase-dependent variations in γ induce azimuthal bunching and a slight detuning of the resonance condition results in a net transfer of energy to the electromagnetic wave. It should be noted that there is also an axial bunching mechanism created from $v_\perp \times B_\perp$ forces that modulate v_z in what is called the Weibel instability [32]. The Weibel instability is the primary mechanism for slow-wave generation, which will be briefly discussed in section 2.3.

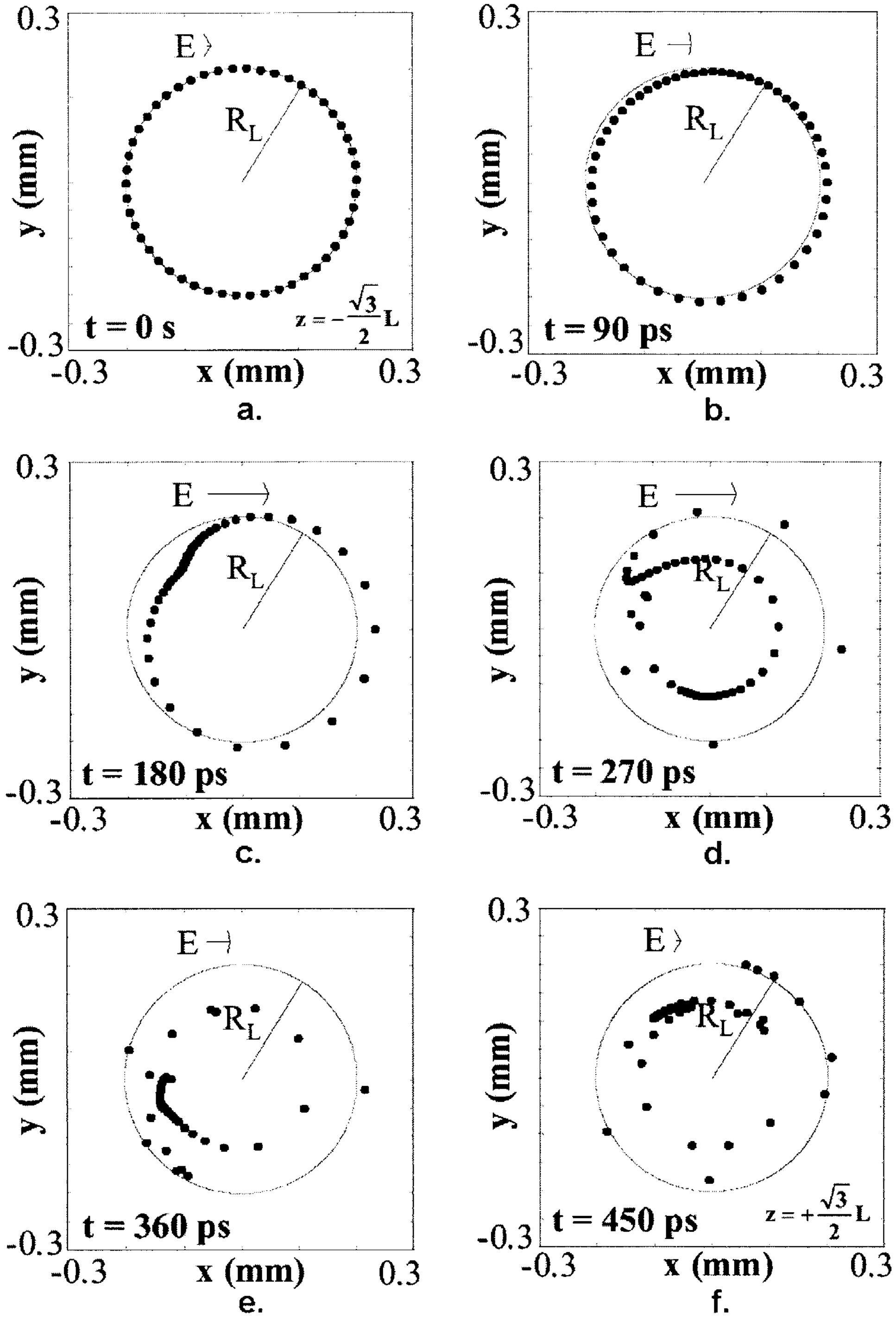

Figure 2-4: Azimuthal phase bunching as a function of time in position space. (Courtesy of Jim Anderson)

2.1.2 Dispersion Diagrams

The most common and simplest gyrotron configuration involves the use of a cylindrical waveguide as the microwave resonator. The gyrating beam interacts with the transverse electric field from a $TE_{m,n}$ mode operating near the cutoff frequency so k_z is very small and there is less of a resonance dependence on the parallel velocity spread Δv_z. The dispersion relationship of a $TE_{m,n}$ mode in a cylindrical cavity is the standard

$$\omega^2 = k^2 c^2 \tag{2.7a}$$

$$k^2 = k_z^{\,2} + k_\perp^{\,2} \tag{2.7b}$$

where

$$k_\perp = \frac{v_{mn}}{r_{cav}} \tag{2.7c}$$

and the cutoff frequency is

$$\omega_{cutoff} = \frac{v_{mn} c}{r_{cav}} \tag{2.7d}$$

Here v_{mn} is the nth root of the Bessel function $J'_m(y)$, m is the theta variation index, and n is the radial variation index.

Overlapping the dispersion relationship of a cylindrical TE waveguide cavity mode along with the resonance condition of the fast cyclotron mode will indicate the regions of strong cavity-beam interactions. As shown in Figure 2-5, several different types of interactions can occur in a gyrotron. Point (a) signifies resonance for a gyromonotron oscillator. Point (b) is a harmonic gyrotron oscillator interaction and point (c) is a backward wave oscillation interaction.

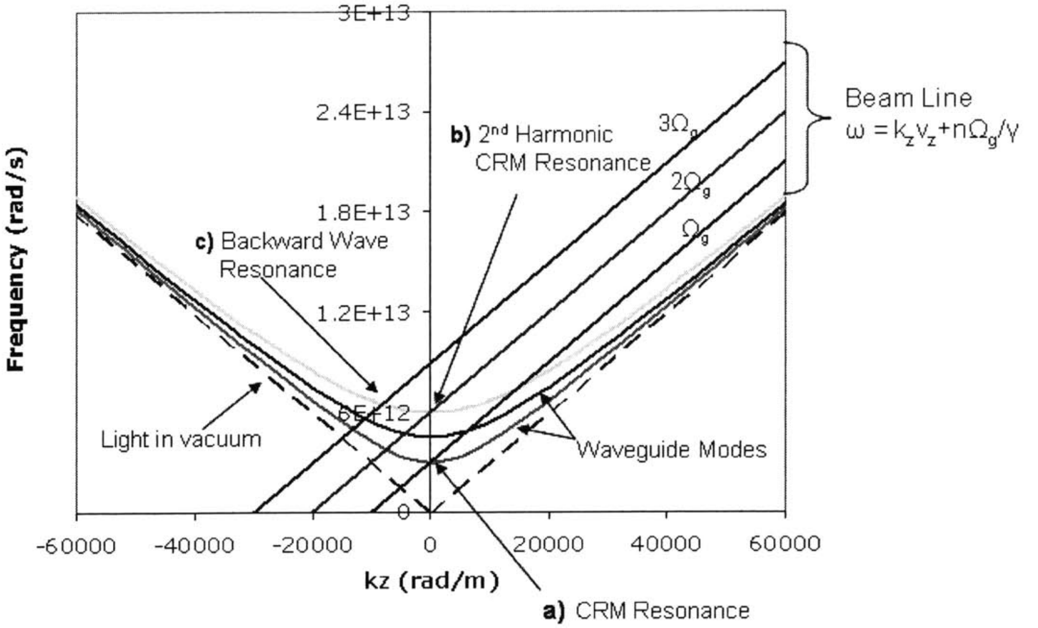

Figure 2-5: Dispersion relationship map of a cylindrical waveguide mode and fast-wave cyclotron modes.

2.2 Kinetic Theory

A more detailed analysis of the cyclotron resonance linear dispersion relationship can be achieved by modeling the CRM interaction as a plasma instability. Plasma immersed in a magnetic field will excite an assortment of waves at or near the cyclotron frequency. Kinetic theory provides a method for thoroughly characterizing the CRM and Weibel instabilities, the two dominant bunching mechanisms in the gyrotron. This derivation is shown in detail by Chu and Hirshfield [50] for a non-neutral plasma and by Fliflet [51] for the specific cases of TE and TM waveguide modes. This section will show a brief setup of the governing equations and the end result following the summaries in [32] and [52].

Starting with an infinite plasma in a uniform magnetic field B_z and of uniform density, the relativistic Vlasov equation is

$$\frac{\partial}{\partial t} f + \mathbf{v} \cdot \nabla f + q(\mathbf{E} + \mathbf{v} \times \mathbf{B}) \cdot \nabla_p f = 0 \tag{2.8}$$

where $f(\mathbf{r},\mathbf{p},t)$ in this case is the electron distribution as a function of physical space, momentum space, and time, ∇ is the gradient in physical space, and ∇_p is the gradient in momentum space. Perturbing the fields by substituting $\mathbf{E} = \mathbf{E}_0 + \mathbf{E}_1$, $\mathbf{B} = \mathbf{B}_0 + \mathbf{B}_1$ **and** $f = f_0 + f_1$ and keeping only first-order terms results in the linearized relativistic Vlasov equation expressed as,

$$\frac{\partial}{\partial t} f_1 + \mathbf{v} \cdot \frac{\partial}{\partial x} f_1 - \frac{e}{c} \mathbf{v} \times B_0 \cdot \frac{\partial}{\partial \mathbf{p}} f_1 = e\left(\mathbf{E}_1 + \frac{1}{c} \mathbf{v} \times \mathbf{B}_1\right) \cdot \frac{\partial}{\partial \mathbf{p}} f_0 \tag{2.9}$$

Along with the relation from Maxwell's equations,

$$\nabla \times \nabla \times \mathbf{E}_1 = -\frac{1}{c^2} \frac{\partial^2}{\partial t^2} \mathbf{E}_1 - \frac{4\pi}{c^2} \frac{\partial}{\partial t} \mathbf{J}_1 \tag{2.10}$$

and the perturbed current,

$$\mathbf{J}_1 = -e \int f_1 \mathbf{v} d^3 p \tag{2.11}$$

equation 2.9 can be solved for f_1 using the method of characteristics [53] and integrating over unperturbed orbits yielding the result,

$$\omega^2 - k_z^2 c^2 = 2\pi \omega_{pe}^2 \int_0^\infty p_\perp dp_\perp \int_{-\infty}^\infty dp_z \frac{f_0}{\lambda} \times \left[\frac{\omega - \frac{k_z p_z}{\gamma m_e}}{\omega - \frac{k_z p_z}{\gamma m_e} - \frac{\Omega_e}{\gamma}} - \frac{p_\perp^2 \left(\omega^2 - k_z^2 c^2\right)}{2\gamma^2 m_e^2 c^2 \left(\omega - \frac{k_z p_z}{\gamma m_e} - \frac{\Omega_e}{\gamma}\right)^2} \right] \tag{2.12}$$

where the plasma frequency $\omega_p^2 = 4\pi n_0 e^2 / m_c$, Ω_c is the non-relativistic cyclotron frequency, and assuming a right-hand circularly polarized wave with fields in the form of

$$\mathbf{E}_1 = E_0\left(\mathbf{e}_x + i\mathbf{e}_y\right)e^{i(k_z z - \omega t)} \tag{2.13a}$$

$$\mathbf{B}_1 = \frac{k_z c}{\omega}\mathbf{e}_z \times \mathbf{E}_1 \tag{2.13b}$$

Equation 2.12 can be further reduced by using the distribution f_0 of electrons drifting in velocity space in which $p_z = p_{z0}$,

$$f_0 = \frac{\delta(p_\perp - p_{\perp 0})\delta(p_z - p_{z0})}{2\pi p_\perp} \tag{2.14}$$

resulting in the reduced equation

$$\omega^2 - k_z^2 c^2 = \frac{\omega_{pe}^2}{\gamma}\left[\frac{\omega - k_z v_{z0}}{\omega - k_z v_{z0} - \frac{\Omega_e}{\gamma}} - \frac{\beta_{\perp 0}^2\left(\omega^2 - k_z^2 c^2\right)}{2\left(\omega - k_z v_{z0} - \frac{\Omega_e}{\gamma}\right)^2}\right] \tag{2.15}$$

From this dispersion relationship it is seen that instabilities occur when $\omega - k_z v_{z0} - \Omega_e / \gamma = 0$ matching to that of the resonance condition of equation 2.6. It can be shown that two dominant and competing instabilities exist for the conditions when $\omega / k_z > c$ (CRM) and $\omega / k_z < c$ (Weibel) and the growth rates ω_{imag} can be found by solving for the roots of ω. As stated before, the fast-wave CRM mechanism is a relativistic effect that is brought about from modulating γ to produce azimuthal bunching while the slow-wave Weibel mechanism modulates v_z resulting in axial bunching. It is also interesting to note that the CRM mechanism is still significantly effective in low voltage regimes where relativistic effects are small [52].

2.3 Single Particle Theory

In a separate approach, a self-consistent non-linear field theory for CRM with a slow varying phase can be found by neglecting collective effects and modeling the interaction as occurring from a single particle [54-57]. In contrast to the collective approach of kinetic theory, single particle theory takes a single particle in the drift region and applies Maxwell's equations and the Lorentz force law. This approach is based upon the generalized pendulum equations [58], [55] and is useful for determining gain and efficiency of a gyrotron operating in a single mode. This synopsis following [57] does not include space charge effects and applies to an electron beam immersed in a magnetic field in a TE cylindrical cavity resonator.

Beginning with the equations of motion, an electron in an electric and magnetic field will experience the Lorenz force and a corresponding change in electron energy denoted by

$$\frac{d\mathbf{p}}{dt} = -\mathbf{eE} - \frac{e}{c}\mathbf{v} \times \mathbf{B} \tag{2.16a}$$

$$\frac{d\xi}{dt} = -e\mathbf{v} \cdot \mathbf{E} \tag{2.16b}$$

where $\mathbf{p} = \gamma m\mathbf{v}$ is the electron momentum, $\xi = \gamma mc^2$ is the electron energy, and γ is the relativistic mass correction factor. The change in electron energy is of primary interest because this quantity demonstrates if the wave loses or gains energy from the beam. This derivation assumes a fixed cavity field profile **E** consisting of a TE_{mp} mode operating near cutoff ($k_z \approx 0$) in a high Q cavity cylindrical cavity. The electric field in such a cavity is expressed as

$$\mathbf{E} = (E_R \hat{R} + E_{\phi_0} \hat{\phi}_0) e^{(i\omega t + \psi)} \tag{2.17a}$$

$$E_R = i(m / k_\perp R) E_0 f(z) J_m(k_\perp R) e^{-im\phi_0} \tag{2.17b}$$

$$E_{\phi_0} = E_0 f(z) J'_m(k_\perp R) e^{-im\phi_0} \tag{2.17c}$$

where $k_\perp = \nu_{mp} / a$, ν_{mp} being the pth zero of the Bessel function of J'_m and a is the cavity radius. By introducing the slow-time phase variable $\theta = \omega t - n\phi$ where n is the harmonic cyclotron resonance number and ϕ is the electron phase and for a mildly relativistic beam with $n\beta_{\perp 0}^2 << 1$ satisfied, equations (2.16) and (2.17) can be combined with further manipulations leading to the single particle gyrotron equations

$$\frac{du}{d\zeta} = 2Ff(\zeta)(1-u)^{n/2} \sin\theta \tag{2.18}$$

$$\frac{d\theta}{d\zeta} = \Delta - u - nFf(\zeta)(1-u)^{n/2-1} \cos\theta \tag{2.19}$$

with the variables $u \equiv \frac{2}{\beta_{\perp 0}^2}\left(1 - \frac{\gamma}{\gamma_0}\right)$ as the relative energy and $\zeta \equiv \pi \frac{\beta_{\perp 0}^2}{\beta_{\parallel 0}} \frac{z}{\lambda}$ as the normalized axial position. Equations (2.18) & (2.19) consist of three normalized parameters defined as

$$\mu \equiv \pi(\beta_{\perp 0}^{2}/\beta_{\parallel 0})(L/\lambda) \qquad \text{(normalized cavity length)} \tag{2.20a}$$

$$F \equiv \frac{E_0}{B_0}\beta_{\perp 0}^{n-4}\left(\frac{n^{n-1}}{n!\,2^{n-1}}\right)J_{m\pm n}(k_{\perp}R_e) \qquad \text{(normalized field amplitude)} \tag{2.20b}$$

$$\Delta \equiv \frac{2(1-n\omega_{c0}/\omega)}{\beta_{\perp 0}^{2}} \qquad \text{(normalized field detuning factor)} \tag{2.20c}$$

where R_e is the radius of the average electron beam gyrocenter and $\beta_{\perp 0} = v_{\perp 0}/c$ is the speed of the electrons at the entrance to the cavity. Total efficiency is then found by relating the beam energy at the entrance of the cavity to the beam energy at the exit by

$$\eta \equiv [\beta_{\perp 0}^{2}/2(1-\gamma_0^{-1})]\eta_{\perp} \tag{2.21}$$

and the perpendicular efficiency $\eta_{\perp} = \langle u(\zeta_{out})\rangle_{\theta_0}$ is found by averaging the relative energy of electrons at the cavity exit over initial phase angles.

For a Gaussian field profile $f(\zeta)$, eqns. (2.18) and (2.19) can be numerically integrated using the Runge-Kutta method on any mathematics software providing a theoretical value of device efficiency.

2.4 The Magnetron Injection Gun

Efficient gyrotron operation is heavily dependent upon the quality of the electron beam. Not only does the beam have to be at a specific radius for optimum beam-wave interaction, but it also needs a large amount of transverse velocity ($v_{\perp}$) as well as very low velocity spread ($\delta v_{\perp}$). Since 1965 [59], [60], magnetron injection guns (MIGs) have been employed in gyrotrons to produce an annular beam of electrons that adhere to these requirements. The following section details the geometry of a MIG and some important design issues involved in the development process.

2.4.1 Analytical Design

Magnetron injection gun design is usually accomplished with the help of gun optics codes. However, the difficulty of the iterative MIG design process necessitates the need for a good first order design before using computer codes to finalize the design. Computer codes will be discussed in section 2.6 after an understanding of the linear MIG design is presented.

Linear analysis is shown following the equations provided by Baird and Lawson [61]. The cross section of the electron beam and the geometrical variables used in this design are show in Figure 2-6. The electron at position **r** gyrates around a magnetic field line. Consequently, the guiding center r_g is locked in physical space in a region of constant magnetic field and the absence of an electric field. As the position of the magnetic field line changes, so will the guiding center radius. This way, gyrotron operators can precisely control beam radius by changing the magnetic field compression.

The design equations are based on the assumption of adiabatic flow and do not take into account the effects of space charge. The adiabatic flow approximation is valid if certain conditions are met in which changes in the magnetic and electric fields are small compared to the physical dimensions traversed by the electrons.

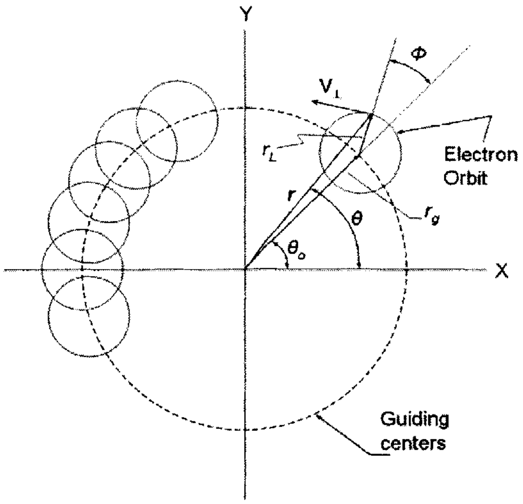

Figure 2-6: Electron beam cross section (courtesy of Colin Joye)

The conditions of adiabatic validity are formulated as,

$$z_L^2\left|\frac{\partial^2\mathbf{B}}{\partial z^2}\right| << \mathbf{B}, \qquad z_L^2\left|\frac{\partial^2\mathbf{E}}{\partial z^2}\right| << \mathbf{E},$$

$$z_L\left|\frac{\partial\mathbf{B}}{\partial z}\right| << \mathbf{B}, \qquad z_L\left|\frac{\partial\mathbf{E}}{\partial z}\right| << \mathbf{E}, \tag{2.22}$$

where an electron travels an axial distance z_L in one cyclotron period. This approximation is valid in Figure 2-7 after the electron beam exits the region of high electric field (z > 10 cm). The adiabatic flow assumption produces an important quantity called the magnetic moment constant that provides the relationship between the electron perpendicular momentum $(p_\perp = \gamma m_e v_\perp)$ and the axial magnetic field $\mathbf{B}_z$ expressed as

$$\frac{p_\perp^2}{2\mathbf{B}} = u = const. \tag{2.23}$$

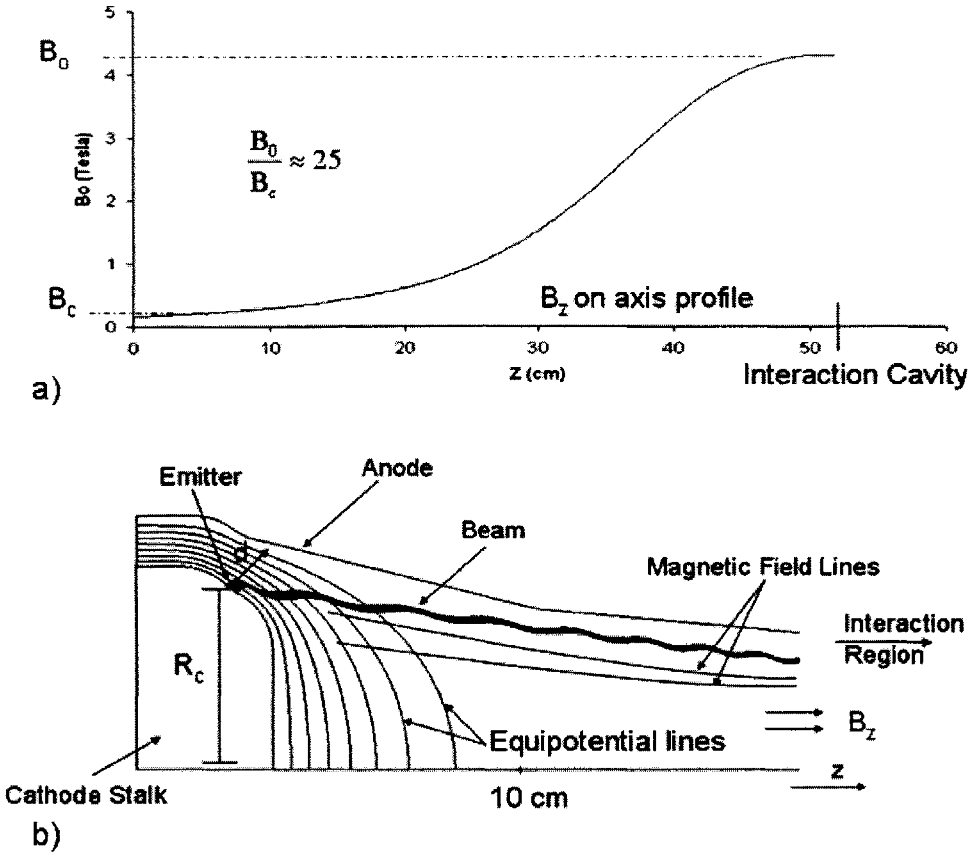

Figure 2-7: a) On-axis magnetic field profile for a 110 GHz gyrotron. b) MIG geometry for a diode gun produced by MICHELLE gun optics code.

Thus as shown in Figure 2-7, when the axial field gets stronger and the magnetic field lines become more compressed, $p_\perp$ increases, and the beam radius decreases since the electrons are fixed to a magnetic field line.

The MIG design process begins with five essential specifications tailored for optimum beam-wave interaction in the resonator cavity. To achieve these pre-determined parameters there are four variables used to achieve an acceptable design. The cathode radius R_c is often the most important variable since the electric field increases with R_c and

Design Parameters		**Design Variables**	
Beam power	**P**	Average Cathode Radius	$\mathbf{r_c}$
Electron energy	γ	Cathode current density	$\mathbf{J_c}$
Cyclotron frequency	ω_c	Cathode angle	φ_c
Average guiding center radius	$\mathbf{r_g}$	Anode and cathode distance	$\mathbf{D_F}$
Ratio of perpendicular to longitudinal velocity	α		

Table 2-1: Design parameters and independent design variables for first-order MIG design.

the current density J_c increases when operating in temperature limited regime. It is necessary to find a cathode radius that gives a low E_c and at the same time a relatively low J_c to be well below the space charge limited current. These parameters and independent variables are found in Table 2-1.

Starting with symmetric electric and magnetic fields and the conservation of momentum

$$(\gamma m_0 r^2 \dot{\theta} - eB_z r^2 / 2) = const. \tag{2.24}$$

where γ is the relativistic mass correction factor, $\dot{\theta}$ is the angular velocity, r is the instantaneous radius of electrons, e and m_0 are the electron charge and mass respectively, and B_z is the axial magnetic field. Equation 2.24 can be transformed to coordinates in the beam drift region of Fig. 2-6 yielding,

$$(\gamma m_0 \dot{\theta} - eB_z / 2) r^2 = (eB_z / 2)(r_L^2 - r_g^2) \tag{2.25}$$

where r_L is the Larmor radius and r_g is the guiding center. Rearranging eqn. 2.24 with the left hand side representing the cathode radius denoted by subscript "c", the interaction guiding center radius by subscript "g", and $\dot{\theta}$ =0 you arrive at

$$\frac{B_0}{B_c} = \frac{r_c^2}{r_g^2 - r_L^2} \tag{2.26}$$

where B_0 / B_c is commonly referred to as the magnetic compression ratio. Assuming $r_L << r_g$, eqn. 2.26 can be rewritten as

$$r_{g_0}^2 B_0 = r_c^2 B_c. \tag{2.27}$$

A similar expression can be derived for the Larmor radius directly from the magnetic moment equation of eqn. 2.23,

$$\gamma_0^2 r_{L_0}^2 B_0 = B_c r_{L_c}^2 \tag{2.28}$$

Taking the differences of both sides of eqn. 2.28 gives the guiding center spread at the interaction expressed as,

$$\delta r_g = \delta r_c \sqrt{\frac{B_0}{B_c}} \tag{2.29}$$

where δr_c is the spread in the difference in cathode radii of emitter electrons.

The drift velocity from the E x B force at the cathode determines the initial perpendicular velocity of the electrons given by

$$v_{\perp c} = \frac{E_c \cos \phi_c}{B_c} \tag{2.30}$$

where ϕ_c is the angle between the cathode electric field and cathode magnetic field. This angle is approximately equal to the slant angle of the cathode in a conically shaped coaxial geometry. E_c here can be approximated by

$$E_c = \frac{-V_a}{r_c' \ln\left(\frac{r_c' + d}{r_c'}\right)} \tag{2.31}$$

where d is the cathode-anode spacing and $r_c' = r_c / \cos\phi_c$. Equation 2.30 can be combined with equation 2.23 to produce the perpendicular velocity in the interaction region in the adiabatic approximation expressed as,

$$v_{\perp 0} = \frac{E_c \cos\phi_c}{B_c \gamma_0} \sqrt{\frac{B_0}{B_c}} \tag{2.32}$$

Note that γ_c is not included here since the electrons start essentially from rest at the cathode.

A complete listing of the design equations can be found in [61] including E_c/E_{max} and J_c/J_L. A good design will incorporate a peak electric field much less than 100 kV/cm and a cathode current density less than 10 A/m^2. The electric field limit is to prevent breakdown and arcing in the gun region while the current density limit is to promote a cathode life on the order of 10^6 hours [62]. In addition, it is advisable to have a cathode angle $\phi_c > 25°$ to create a laminar beam. A laminar beam is one that the electron trajectories do not intersect. Laminar beams have the advantage of reducing the increase of velocity spread from increased beam current. One noteworthy insight from the design equations from Baird and Lawson is that the ratio of the cathode current density to that of the space charge limited is approximately proportional to r_c^5. This is of importance since magnetron injection guns for gyrotron applications usually operate in the temperature-limited regime well below the space charge Langmuir limit J_L. The need to have temperature-limited operation inherently defines a maximum for the cathode radius in any MIG design.

2.4.2 Estimation of Velocity Spread

Velocity spread is possibly the most important parameter that limits high efficiency. To obtain high efficiency, all the electrons need to be oscillating at very similar velocities for optimal bunching. In addition, the velocity spread puts an upper limit on attainable α ($v_\perp / v_\parallel$) values because as α gets upwards of 2, some of the electrons will acquire too much perpendicular energy and will be reflected by the magnetic mirror force. These reflected electrons, even if occurring in small amounts, can severely degrade the overall quality of the beam. Thus it is imperative to have accurate estimates of the velocity spread due to optical spread, thermal spread, and surface roughness.

Electron trajectory optical spread is caused by the geometry of the diode and is most accurately calculated using gun optics codes such as MICHELLE [63] or EGUN [64]. There are also two other important sources of spread arising from thermal differences and surface roughness on the cathode surface. Estimates for thermal and cathode roughness spread at the cathode can be estimated as given by Tsimring [65] as,

$$(\Delta v_\perp)_T = \left(\frac{KT_c}{m_o}\right)^{\frac{1}{2}} \tag{2.33}$$

$$(\Delta v_\perp)_R = \frac{2}{5}\left(\frac{2eE_c R}{m_o}\right)^{\frac{1}{2}} \tag{2.34}$$

where K is Boltzmann's constant, T_c is the temperature at the cathode in degrees Kelvin, m_0 is the electron mass, e is the electron charge, and R is the radius of a hemispherical extrusion from the cathode surface. $(\Delta v_\perp)_T$ and $(\Delta v_\perp)_R$ can be interpreted as the standard deviation of the perpendicular velocity from its respective cause while the actual velocity spread has the form $\Delta v_\perp / v_{\perp avg}$. All of the different causes of spread can be combined using the sum of squares to produce an estimate of the total spread in the form

$$\left(\frac{\Delta v_\perp}{v_{\perp avg}}\right)_{total} = \left[\left(\frac{\Delta v_\perp}{v_{\perp avg}}\right)_T^2 + \left(\frac{\Delta v_\perp}{v_{\perp avg}}\right)_R^2 + \left(\frac{\Delta v_\perp}{v_{\perp avg}}\right)_o^2 + \left(\frac{\Delta v_\perp}{v_{\perp avg}}\right)_x^2 + \ldots\right] \quad (2.35)$$

where subscript "o" corresponds to optical spread and "x" is any other cause of spread such as non-symmetric cathode electric field or other space charge effects. A more detailed explanation and the effects of velocity spread will be discussed in chapter 4.

2.4.3 Electron Gun Codes

The simulation tools used in this thesis center around electron optics finite element codes, in particular MICHELLE [63], EGUN [64], and OMNITRAK [66]. EGUN developed by Herrmannsfeldt at the Stanford Linear Accelerator has long been hailed as the standard 2-D steady state electron gun code. EGUN is a 2-1/2 dimensional code in that it solves for electrostatic and magnetostatic fields in two dimensions and particle trajectories in three dimensions. EGUN has been thoroughly tested and has become the industry benchmark for gun codes. A magnetron injection gun can be adequately modeled in EGUN since it has an axis-symmetric geometry. When emission non-uniformity is included, however, the symmetry is broken and a fully three dimensional code is needed such as OMNITRAK or MICHELLE.

Electron gun codes usually fall into one of two categories: particle-in-cell (PIC) codes or ray-tracing codes. Both categories involve an iterative process solving electrostatic and magnetostatic fields and advancing particles through those fields. The key difference is the order in which these tasks are accomplished. Particle-in-cell codes advance a particle, deposit its charge, and calculate fields each time step whereas ray-tracing codes first calculate the fields for all solution space and then track the particles through the fields. All the codes referenced above are of the ray-tracing type code and will be discussed in the subsequent paragraphs.

All ray-tracing codes follow essentially the same finite element algorithm whether they are two or three dimensions. The only differences are the field calculations, which must be done using three dimensions and clearly the mesh size is much greater in 3-D. The primary equations driving the solution are Poisson's equation and the Lorentz force law defined as,

$$\nabla^2\phi = -\frac{\rho}{\varepsilon} \tag{2.36}$$

$$m_0\frac{d\gamma\mathbf{v}}{dt} = q(\mathbf{E} + \mathbf{v}\times\mathbf{B}) \tag{2.37}$$

where ϕ is the electrostatic potential, ρ is the charge density, ε is the dielectric permittivity, m_0 is the rest mass, $\mathbf{E} = -\nabla\phi$ is the electric field, $\mathbf{v}$ is the electron velocity, and $\mathbf{B}$ is the magnetic field. Initially eqn. 2.36 is solved using the finite difference method to solve for the charge-free electric field solution (Laplace's equation) in the presence of user specified boundaries. Two common boundaries used in gun simulations are Neumann and Dirichlet. Neumann refers to a symmetry condition where the perpendicular electric field is zero at the boundary $(\partial\phi/\partial n = 0)$. The Dirichlet condition

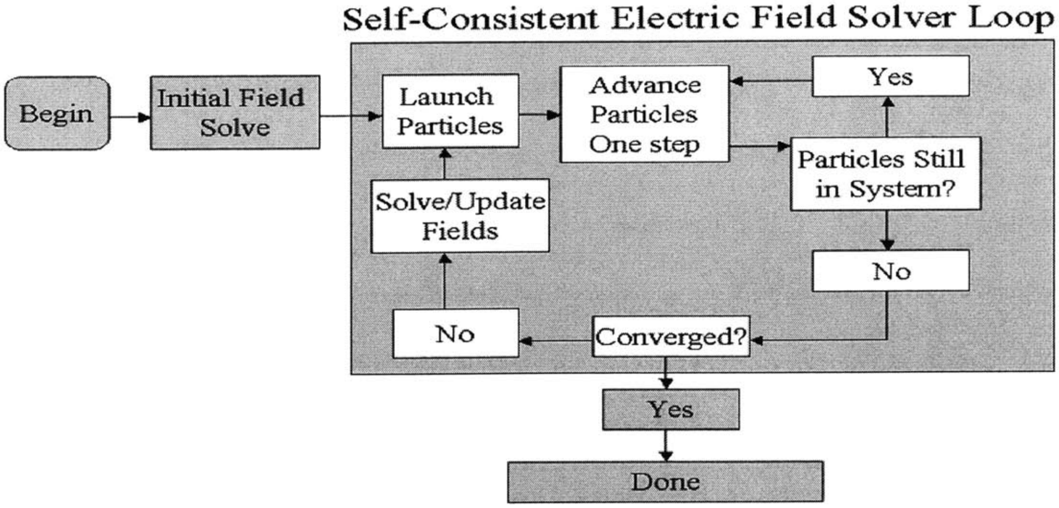

Figure 2-8: Electrostatic field solve algorithm

specifies a potential along the boundary $\phi = V_{const.}$ and is primarily used for conductors. After the initial electrostatic solution, the particles are launched from the emitting surface either by Child's space-charge limiting current density or in this study, with a predetermined current density. Particles are advanced through the mesh at time step intervals following eqn. 2.37 until no particles remain in the system. The program then checks for convergence. If convergence is met, the program is finished. If not, a new cycle is started incorporating the space charge of the particle beam from the previous cycle in the new field calculation of Poisson's equation. The simulation algorithm is summarized in Figure 2-8. This process will continue until adequate convergence is met or the maximum number of user specified cycles is reached.

The magnetic fields are either calculated before the particle run with a separate magnetostatic solver simulating an array of point coils, a polynomial expression for the axial field, $B_z = f(z)$, at $r = 0$, or an on-axis axial field data file. Many of these programs also have the ability to solve the particle magnetic self-fields, which becomes important as the energy of particles reach relativistic levels. If neglecting the self-fields, the magnetic fields only need to be solved for once before running the electrostatic solver. Otherwise, the self magnetic fields must be calculated using Ampere's law for each cycle adding another step to the algorithm in Fig. 2-8.

2.5 Electron Emission

Electron emission from a material surface can be accomplished in a variety of ways. Electrons are trapped within a material held by a potential well called the work function. To emit from any surface, electrons must possess enough energy to overcome the potential well and an electric field to steer them from the surface. There are a variety of emission mechanisms including field, secondary, photoelectric, and thermionic emission.

1) Field Emission

Field emission is a process of pulling electrons from a surface. Accomplishable even at room temperature, field emission devices apply a very high electric field ($>10^6$ V/m) to lower the potential barrier described by the work function. The barrier becomes so low that even electrons without enough kinetic energy to overcome the work function, can escape the surface through a quantum mechanical tunneling effect. This effect theoretically allows for great current densities at all temperatures, but is hindered by the electric field requirement. To achieve such electric fields, most field emitters consist of sharp emitter tips that are fragile and structurally unreliable.

2) **Secondary Emission**

Secondary emission describes the bombardment of an electrode to produce emission. The impacting electrons called the primary electrons cause the emission of several secondary electrons creating a net increase in current. Generally one primary electron will produce several secondary electrons. The number of secondary electrons produced depends on the secondary emission ratio, the primary electron energy, and the angle of bombardment. Problems associated with this self-sustained emission are short cathode life and a susceptibility to contamination.

3) **Photoelectric Emission**

Electrons will emit from a metallic surface upon exposure to electromagnetic radiation above a certain threshold frequency. Above the threshold frequency, the photon energy absorbed by the electrons is sufficient to overcome the work function barrier. This frequency is related to the work function by the relation $E_{phton} = \hbar f > e\phi$ where $e\phi$ is the work function, E is energy, $\hbar$ is Planck's constant, and f is frequency.

4) **Thermionic Emission**

A more common approach than photoelectric emission in vacuum devices is the use of a thermionic cathode. Thermionic cathodes operate under the principle that heating a low work function surface will eventually give bound surface electrons enough thermal energy to escape the potential well and "boil off" from the surface. At all temperatures, every solid has some electrons with energy capable to overcome the work function.

Unfortunately, the percentage of these high-energy electrons is only the tail of the distribution, and emission will be negligible. Heating the surface to the order of 1000° C significantly increases the number of electrons capable of emission. Since magnetron injection guns rely almost exclusively on thermionic cathodes, a brief overview of the emission characteristics of thermionic emission will be provided in forthcoming paragraphs.

From Gilmour [67], the current density of a thermionic cathode at a temperature T is given by the Richardson-Dushman equation expressed as

$$J = A_0 T^2 e^{-\frac{e\phi}{kT}} \tag{2.38}$$

where J is the current density, e is the electron charge, ϕ is the work function, k is Boltzmann's constant, and A_0 is $1.2*10^6$ A/m^2 deg^2. The actual value of A_0 can be determined experimentally and is usually quite lower than $1.2*10^6$. Eqn. 2.38 gives the number of electrons per area per time that can escape the work function at a certain temperature. Modifying eqn. 2.38 to account for the effective lowering of the work function by the addition of an electric field known as the Schottky effect is given by

$$J = A_0 T^2 \exp\left[\frac{-e}{kT}\left(\phi - \left(\frac{eE}{4\pi\varepsilon_0}\right)^{1/2}\right)\right] \tag{2.39}$$

The Schottky effect shows why at fixed temperature the current will continue to increase slowly as the voltage and thus the cathode electric field is increased.

Thermionic emission at low voltages is dominated by what is called the space charge limited regime. In this regime, the emitted electrons create a space charge cloud

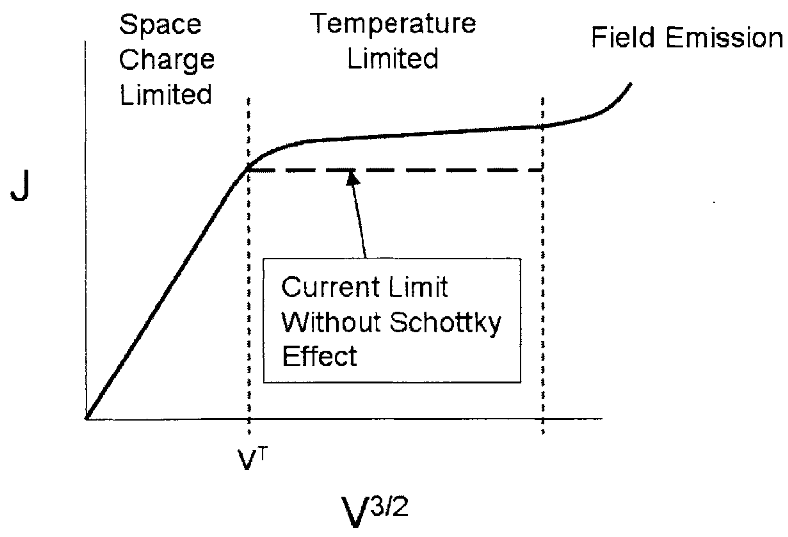

Figure 2-9: Emission regions of a thermionic cathode.

between the cathode and anode neutralizing the electric field. Eventually, as current increases the electron cloud becomes so dense that the potential drops below zero and emission ceases. The equilibrium current density limit referred to as the Child-Langmuir current is expressed for a parallel plate diode by

$$J = \kappa V^{3/2} \tag{2.40}$$

where J is the current density, k is a geometrical constant called the perveance, and V is the voltage. As shown in Fig. 2-9, current will continue to rise in proportion to $V^{3/2}$ until the voltage gets so high that the available electrons described by eqn. 2.38 reach a maximum available current for the cathode temperature. From this point forward, the current will only modestly increase from the Schottky effect until the voltage gets so high that field emission occurs through electron tunneling.

Chapter 3

Experimental Emission Uniformity Profiles

Emission non-uniformity has been a consistent problem for magnetron injection guns. Theoretical studies have shown inhomogeneous beam current density can lead to increased mode competition effectively lowering the efficiency of the device [68]. Other studies show that non-uniformity does little to degrade the beam quality and thus the efficiency unless at extremely high current (>200 A) [69]. Experimentally at MIT, Grimm reports in [70] that diminished gyrotron efficiency resulted from a total failure of half the emitting area. After the cathode was replaced, the efficiency improved. Poor gyrotron performance has also been blamed on non-uniform emission without an investigation into the degree of non-uniformity in other gyrotrons as well [71]. So much uncertainty over the actual effect of beam non-uniformity spotlights the need for a better understanding of the underlying physics of non-uniform emission.

The susceptibility of MIGs to non-uniform emission stems from generally operating in the temperature limited regime of emission. Due to this dependence on the cathode temperature, variation of the emitter surface temperature will result in inhomogeneous emission. Even with good temperature uniformity, non-uniform emission can also result from deviations in the cathode work function [72 -74]. Work function differences on the cathode surface give variant local temperature limited current densities governed by eqn. 2.39 producing the inhomogeneous beam characteristic.

This chapter will focus on obtaining the non-uniformity profile necessary for the upcoming 3-D gun modeling in MICHELLE and the concurrent effort of experimental validation. These results are similar to the experiment by Anderson in [73] but were needed to assure precision of the measured angles for modeling in MICHELLE as well as to provide an updated measurement of the non-uniformity profile. In addition, the preliminary cathode measurements of an identical cathode to the one installed at MIT will be performed at Calabazas Creek Research. The setup and results of this measurement are detailed at the end of the chapter.

3.1 Experimental Gyrotron

The gyrotron used in this experiment operates at a frequency of 110 GHz in the $TE_{22,6}$ mode designed for an output power of 1.5 MW. The experimental gyrotron was developed concurrently with an industrial version at Communications Power Industries (CPI). CPI designed the microwave cavity using the MAGY code [75] while the diode magnetron injection gun was designed by Dr. Steven Korbly of MIT by way of a parameter design study with the EGUN gun-optics code. Table 3-1 lists the gyrotron design parameters and a schematic showing the layout of the gyrotron in axial

Frequency	110 GHz
Output Power	1.5 MW
Beam Voltage	96 kV
Beam Current	40 A
Mode	TE22,6
Pitch Factor	1.4
V_{Perp} Spread	1.8%
Pulse Length	3 us
Cavity B Field	4.3 T
Compression	25

Table 3-1: 110 GHz gyrotron MIG design and operating parameters.

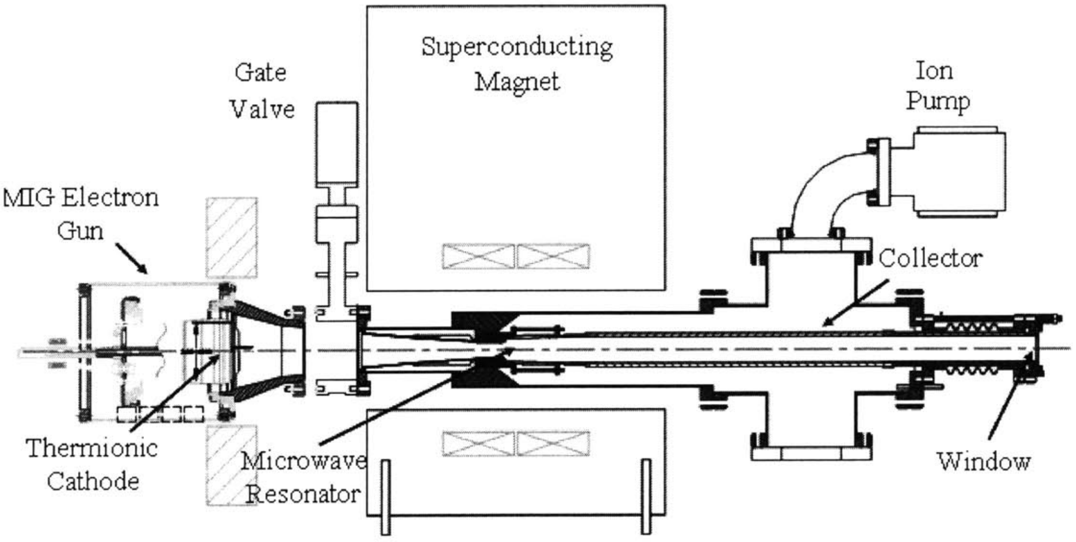

Figure 3-1: Schematic of the 110 GHz, 1.5 MW experimental gyrotron in axial configuration.

configuration is displayed in Figure 3-1. The diode gun emitter has a slant angle of approximately 36° with the axis and emission area of about 11.1 cm^2. The current density at the cathode is 3.6 A/cm^2 to achieve the operating current of 40 A, well below the suggested maximum of 10 A/cm^2 to promote cathode longevity.

The electron gun uses a thermionic M-type tungsten cathode built by SpectraMat. M-type dispenser cathodes consist of an emissive mix impregnated into a porous tungsten pellet creating a low work function emitting surface. In addition, there is a very thin coating of osmium, iridium, or rhenium applied to the emitter face to lower the operating temperature of the cathode while maintaining emission density. This SpectraMat cathode has an impregnate ratio of 4:1:1 of $BaO:CaO:Al_2O_3$, a surface finish of 32 - 64 microinches RMS, and an osmium M surface coating. Previous measurements by Anderson [76] calculate the central work function of this cathode to be approximately 1.88 eV. The cathode activated easily with a vacuum pressure in the low 10^{-8} torr range.

3.2 Azimuthal Collector Current Probe Measurements

To obtain the azimuthal current distribution, the original copper pipe collector in Fig. 3-1 was replaced with a rotating collector current probe shown in Figure 3-2. This collector has a 15 degree axial slot allowing a small azimuthal angle range of the beam to move past the collector and strike an electrically isolated plate. The probe connects to a dial outside the vacuum capable of rotating the probe 360 degrees allowing for current sampling around the azimuth. In addition, the microwave resonator is replaced by a tapered section to impede any mode generation during the experiment.

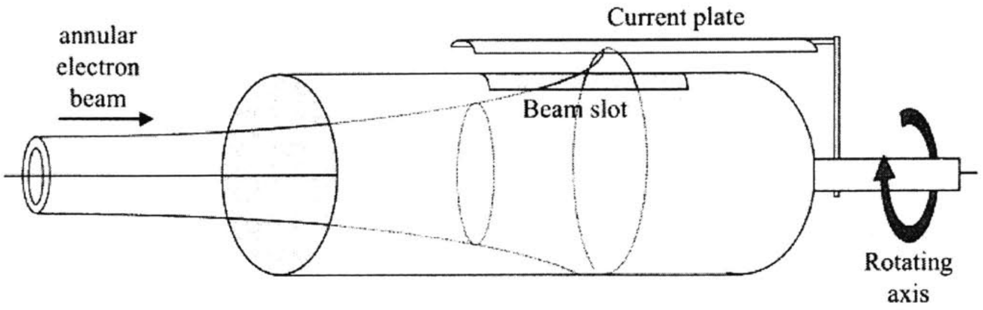

Figure 3-2: Slotted rotating current probe diagnostic. Current passes through the 15 degree slot providing a method to measure variations in azimuthal current with 15 degree precision.

After processing the collector to obtain stable operation, data was first taken at different cathode temperatures. I-V curves for different temperatures are shown in Figure 3-3. The curves clearly illustrate the transition from space-charge limited to temperature limited current regimes for different cathode temperatures. For all three temperatures, emission was well into the temperature limited regime past a voltage 30 kV. The cathode temperature of 985° C corresponding to the middle curve in Fig. 3-3 was found empirically to provide the operating voltage and current of 96 kV and 40 Amps. There was difficulty acquiring data past 80 kV because secondary electrons and high pressure led to drops in the overall current and operating stability.

Next, data was taken at a cathode temperature of 985° C for different azimuthal angles at a variety of cathode voltages. The results are shown in Figure 3-4 displaying the normalized current for different azimuthal angles. At low voltages (0-10 kV), emission is

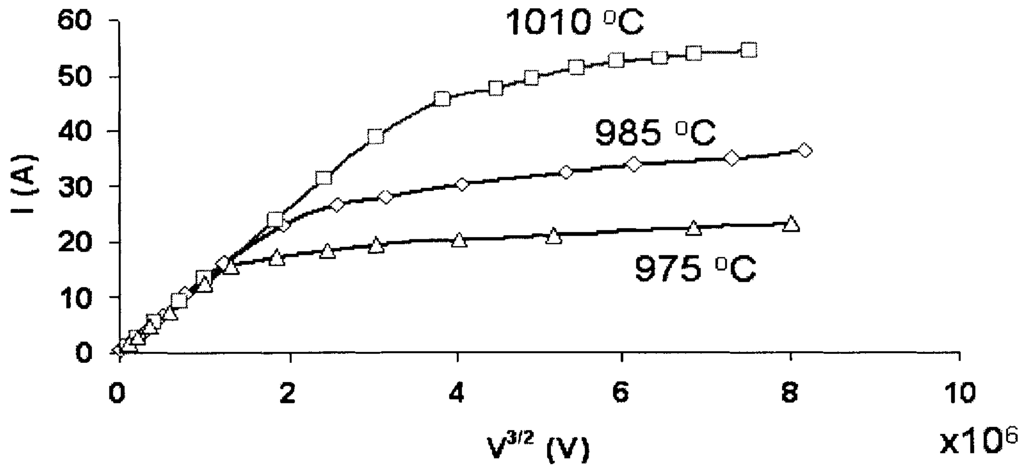

Figure 3-3: I-V curves for different cathode temperatures. 985 °C approximately corresponds to the normal operating parameters of 40 A at 96 kV.

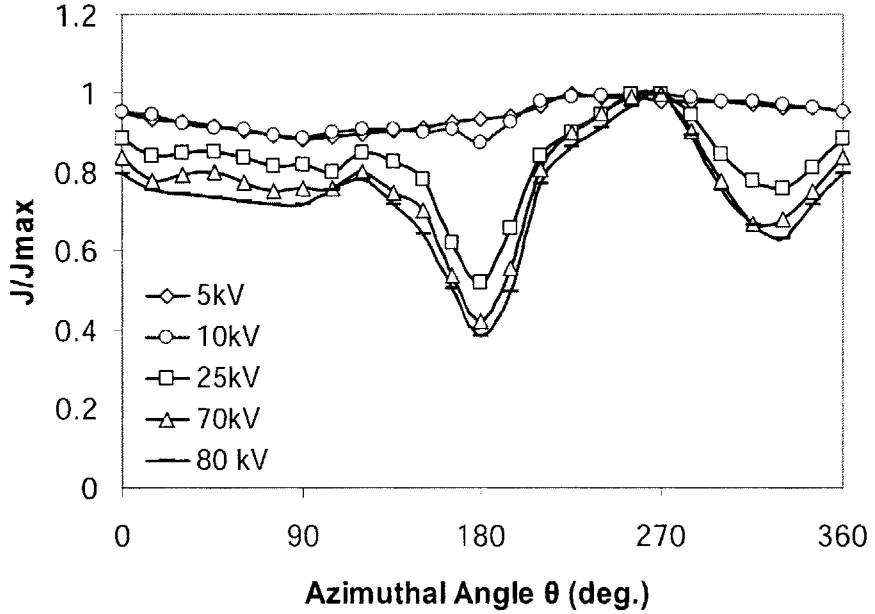

Figure 3-4: Normalized azimuthal current density profile measured by the rotating collector probe.

in the space-charge limited regime and the current should be completely uniform. There is, however, a visible sinusoidal variation in the measured current. This phenomenon can be explained by a small 0.3 mm offset of cathode. The Child-Langmuir current is actually controlled by the electric field at the cathode surface and not the anode-cathode voltage indicated by eqn. 2.40. Eqn. 2.40 is an approximation valid for a diode device with $V = E/d$ where d is the anode-cathode spacing and E is the electric field. When d is not uniform azimuthally, one side of the cathode will experience more electric field than the opposite side creating a sinusoidal variation in current. The variation amounts to an azimuthal current fluctuation of 10% at low voltages. As the voltage is increased, non-uniformity will begin to manifest itself as emission enters the temperature limited regime where variations in work function and temperature have a prominent effect on the local emission density. Previous measurements at CPI have shown this cathode to have a particularly uniform temperature along the azimuth, so the majority of current non-uniformity is rooted in the work function spread. Increasing the voltage past 80 kV showed only small changes in the non-uniformity profile since all parts of the cathode are well past the transition into the temperature limited regime.

Fig. 3-4 shows the ratio of current densities reaching three to one at some angles and two regions at approximately 180 and 270 degrees that are particularly deviant from the average. The error in angle measurement is about $\pm 7\%$. Assuming a total average current density of 3.6 A/cm^2 at 40 A, the average current density per quadrant is displayed in Table 3-2. The average current per quadrant is necessary for the upcoming simulations as well as for determining the alpha values from the segmented current probes.

Quadrant #	Angle range	Average Current Density
Q1	315°-45°	3.53 A/cm^2
Q2	45°-135°	3.73 A/cm^2
Q3	135°-225°	2.65 A/cm^2
Q4	225°-315°	4.49 A/cm^2

Table 3-2: Average current density for each azimuthal quadrant. Overall current density at 40 A is approximately 3.6 A/cm^2 at the cathode.

The result in Fig. 3-4 is especially interesting since it shows an evolution of cathode emission to the previous measurement taken in 2003. When compared to the measurement by Anderson [76] shown in Figure 3-5, a noticeable difference in the current profile occurs at 315 degrees. Previously, there was no local minimum at this angle where the recent measurement show there is. The difference could be accounted for if part of the emitter became poisoned between the two experiments. Mild poisoning of the emitter surface will have the same effect as lowering the work function resulting in lower current from the contaminated section.

3.3 CCR Cathode Uniformity Test

For future cavity efficiency studies to be most accurate, it is crucial to have a uniform emitting cathode to avoid a potential cause of low efficiency. Therefore, in our next phase of research we will be testing three new cathodes in an effort to obtain an

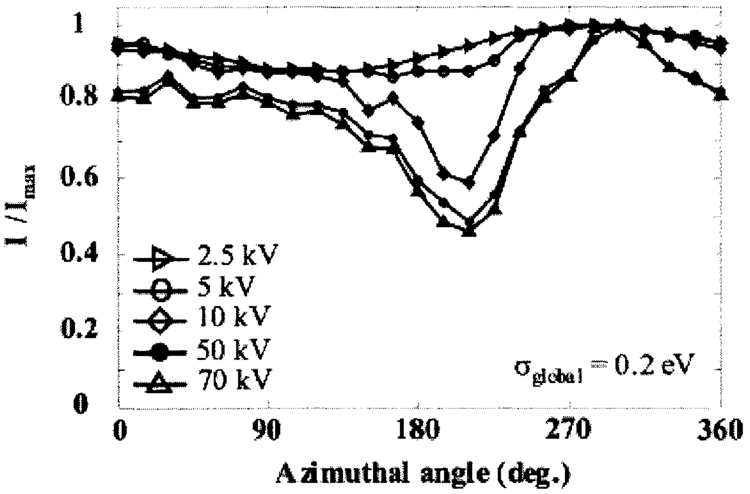

Figure 3-5: Previous non-uniformity measurement [76] showing no local minimum at 315 degrees.

azimuthally uniform cathode for use in upcoming experiments. The first of the cathodes is an identically manufactured cathode to the present cathode in the 110 GHz gyrotron summarized in Table 3-1. This cathode will be referred to as Cathode B. The other two cathodes will be manufactured using a new fabrication process developed by Calabazas Creek Research (CCR) in cooperation with Semicon Associates, Inc and Spectra-Mat, Inc [77]. This section discusses the azimuthal current density measurement using the CCR tester for the first of these cathodes. The measurement setup is described in the ensuing pages followed by the preliminary uniformity data from the first measurements.

3.3.1 CCR cathode tester setup

The CCR cathode uniformity tester consists of a demountable cathode apparatus and a rotating anode as depicted in Figure 3-6. A small faraday cup is embedded within the anode at an arbitrary azimuthal position. The faraday cup is about .002 inches in diameter and serves as the current probe. As the anode is rotated the current probe rotates as well, enabling the experimenter to sample all 360 degrees of the emitter surface. The vacuum chamber shown in Figure 3-7, surrounds the cathode-anode system. Viewing windows and feed-through leads are located every 90 degrees around the chamber. On one side, a pyrometer takes an estimate of the emitter temperature through optical pyrometry. Ninety degrees from that, vacuum pumps and a residual gas analyzer (RGA) connect to the chamber. Opposite the pyrometer is the high voltage input as well as the current probe output. The current probe is fed into an integrator circuit since the probe current is too small (μA) for simplistic direct measurements. Instead the difference in the level of current integration is used to evaluate the emission homogeneity. Eventually, the entire data taking system will be capable of full computer control.

The cathode tester is normally operated at very low voltages and low temperatures. Though the actual MIG is designed for full operation at 96 kV and 40 A, this degree of current would make it impossible to have stable operation. All the current will be striking the anode, about .75 inches away, causing a tremendous amount of out-gassing leading to poisoning of the cathode and possible arcing. Thus all the measurements for this experiment will be taken at less than 5kV with short one microsecond pulses. To have the cathode sufficiently in the temperature-limited range at this low voltage, the cathode temperature must be dropped significantly as shown in Figure 3-8.

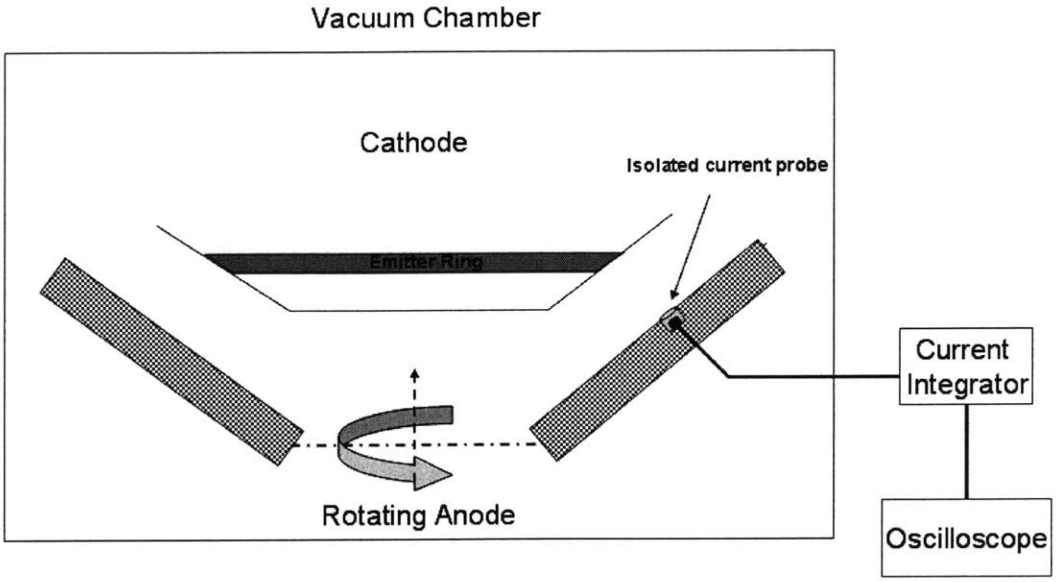

Figure 3-6: Schematic of the CCR cathode tester with demountable cathode and rotating anode.

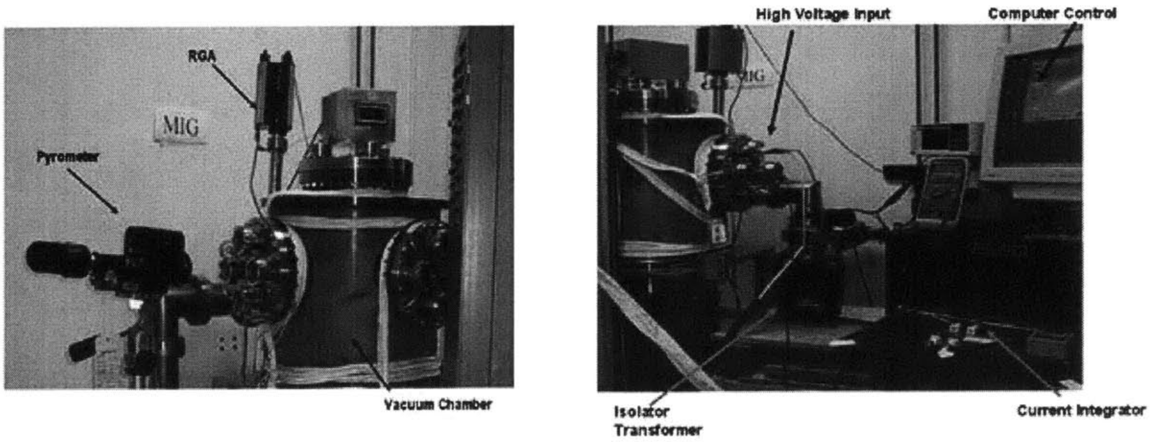

Figure 3-7: Experimental setup outside the vacuum of the CCR cathode tester [75].

3.3.2 Cathode B uniformity measurement data

The uniformity measurements on the CCR tester were taken at a cathode voltage of 1.2 kV and 850 degrees C. Initially, data was attempted at 4 kV and 890 degrees C, but the total current began to drop with time. Thus the voltage and the temperature were brought down to a level where the current remained fairly stable over the measurement duration. At 1.2 kV, the total current was approximately 250 mA.

Figure 3-8 shows the I-V curve at a temperature of 850 degrees C. Taking the ratio of the current at different temperatures allows one to calculate an estimate of the average work function expressed as

$$\frac{J_2}{J_1} = \frac{T_2^2}{T_1^2} \exp\left[\frac{-e\phi}{k}\left(\frac{1}{T_2} - \frac{1}{T_1}\right)\right] \tag{3.1}$$

where J is the current density, T in the temperature in Kelvin, k is Boltzmann's constant, e is electron charge and ϕ is the work function in eV. The average work function extracted with this method and Figure 3-8 was found to be approximately 1.95 eV. This is about .07 higher than the similar cathode currently installed on the experimental gyrotron leading to the conclusion that the cathode was not fully activated and will need further running before future data is taken.

Measuring a preliminary uniformity profile at a total current of 0.25 A and a voltage of 1.2 kV gave the azimuthal emission uniformity shown in Figure 3-9. This measurement yielded an almost sinusoidal current density emission variation with a max to min ratio of 2.5 to 1. The current remained steady at a cathode temperature of 850

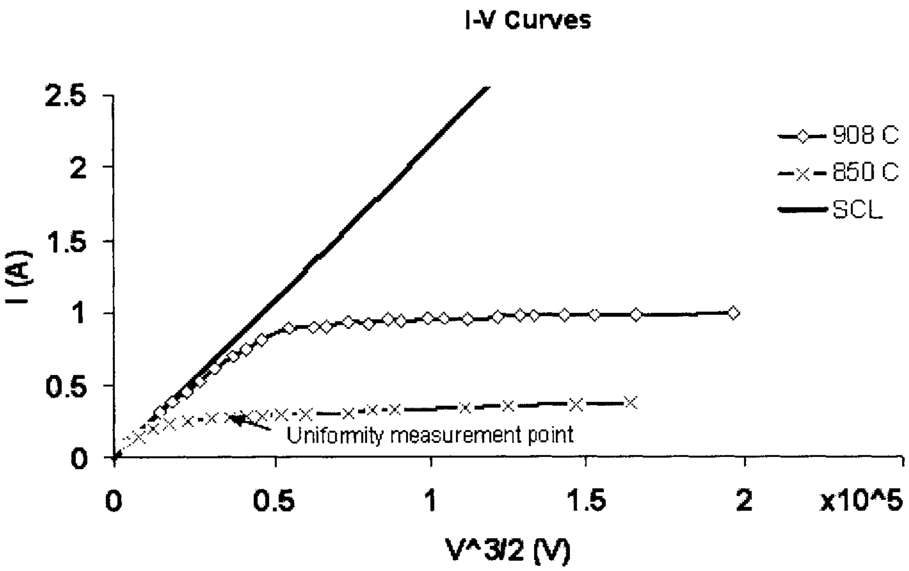

Figure 3-8: I-V curves for 850 and 908 degrees C as well as the space charge current limit. The uniformity measurement was taken at 850 degrees C.

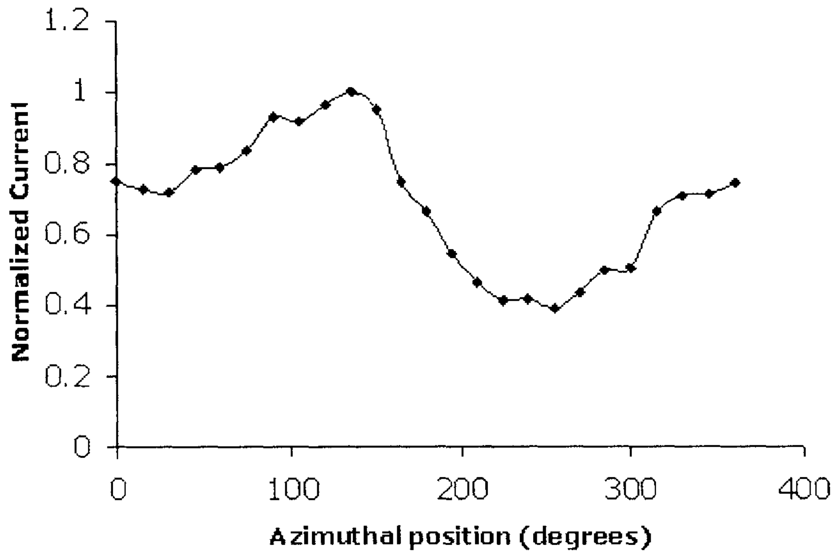

Figure 3-9: Azimuthal emission profile obtained for initial CCR cathode test on Cathode B.

degrees C throughout the measurement.

Given the lower current density and the lower calculated work function of this measurement compared to previous measurements, more measurements should be taken to validate the uniformity profile shown of Figure 3-9. Further processing of the anode to reduce cathode poisoning and longer activation of the cathode may be required. This experiment was solely the initial test of the first of three cathodes to be measured. Eventually all three cathodes will be thoroughly tested and the most uniform of the three will be installed on the present experimental gyrotron at MIT.

3.4 Summary and Conclusions

This chapter presented the experimentally obtained emission non-uniformity profile for two cathodes for the 96 kV, 40 A magnetron injection gun used in the 1.5 MW gyrotron at MIT. The first cathode is presently installed on the experimental gyrotron and the second is the first of three separate cathodes identical to the first that are to be tested for emission uniformity.

Non-uniform emission has become a potential culprit of poor efficiency and measuring the present uniformity profile was the first step in thoroughly modeling the phenomenon in a 3-D gun code. This experiment accurately assesses the azimuthal cathode emission of the active MIG to serve as an input into MICHELLE 3-D and to aid in the calculation of experimental segmented alpha values discussed in the following chapters. This cathode was found to have a significantly high level of non-uniformity with azimuthal current differences reaching three to one at certain angles. The subsequent chapter will use the obtained emission profile in MICHELLE 3-D to determine values such as alpha and the perpendicular velocity spread and to compare the results to a completely uniform beam.

The measurement of the second cathode, Cathode B, is an ongoing effort to characterize the uniformity profile of three new identical cathodes to the one presently installed on the experimental gyrotron. The preliminary results for the first of the new cathodes are presented in this chapter. Further measurements in the upcoming months will have to be done on this cathode to assure full activation of the cathode at measurement time. Once the other two cathodes have been manufactured, they will be tested similarly to the first cathode. The cathode with the best uniformity profile will then be installed on the experimental gyrotron for forthcoming efficiency experiments.

Chapter 4

3-D Emission Non-Uniformity Simulations

Research on the International Thermonuclear Experimental Reactor (ITER) has recently intensified with the approval of the of the facility site in Cadarache, France. Slated for initial operation in 2016, ITER will incorporate twenty-four 1 MW, 170 GHz gyrotrons and three 1 MW, 120 GHz gyrotrons. Achieving the desired overall gyrotron efficiency presents a difficult problem since there are currently no gyrotrons capable of producing 1MW of continuous power over 50 % efficiency. As stated previously in [68] and [71], poor efficiency has been attributed to azimuthal inhomogeneous cathode emission even without extensive modeling. A full 3-D model is necessary to determine the detrimental effects from emission non-uniformity on the beam quality and in turn the efficiency.

Since non-uniform emission must be simulated in a fully 3-D model, simulating the phenomenon is problematic due to computer processor speed and memory limits as well as code availability. With the advent of fast computers and the newly developed 3-D gun optics tool MICHELLE, a full model from the cathode to the cavity is now realizable. This chapter discusses the modeling results of the first fully 3-D model of a magnetron injection gun from the cathode to the cavity with the inclusion of azimuthal non-uniformity. The 3-D code is first benchmarked to EGUN and the 2-D version of MICHELLE. Then the experimentally obtained emission non-uniformity profile found in chapter three is simulated with MICHELLE and changes in alpha and perpendicular velocity are compared with those of a uniform beam.

4.1 Velocity Spread and Pitch Factor

The parameters defining beam quality consist of the spread in the electron velocities and the average pitch factor alpha ($\alpha = v_{\perp} / v_{\parallel}$). These are the principle quantities that will be examined in the upcoming simulations. Since all the beam-wave energy conversion comes from the electrons' perpendicular velocity, it is imperative to have sufficiently high alpha for acceptable overall efficiency. Theoretical efficiency of perpendicular energy can reach up to 70% for an initially uniform phase distribution and even higher by pre-bunching the electron beam. As noted in section 5.3.2, reflected electrons causing parasitic oscillations and increased velocity spread as well as arcing and cathode bombardment limit attainable alpha values. Therefore, alpha is usually kept below 1.5. If a beam had zero velocity spread, attainable alpha values could be increased dramatically, allowing for greater overall efficiencies. Obviously, there will always be some sources of velocity spread, but any way to minimize their presence will benefit gyrotron efficiency, promote stable operation, and limit mode competition.

For the cyclotron resonance interaction operating near cutoff ($k_z = 0$), the perpendicular velocity spread parameter is very important, having a significant detrimental effect on the synchronism of the interaction by interfering with the bunching process. For a monoenergetic beam, the perpendicular velocity spread $(\Delta v_\perp / v_\perp)$ is linked to the parallel velocity spread $(\Delta v_\| / v_\|)$ by the relation

$$\frac{\Delta v_\|}{v_\|} = \alpha^2 \frac{\Delta v_\perp}{v_\perp} \tag{4.1}$$

where Δv is usually taken as the standard deviation.

Some of the common causes of velocity spread are listed below [78]:

1) Spread of initial electron velocities
2) Emitter surface roughness
3) Non-uniform electric and magnetic cathode fields determined by the geometry of the electrode and the magnet (optical spread).
4) Azimuthally inhomogeneous beam emission
5) Space charge field in the beam
6) Convective Instabilities (negative mass, diochotron)
7) Global Instability (trapped electrons)

All of these mechanisms can contribute to an increase in velocity spread of the beam, but 2-D simulations can only adequately predict the cumulative effect of optical and space charge fields. Actual spread is usually estimated at about double what 2-D simulation can predict. Using a 3-D gun code, the effects of non-uniform emission can also be taken into account in the theoretical estimate. Non-uniform emission induces velocity spread by changing the potential at the cathode for different azimuthal regions or by possibly exciting a convective instability in the beam. There has never been a complete 3-D model to estimate the spread from non-uniform emission or establish how detrimental an effect it is. The primary concern of this research and the following simulation study will seek to discover just how serious non-uniform emission is to the beam quality and report conclusions based on that study.

4.2 Simulation Tools

4.2.1 MICHELLE

MICHELLE 3-D gun optics and collector modeling tool [63] is a three-dimensional finite element code developed by Science Applications International Corporation (SAIC). The motivation for MICHELLE came from a need to model in three-dimensions with greater precision with careful consideration for distinctly fine features. MICHELLE's physics engine follows the general self-consistent field solver model shown in Fig. 2-8. MICHELLE was particularly attractive for this problem because it was capable of simulating relativistic 2-D and 3-D self-magnetic fields and had a well supported GUI and post processor. In addition, MICHELLE uses the ICEM CFD meshing tool [79] developed by ANSYS for superb control over mesh density in three-dimensions.

4.2.2 ANSYS ICEM CFD Meshing Tool

To adequately model a MIG, it is necessary to have strict control over the mesh density following the beam. The MIG geometry shown in Figure 4-1, presents a difficult problem

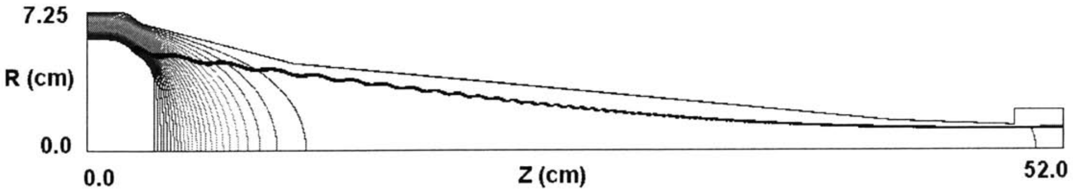

Figure 4-1: Magnetron injection gun geometry, equipotential lines, and beam path.

due to the annular beam and the long, thin structure. The mesh needs to be well refined near the beam, but also very coarse away from the beam to keep the mesh number under memory constraints. This does not present a problem in 2-D codes where the mesh can be refined to more than necessary levels and still be safely under the memory constraints. In 3-D, the mesh element number becomes problematic in keeping below the 3 GB addressable limit for a single processor on modern 32-bit PC's, while still achieving adequate resolution for solution accuracy. As shown in Figure 4-2, ICEM CFD allows for very strict control over the mesh density using either a structured or unstructured grid. 2-D mesh elements can be a combination of quads or triangles while 3-D elements consist of hexahedrons and tetrahedrons. ICEM also allows for a model to be created in two-dimensions and then extruded around the axis for a full three-dimensional model, a capability very advantageous for modeling axis-symmetric geometries such as a MIG in three dimensions.

4.2.3 Voyager Post Processor and Python Post Processor

MICHELLE comes with VoyPP, a built-in post processor GUI helpful in displaying the fields, potentials, and particle trajectories. VoyPP also has the capability to find the average values important to MIG beam design such as the pitch factor (α) and

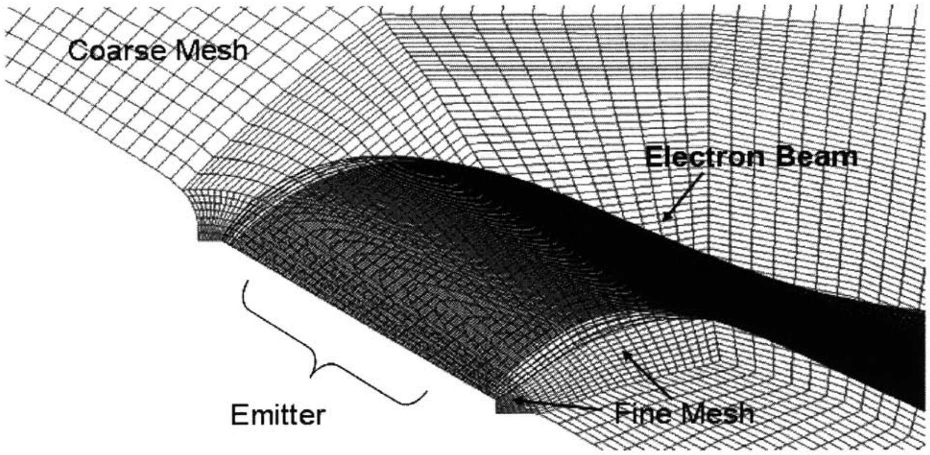

Figure 4-2: Illustration of the mesh density control in ICEM CFD mesh generator.

perpendicular velocity spread ($\delta v_{\perp}$). For our purposes though, it was necessary to have α and $\delta v_{\perp}$ values for different azimuthal quadrants to compare with experiment and to determine local effects from the emission non-uniformity.

For the advanced post processing needs, the Python coding language was used to parse the data and calculate the necessary parameters. MICHELLE can export the momentum and position of each particle at different slice planes, but the particles need to be orientated in coordinates parallel and perpendicular to the beam. Since the electron beam spirals around the magnetic field, the parallel and perpendicular momentum can be found by taking the scalar product of the momentum vector and the unit magnetic field vector. The magnetic field at specific particle positions was found by a special "export magnetic field array" command translated to Python from its original version in C by Ben Held, co-creater of the VoyPP and employee of Simulation Technology and Applied Research. After the momentum is separated into parallel and perpendicular directions, $\delta v_{\perp}$, $\delta v_{\parallel}$, $v_{\perp}$, $v_{\parallel}$, and α can be found with parsing code in Python for different azimuthal sections and the overall beam average as well. The Python post processor is run directly from the command line in VoyPP and takes about 20 minutes for a full 3-D run.

4.3 MICHELLE 3-D Benchmarking

Before using MICHELLE to model the emission non-uniformity, the code was benchmarked to the accepted 2-D gun code EGUN and to the 2-D version of MICHELLE as well. Modeling a large 3-D structure from the cathode to cavity such as the MIG profiled in Fig. 4-1 has never been before successfully attempted. There is some uncertainty if the code will be able to perform and converge accurately with such a difficult long and thin geometry and limited mesh capacity. In order to ensure reliability of the modeling of this problem in full 3-D geometry and to have better credibility for the non-uniform case, MICHELLE 3-D had to prove its capability of producing accurate results. To accomplish this, MICHELLE was run in the 3-D case with a uniform beam and beam parameters such as alpha, the perpendicular velocity, and perpendicular velocity spread were compared between the three codes.

The comparison is shown in Figure 4-3 for average alpha and the perpendicular velocity spread. The alpha curves are almost completely overlapping, all showing a theoretical alpha of 1.4 at the entrance to the cavity. The perpendicular velocity spread curves are also very similar, showing a $\delta v_{\perp}$ of 1.8% at the entrance of the cavity. The curves do show a difference in the mixing region of the velocity spread. EGUN shows a much more pronounced mixing region with a velocity spread increase of 0.8 percentage

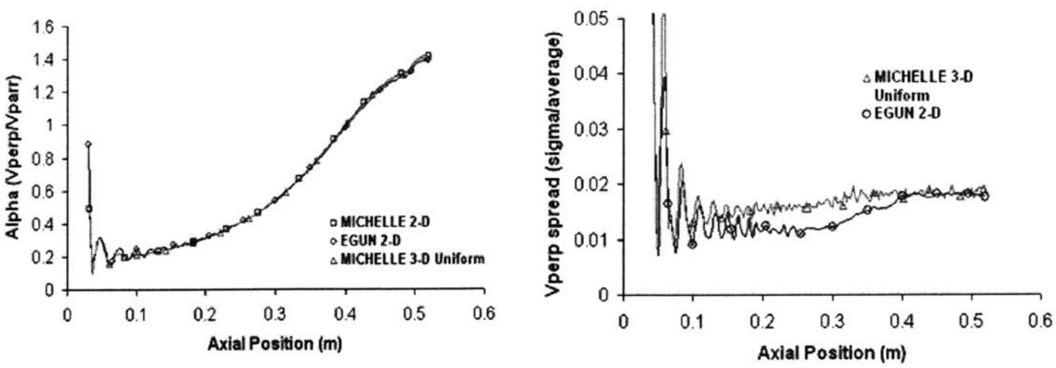

a) Alpha

b) Vperp Spread

Figure 4-3: Comparison of alpha and perpendicular velocity spread. Alpha curves are almost completely overlapping. Perpendicular velocity spread is also very similar between the codes.

points beginning at 30 cm while MICHELLE 3-D shows an increase of 0.3 percentage points beginning at 30 cm. The difference in the mixing region may be the result of many more particles in 3-D (≈1000) versus EGUN 2-D (≈25) and difference in the meshes. EGUN uses a triangular mesh while MICHELLE 3-D uses hexahedrons in the beamline.

Comparing codes will always show slight distinctions due to inherent differences in the mesh and the field solver algorithm. Even comparing runs of different setups will produce disparity within the same code. For instance, varying the mesh in MICHELLE will show differences in the calculated alpha values, but only to about one percent. Overall, the comparison of MICHELLE 3-D to EGUN and MICHELLE 2-D provided a satisfactory result. The evolution of $\delta v_\perp$, $\delta v_\parallel$, $v_\perp$, $v_\parallel$, and α as well as their cavity entrance values all compare reasonably well between the three codes and justify proceeding to non-uniform emission studies with MICHELLE 3-D. The following section discusses the modeling approach and summarizes the results of 3-D inhomogeneous emission.

4.4 MICHELLE 3-D Non-Uniform Emission Study

After determining MICHELLE can produce accurate results in a full 3-D geometry, the code setup was modified to incorporate different azimuthal emission sections. A number of different meshes were used, varying the mesh and number of azimuthal sections for each. The final 3-D mesh used in this study has a combination of hexahedrons and tetrahedrons with the majority being hexahedrons. The total number of 3-D mesh elements is approximately 2.4 million hexahedrons and .2 million tetrahedrons giving a solution memory requirement just under the 3 GB limit. Originally created in 2-D, the mesh was transformed to 3-D by extruding the mesh around the axis in five degree increments giving a total of 72 azimuthal sections.

4.4.1 Two to one current density variation in four quadrants

A first test was performed by splitting the emitter section into four sections as shown in Figure 4-4a with alternating cathode current densities of 4.48 A/cm^2 and 2.24 A/cm^2 giving an average cathode current density of 3.6 A/cm^2 to produce 40 A of beam current. This emission profile produced the $\delta v_\perp$ shown in Figure 4-4b. Surprisingly, the overall spread only increased from 1.8% (uniform case) to 2.2% (non-uniform case). The local spread in the low current density quadrant changed very little remaining at approximately 1.8% while the high current density quadrant increased to about 2.3%. The increase of

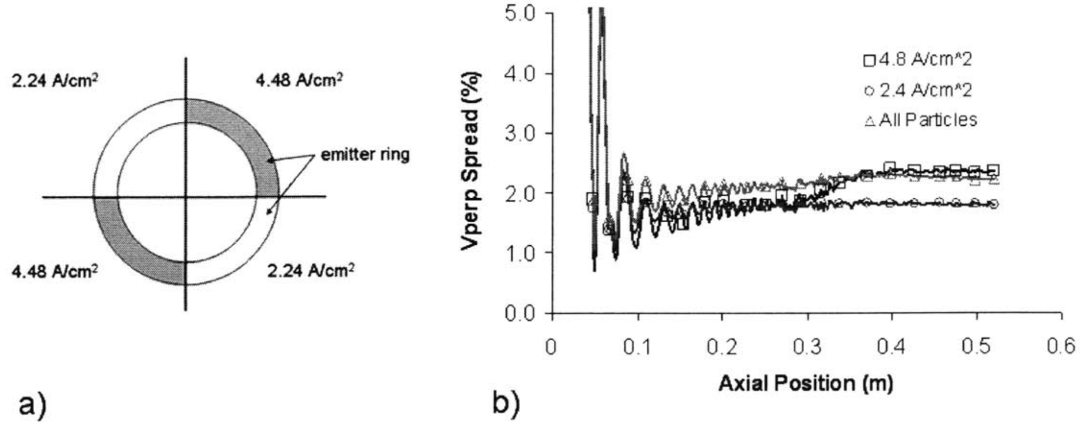

Figure 4-4: a) Initial test of non-uniformity in MICHELLE 3-D. Four emitter sections are segmented azimuthally with a current density ratio of 2 to 1 in adjacent quadrants. b) The resulting perpendicular velocity spread for the high and low current density quadrants as well as the total spread of the entire beam.

overall spread was much lower than expected considering the significant degree of non-uniformity. Differences in alpha were also fairly muted with the high current density quadrant having an alpha of 1.41, the low current density quadrant having 1.35 and a beam average of 1.38. The non-uniform case shows an almost negligible difference in alpha and perpendicular velocity spread resulting from the non-uniformity. This slight degradation in beam quality would have little effect on the efficiency of the device.

An interesting observation can be made from Fig. 4-4b in that the mixing region almost disappears for the low current density quadrant. The mixing region as demonstrated by Liu in [80] is the region where the electron trajectory phases mix. This can be thought of as where the original quasi-laminar beam becomes a regularly intersecting or non-laminar beam. Initially in the laminar beam state, the axial periodicity of the electron beam creates a periodically varying space charge potential causing the oscillations in $\delta v_\perp$ as seen in Figure 4-4b. Eventually, the electron trajectory phases mix, losing the axial periodicity and causing $\delta v_\perp$ to saturate at a particular value as seen for $z > 35$ cm in Fig. 4-4b. This velocity spread saturation is due to the effect of beam space charge. The lack of a well defined mixing region for the low current density quadrant case reveals that the beam space-charge has little effect on the velocity spread for this current density.

4.4.2 Experimentally obtained emission profile

After discovering the fairly small effect for the two to one current density quadrants, the code was then run with the non-uniformity profile obtained experimentally with the rotating collector probe found in Fig. 3-4. The code was run with the azimuthal non-uniformity represented three different ways:

1) averaging the current of Fig. 3-4 into four different emitter quadrants such as Fig. 4-5a,
2) averaging the current of Fig. 3-4 into 28 emitter sections,
3) using a single emitter with emission dependent on azimuthal angle as defined by a current data input file consistent with Fig. 3-4.

All three of these methods produced very similar results for the emission profile. The averaged current into four quadrants is shown in Figure 4-5a and the resulting overall perpendicular velocity spread in Figure 4-5b. $\delta v_\perp$ again showed very little increase due to the non-uniformity. The overall beam had a spread of about 2.05% compared to 1.8% of a 3-D uniform beam. Individual quadrants had spreads from 1.8% in the lowest current

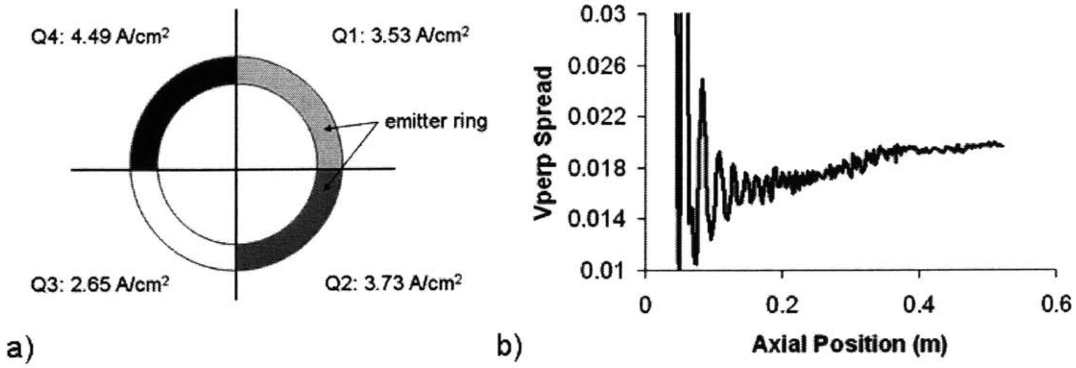

Figure 4-5: a) Experimentally measured current profile of the MIT 110 GHz gyrotron averaged into four quadrants. b) Resulting perpendicular velocity spread of the entire beam with the non-uniformity shown in a).

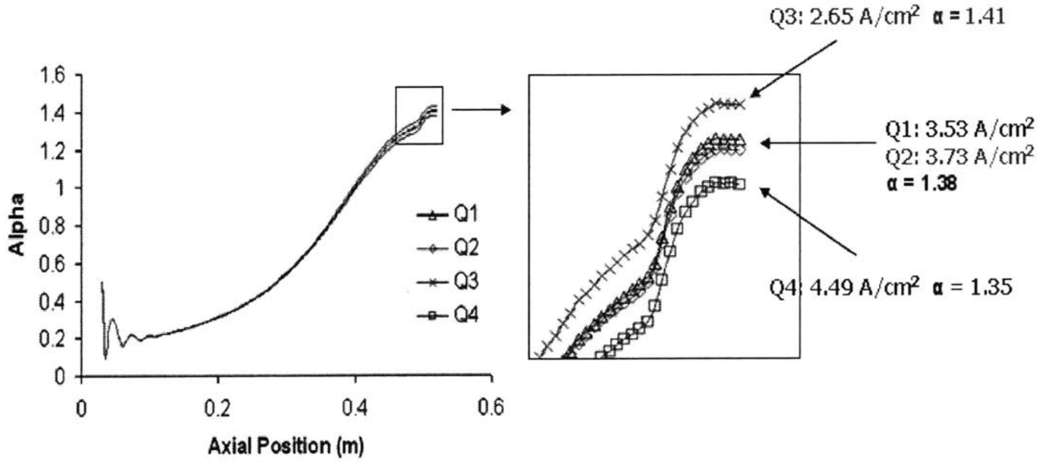

Figure 4-6: Comparison of alpha from MICHELLE 3-D for different azimuthal quadrants with the current density profile of Fig. 3-4.

density quadrant to 2.1% in the highest current density quadrant. The corresponding alpha curves for different quadrants are shown in Figure 4-6. The curves are almost overlapping one another. Alpha shows slight differences from quadrant to quadrant, 1.35 for the highest current density quadrant and 1.41 for the lowest current density quadrant, but the overall average alpha of 1.38 remains very close to the design value of 1.4. These small changes in the beam quality would have a negligible effect on the efficiency.

It is also interesting to point out that the velocity spread for each quadrant in the non-uniform case appears to be mostly determined by the local space charge and less by the loss of symmetry of space charge around the entire azimuth. This can be shown by comparing the velocity spread from the high current density quadrant of Figure 4-5. The local spread for this 4.49 A/cm^2 quadrant in the non-uniform case is 2.1 %. Running this current density in a uniform 3-D or in the 2-D case gives a total velocity spread of 2.0%, very close to the local spread of the single quadrant in the non-uniform case. Thus it seems that the velocity spread of different azimuthal sections of a non-uniform beam can be estimated reasonably well by running each current density emitter region as a single 2-D run. The lack of space charge symmetry over the entire azimuth has been shown to have little additional effect on the velocity spread on top of the velocity spread from the local space charge, the same space charge effect obtainable from a 2-D run.

4.4.3 Ten to one sinusoidal varying azimuthal emission non-uniformity

Though the experimentally obtained non-uniformity emission profile did not show much effect on the velocity spread, MICHELLE 3-D does show that a severely non-uniform beam will produce a significant increase in velocity and decrease in average

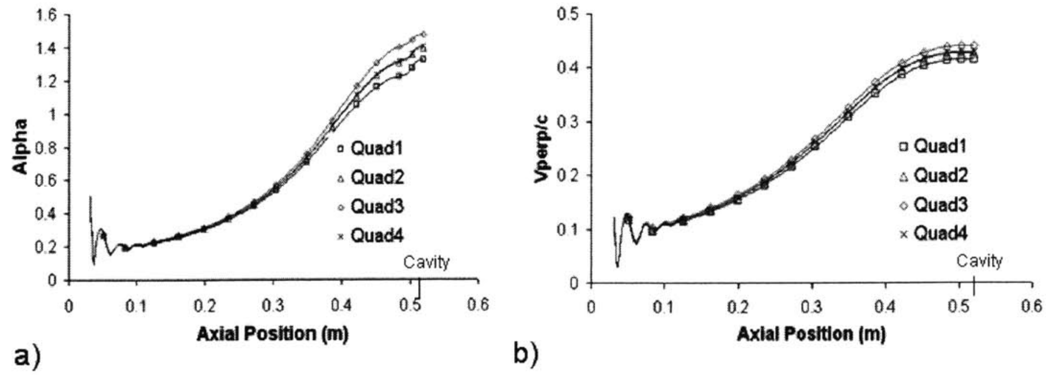

Figure 4-7: a) Alpha evolution from the cathode to the cavity for a sinusoidal azimuthal varying emission density of 10 to 1 peak to min. Four different quadrants are plotted with quadrant 3 having the min and quadrant 1 having the peak current density. b) Same emission as a) but instead showing the perpendicular velocity evolution.

alpha. Running a beam with a single (n = 1) sinusoidal variation along the azimuth with a 10 to 1 variation will result in an overall velocity spread of 3.15%, up from 1.8% spread of the uniform beam. Individual quadrants have perpendicular velocity spreads of 1.8 – 2.6%. This case is of particular interest since the perpendicular velocities of different regions begin to visibly separate as shown in Fig. 4-7b. Though the local quadrant spreads are not drastically increasing, the overall spread is increasing more rapidly from the divergence of the average perpendicular velocities. This increase of overall spread theoretically would result in an efficiency drop of a 1-2%.

4.4.4 Simulation solver parameters and inputs

It should be emphasized that the non-uniformity runs in MICHELLE 3-D were repeated many times to ensure proper convergence and to provide for the most adequate solution of the actual physical problem. There are, however, some parts of the MICHELLE physics engine solver that were not used due to memory constraints. The results presented in the preceding sections were run with a linear Poisson solver and with 2-D self magnetic fields. Switching to the quadratic Poisson solver requires almost four times the amount of memory needed for the solver and the full 3-D self-fields require about twice as much. Since the runs are done at maximum memory, the only way to allow for these other solvers would be to drastically reduce the mesh size. Being that the nominal mesh is somewhat coarse compared to a 2-D model to begin with, it was thought that the added physics by using these extra more expensive capabilities would not be as important as a well refined mesh. Thus the quadratic solver was not used in 3-D. The full 3-D self magnetic field solver was used with a coarse mesh and was found to compare very well with the 2-D self magnetic field non-uniform emission simulation and consequently was not used in later simulations.

In addition, the external magnetic field was a second order off-axis expansion of the on-axis field profile ($B_{\|}$ @$r = 0$). MICHELLE has the capability to translate magnetic field data from Maxwell 3-D or other magnetostatic solvers, but the off-axis expansion compared reasonably enough to provide justification for its use and to extinguish the need for a 3-D magnetostatic solver to be used. The on-axis field was the original on-axis field values used by EGUN to design the electron gun.

4.5 Summary and Conclusions

The first full 3-D simulation of a magnetron injection gun from the cathode to the cavity has been presented using MICHELLE 3-D. A uniform MICHELLE 3-D beam has shown very good comparisons in the beam pitch factor and perpendicular velocity spread to EGUN and a 2-D MICHELLE model. MICHELLE 3-D was run using approximately 2.4 million hexahedrons and tetrahedrons providing an adequate self-consistent solution.

After benchmarking to established 2-D codes, MICHELLE 3-D was used to extensively model the effects on alpha and velocity spread of an azimuthally non-uniform emitting beam in contrast to a uniform beam. Using an experimentally obtained azimuthal beam emission profile, MICHELLE found that the beam non-uniformity had only a very small effect on the beam alpha and velocity spread. The velocity spread increased from 1.8 % for a uniform beam to 2.05 % for a non-uniform beam and the average pitch factor remained within 1-2% of the design value of 1.4. The very small increase in velocity spread would have a negligible effect on the device efficiency. Modeling with more extreme uniformity, such as a ten to one max to min sinusoidal variation, produced an overall velocity spread of 3.15%, an increase of 1.35 %. This extreme non-uniformity does produce a velocity spread increase capable of decreasing gyrotron efficiency by 1-2 %, but is still rather small compared to the velocity spread increase necessary to produce the efficiency degradations seen in some industrial gyrotrons. The increase of velocity spread at severe non-uniformity is most likely due to the increased local space charge of the high current density regions and the spreading of average perpendicular velocities for regions of different current density as shown in Fig. 4.7b.

This research certainly does not stop here. The mandate for higher and higher gyrotron efficiency continues to increase, augmenting research into the quality of electron beams and 3-D effects. Future work needs to concentrate on still better meshing and the inclusion of expensive physics solvers such as the quadratic field solver as well as other 3-D effects such as off centered or angled cathodes or anodes. SAIC is currently working on a 64 bit version of MICHELLE. As 64 bit computers become more widely available and the code updates compatibility with the new systems, larger and more refined meshes will be attainable with the eased memory constraint. Unfortunately, the computer processor speed has stalled in the last couple years at about 3.5 GHz causing any increase in memory capabilities to also significantly increase the runtime. Parallel processing techniques will become important on these very long runs, but only certain codes have this ability and MICHELLE as of this date does not. Regardless of the runtime constraints, large fully 3-D simulations will continue to progress in the future providing valuable insight to the important design and manufacturing parameters of magnetron injection guns.

Three dimensional codes will also be needed to look into the effect of trapped electrons on the beam quality. Accurately modeling trapped electrons may only be possible through the use of particle-in-cell codes since the solving algorithm of electrostatic codes has difficulty converging in this situation. Advanced PIC codes will be needed to assess the impact of a small number of trapped electrons on the overall beam velocity spread and average pitch factor as well as any instabilities on the beam.

Chapter 5

Segmented Alpha Probes

For a simulation to have credibility describing a phenomenon that cannot be easily measured, it is advisable to compare a different phenomenon of the simulation that can be measured to that of experimental data. In this research, the perpendicular velocity spread is the most important quantity from the simulation. Previous attempts to measure velocity spread of the entire beam have been limited to scaled down versions [71, 81-83] due to arcing and reflected electrons at full voltage and current. Velocity spread is normally measured in a scaled down system by applying a retarding voltage at the collector to reflect a percentage of the beam and allowing electrons with sufficient parallel energy to reach the collector. The spread in the parallel velocity is found from difference in retarding voltage to reflect none of the beam and the entire beam. Then by knowing the average pitch factor, assuming a monoenergetic beam, and employing eqn. 4.1 the perpendicular velocity spread can be calculated. Of course, this is a very difficult procedure, with high experimental error, and has always given velocity spreads much higher than those of simulation. This setup is also for a scaled down version and is not capable of measuring the spread in different azimuthal sections.

An easier approach to validate MICHELLE would be an attempt to measure the beam pitch factor in azimuthal sections of different current densities in the actual gyrotron. Measuring alpha at full voltage and current through a capacitive probe is well known and has been used to measure alpha in gyrotrons and free electron lasers for many years [84-86]. The capacitive probe diagnostic depicted in the next section provides a passive method to estimate the average alpha of the beam. Dividing the probe into four azimuthal sections facilitates the measurement of alpha for the four quadrants simulated in chapter 4. Designed concurrently with the 3-D non-uniform emission simulations, the probes are intended to compare with simulation, and provide credibility to MICHELLE 3-D's results.

5.1 Single Alpha Probe

Capacitive alpha probes are described by a simple application of Gauss' Law. The alpha probe directly measures the amount of charge per meter of the electron beam passing through the probe as depicted in Figure 5-1a. The original unsegmented probe consists of essentially two concentric metal cylinders. The inner cylinder has a tapered inner radius fairly close to the electron beam separated from another outer cylinder by a dielectric. The outer cylinder is usually set at ground and is the back wall of the beam tunnel located just before the microwave resonator. The floating inner cylinder more closely resembles a ring since the probe length is kept fairly short to mitigate any effects on the beam quality. The tapered inner radius prevents any unintended oscillation of electromagnetic modes in the probe.

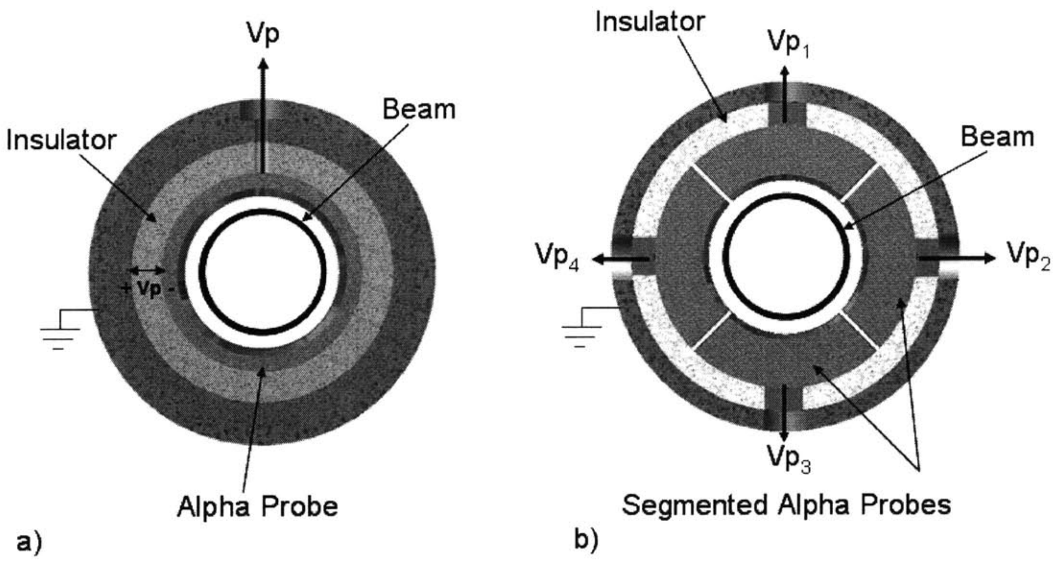

Figure 5-1: a) Geometry of single alpha probe to measure average alpha of entire beam. b) Geometry of segmented alpha probe to measure average alpha in four azimuthal quadrants.

Approximating the probe as two infinitely long concentric cylindrical electrodes and applying Gauss' Law gives the familiar equation $\xi = C_p V_p$ where $\xi = \int \rho r d\phi dr$ is the charge per unit length. ξ will induce an image charge on the probe creating a voltage V_p related by the capacitance C_p. Knowing that $I_b = \xi \langle v_{\|} \rangle$ at the axial position of the probe gives the relation

$$\langle v_{\|} \rangle = \frac{I_b}{C_p V_p} \tag{5.1}$$

where I_b is the beam current and $\langle v_{\|} \rangle$ is the average parallel velocity of the beam at the probe location. Then by knowing the beam energy from the cathode voltage, the perpendicular velocity can be computed by

$$\langle\beta_\perp\rangle = \sqrt{1-\frac{1}{\gamma'^2}-\langle\beta_\parallel\rangle^2} \tag{5.2}$$

where $\langle\beta_\perp\rangle$ and $\langle\beta_\parallel\rangle$ are the perpendicular and parallel velocities of the beam normalized by the speed of light and

$$\gamma' = 1+\frac{e(V_k-\delta V)}{m_0c^2} \tag{5.3}$$

where V_k is the accelerating cathode voltage, m_0 is the electron rest mass, and c is the speed of light. Thus alpha can then be found from $\alpha = \beta_\perp / \beta_\parallel$. Here γ' is expressed taking into account the voltage depression of the beam effectively lowering the energy of the beam. δV can be estimated by the approximation given in [84] as

$$\delta V \approx \frac{I_b}{2\pi\varepsilon\langle v_\parallel\rangle}\ln\left(\frac{r_w}{r_b}\right) \tag{5.4}$$

where r_w and r_b is the radius of the back wall and beam radius. The voltage depression can also be computed using a gun code and finding the potential difference between the beam and the back wall. The latter method was used for the purposes of this research since the alpha probe could be modeled using MICHELLE and it was thought that a more accurate representation of depression would be attained through simulation than the analytical estimate. Additionally, voltage depression will be different for different parts of a non-uniform beam again favoring simulation to provide a better calculation of depression. The voltage depression at the probe position was calculated with MICHELLE to be 2.4 kV for the highest current density quadrant and 1.7 kV for the lowest. The voltage depression in the cavity for this gun at operating voltage of 96 kV and current of 40 A is approximately 4-5 kV.

Calibration of the probe is found in situ by lowering the voltage such that the perpendicular velocity is negligible. At this voltage all the beam energy is in the parallel direction and equation 5.1 can be solved for the capacitance. The capacitance is assumed to remain unchanged with higher beam energies. An acceptable voltage range in which the perpendicular velocity is an insignificant fraction of the total energy is usually found from 0-5 kV for this gyrotron as verified by simulation. It should be emphasized that the voltage depression must be included in the calibration. Not including the voltage depression underestimated the capacitance by eight percent leading to underestimates of alpha in excess of fifteen percent.

5.2 Segmented Alpha Probes: Theory and Simulation

5.2.1 Revised probe equation

The fundamental physics of the single capacitive probe is fairly straightforward and has proved a valuable and easily implemented diagnostic in determining the pitch factor. Extending the physics to extract the pitch factor of four azimuthally segmented parts of the beam becomes more complicated. At first glance, everything in the diagnostic is multiplied by four. There are four probes, four different though relatively similar capacitances, four probe voltages, four currents, and four parallel velocities to be accounted for. As shown in Fig. 5-1b, the construction of the probe is equivalent to that of the single probe, except the single probe and insulator are segmented into four probes and insulators all electrically isolated from each other in four azimuthal quadrants. The difficulty, though, does not lie in the measurement book keeping, but in equation 5.1 that

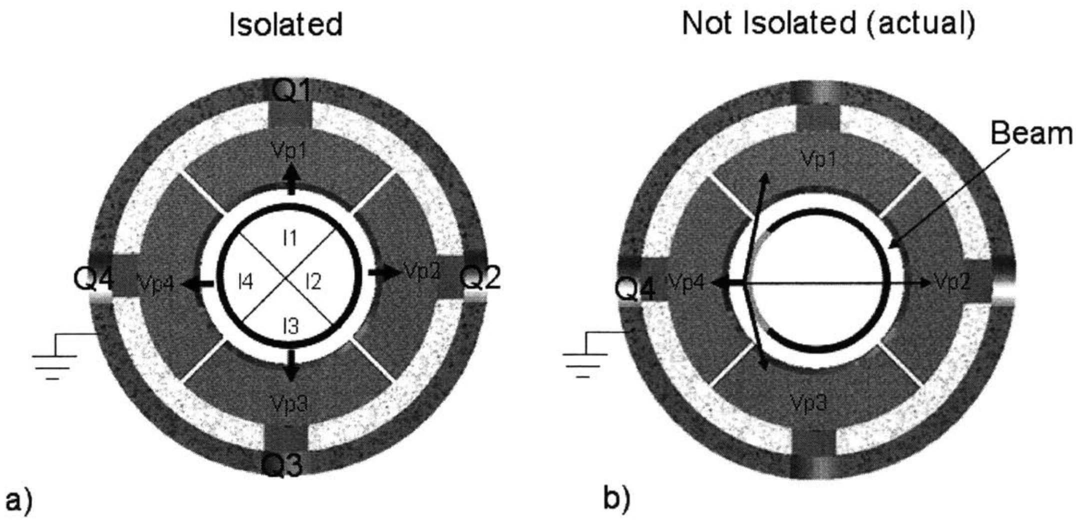

Figure 5-2: a) Isolated quadrants: all the probe voltage of a quadrant is induced by the current in that same quadrant; equation 5.1 is accurate. b) Actual situation: each quadrants probe voltage is induced by a combination of the currents in all quadrants.

describes the relationship between a quadrant's probe voltage V_{p_i} and the charge density $\xi_i = I_{b_i} / v_{\|_i}$. Derived from a symmetric system with a Gaussian surface, Equation 5.1 states that the probe voltage relates to the total current enclosed by the probe. For this equation to still hold true for the segmented probes, all the probe voltage of a quadrant would have to be induced by charge only from the current in that quadrant as shown in Figure 5-2a. Each divided quadrant is its own isolated system. That is to say that the probe voltage of probe 1 is only induced by the current in quadrant 1:

$$I_1 / v_{\|1} \rightarrow V_{p1}$$

In the real experiment, however, a significant amount of the probe voltage will be induced by the charge in other quadrants as shown in Figure 5-2b for the current in quadrant 4. Here the voltage on each probe is induced by a combination of the currents in all the quadrants such that for probe 1:

$$M_{14}I_4 / v_{\|4} + M_{13}I_3 / v_{\|3} + M_{12}I_2 / v_{\|2} + M_{11}I_1 / v_{\|1} \rightarrow V_{p1}$$

where M_{ij} is a cross-voltage induction factor describing how the current from quadrant j affects the probe voltage of the probe in quadrant i. M_{ij} is the ratio of the induced voltage on probe i from quadrant j to the induced voltage on probe i from quadrant i. For a non-uniform beam, the cross talk between quadrants effectively underestimates $v_{\|}$ for quadrants with less than average current and overestimates for quadrants with more than average current. To correct this, a matrix of four equations and four unknowns can be formulated as

$$\begin{bmatrix} V_{p1} \\ V_{p2} \\ V_{p3} \\ V_{p4} \end{bmatrix} = \begin{bmatrix} \frac{M_{11}I_1}{C_1} + \frac{M_{12}I_2}{C_2} + \frac{M_{13}I_3}{C_3} + \frac{M_{14}I_4}{C_4} \\ \frac{M_{21}I_1}{C_1} + \frac{M_{22}I_2}{C_2} + \frac{M_{23}I_3}{C_3} + \frac{M_{24}I_4}{C_4} \\ \frac{M_{31}I_1}{C_1} + \frac{M_{32}I_2}{C_2} + \frac{M_{33}I_3}{C_3} + \frac{M_{34}I_4}{C_4} \\ \frac{M_{41}I_1}{C_1} + \frac{M_{42}I_2}{C_2} + \frac{M_{43}I_3}{C_3} + \frac{M_{44}I_4}{C_4} \end{bmatrix} \begin{bmatrix} \frac{1}{\langle v_{\|1} \rangle} \\ \frac{1}{\langle v_{\|2} \rangle} \\ \frac{1}{\langle v_{\|3} \rangle} \\ \frac{1}{\langle v_{\|4} \rangle} \end{bmatrix} \qquad (5.5)$$

to solve for the correct parallel velocities. Inverting the above matrix will provide the parallel velocity for all four quadrants. A similar matrix must first be solved for the capacitances for each quadrant which is the same matrix above except C_i and $v_{\|i}$ are switched and the matrix inversion solves for C_i.

5.2.2 Cross voltage induction factors: MICHELLE 3-D

To find the cross induction factors M_{ij}, an electrostatic solver was used to simulate the floating capacitive probes. Initially 2-D codes such as Field Precision's Estat [87] and Ansoft's Maxwell 2-D [88] were used, but were met with little success. Approximating the floating conductors as a dielectric with a very high (10^5) permittivity presented convergence problems for Estat. Maxwell 2-D has a floating conductor material type and had adequate convergence but could not evaluate the 3-D effects of the system. Eventually, it was decided that a 3-D system would be necessary to calculate the cross-induction voltage factors. Instead of purchasing an expensive 3-D electrostatic solver, MICHELLE 3-D was modified to model the probes in the gun geometry. Again the floating conductor probes were modeled as a high permittivity dielectric, but unlike in Estat, MICHELLE 3-D performed very well, providing a converged 3-D electrostatic solution in a reasonable amount of time (2 hours).

The cross-induction voltage factors for this geometry were found by running current in only one quadrant of the beam (Figure 5-3). Then the voltage induced on all four probes was calculated in the post processor. The ratios of probe voltages of probes in no current quadrants to the probe voltage of the quadrant with current gave the cross-induction factors M_{ij}. Since the cross-induction factors for adjacent quadrants are the same and M_{ii} is 1, there are only two factors found to be:

Adjacent quadrant: $M_{i,i\pm1} = .336$

Opposite quadrant: $M_{i,i\pm2} = .115$

For example, this states that the current in quadrant 2 will induce 33.6% of the voltage it induces on probe 2 onto probes 1 and 3 and 11.5% on probe 4.

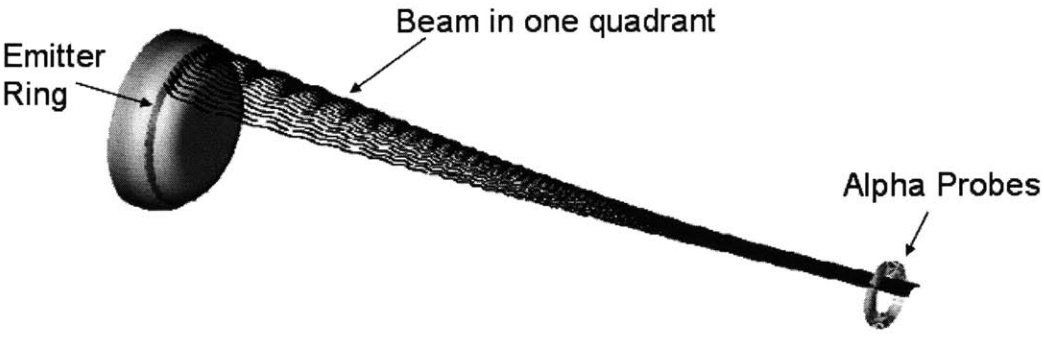

Figure 5-3: Modeling the alpha probes with MICHELLE 3-D. The cross-voltage induction factors are found by running current in only one quadrant and comparing the voltage induced on the no current quadrant probes to that of the current quadrant's probe.

The matrix approach performed quite well in simulation. Modeling the probes in MICHELLE allowed for the running of the experimental diagnostic in simulation complete with the same calibration and probe voltage detection behavior that would be done in the experiment. Calibration for the probes was carried out by running a uniform beam at 2 kV where the alpha was only .062 making the parallel velocity 99.8% of the total velocity. Next, a full non-uniform beam was simulated with the average current densities for the four quadrants found experimentally with the rotating current probe and shown in Fig. 4-5. The probe voltages for each quadrant were then extracted with the post processor. The results of alpha found with the simple relation in eqn. 5.1 (not corrected) and the corrected alphas found using the matrix of eqn. 5.5 (corrected) are shown in Figure 5.4. As seen in Fig. 5.4a, alpha is overestimated for quadrants of lower than average current density (quadrant 3) and underestimated for quadrants with higher than average current density (quadrant 4). Using the matrix method corrects this inaccuracy as

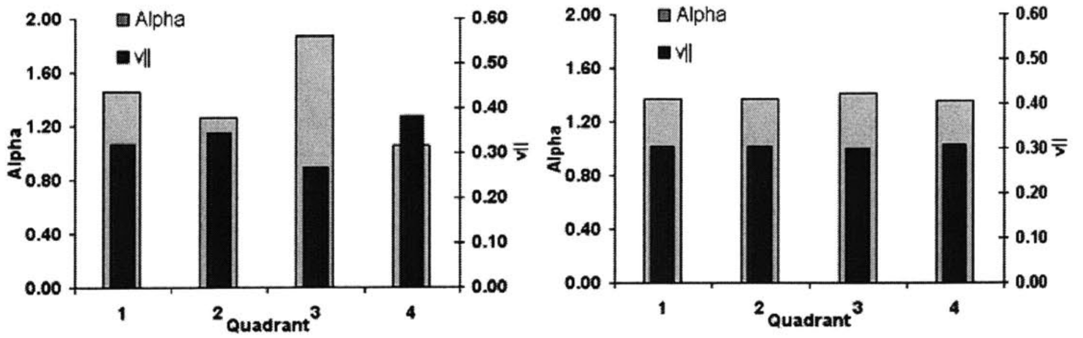

a) No correction

b) With matrix correction

Figure 5-4: Modeling the alpha probes for a four quadrant non-uniform beam in MICHELLE 3-D. a) Alpha and $v_{||}$ calculated from the probes using equation 5-1. b) Alpha and $v_{||}$ calculated using the matrix of eqn. 5.5 to provide the correction of cross talk between probes and current of different quadrants.

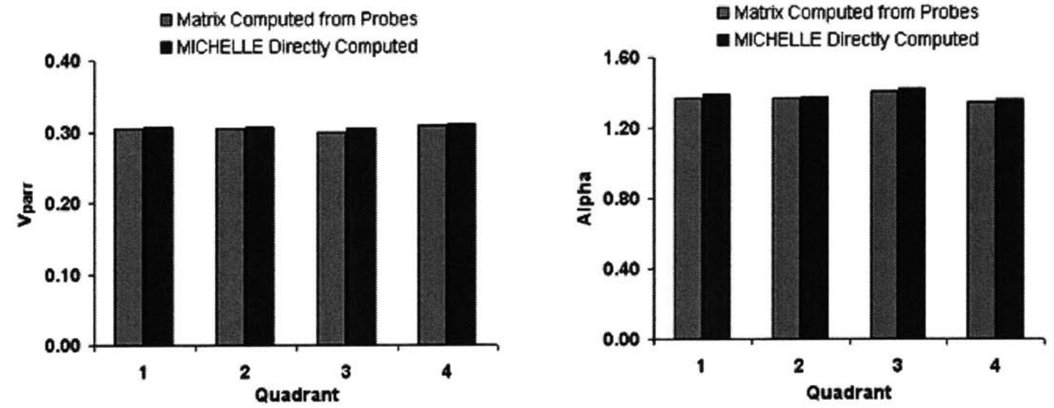

a) Parallel Velocity

b) Alpha

Figure 5-5: Comparing the a) $v_{||}$ and b) alpha values for a four quadrant non-uniform MICHELLE 3-D simulation computed using the probes in MICHELLE with the matrix calculation of eqn. 5.5 and the values directly computed from the particle data in MICHELLE.

shown in Fig. 5.4b. The corrected alpha and $v_{\|}$ found from the probes in simulation compare very well with the alpha and $v_{\|}$ directly computed using the MICHELLE post processor. As shown in Figure 5-5, even with very small differences in alpha of $\pm 2\%$, the probes were able to distinguish the variation in alpha from quadrant to quadrant following the results computed directly from the particle trajectory data of MICHELLE. Thus the matrix method of determining the alpha in four azimuthal sections had adequate accuracy when run in simulation, provided a solution to the cross voltage induction, and theoretically could provide the resolution needed for small differences in alpha.

5.3 Segmented Alpha Probes: Experiment

The final design of the segmented alpha probes had four stainless steel probes with inner radii of 1.26 cm with 34 degree uptapers and outer radii of 2.15 cm. Macor served as the ceramic insulator between the probes extending to the back wall at a radius of 2.54 cm. The probes shown in Figure 5-6, were installed about 2 cm axially behind the entrance to the microwave resonator of the 96 kV, 40 A gyrotron at MIT described in chapters 3 & 4, and were aligned to have the center of each probe as the center of the average current density quadrants of Table 3-2. Inside the gyrotron, each probe was connected through coaxial wires attached to four BNC connectors outside the vacuum. BNC cables then transferred the signals to a 350 MHz, four channel 1 Gs/s Agilent oscilloscope. The probe signals were later found to be quite noisy. Therefore, 10 kohm resistors were added

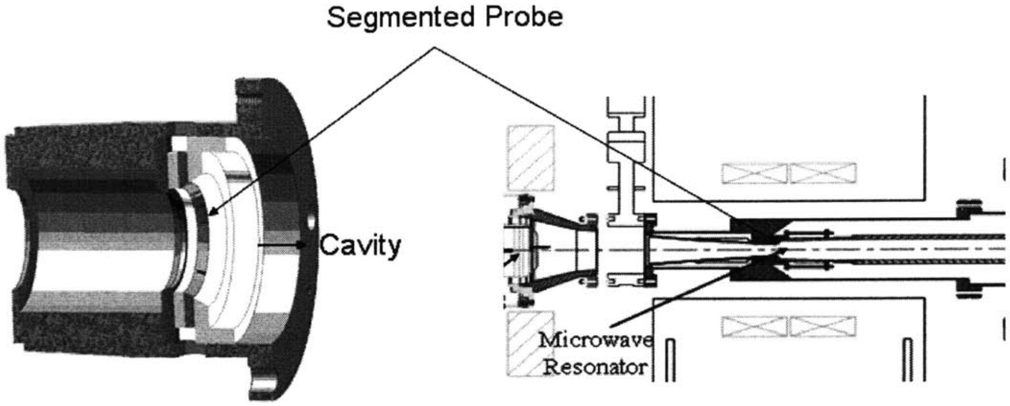

Figure 5-6: Cross section of the segmented alpha probe and its axial location with respect to the microwave resonator.

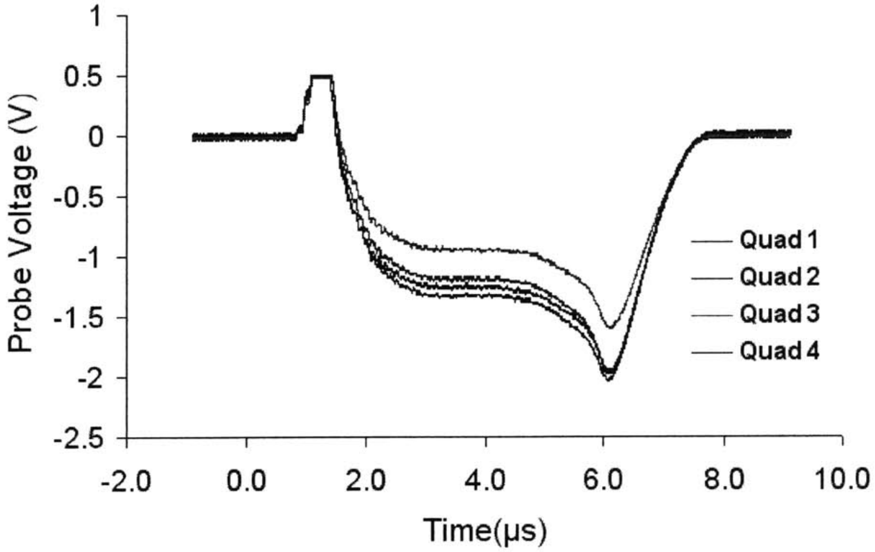

Figure 5-7: Experimental alpha probe signals as seen on the 350 MHz Agilent oscilloscope.

between the BNC cables and the oscilloscope terminals to act as low-pass filters. After the tube was heated to 200 degrees Celsius, the vacuum reached a pressure of 1 E-8 torr, more than adequate for full current operation. Following a thorough processing period, alpha probes signals such as those shown in Figure 5-7 could be obtained with a relatively flat voltage over the constant part of the three microsecond voltage pulse. The spike and dip in the alpha probe signals are due to transient effects from the rise and fall of the cathode voltage pulse. The gyrotron alignment corresponded to the maximum power point of the gyrotron, producing an approximate 1-1.5 MW of peak power.

Each probe's capacitance was found in situ by the method described in section 5.1 and 5.2. Reducing the cathode voltage to very low voltages in the range of 0-5 kV, a number of capacitance values for each probe were calculated with equation 5.1 and the average capacitance was used for each probe. A particular capacitance is only valid for a single alignment. Since changing the beam position changes the distance of the beam to a probe causing the capacitance to vary accordingly, all alpha probe measurements were taken at the same alignment.

Data was taken for several different voltages and magnetic compression values at the high power parameters previously found [89]. The average measured alpha of all four quadrants was found to be in the range of 1.3 to 1.5, very close to simulation alpha of 1.4. The average alpha for the entire beam at different high power points for varying magnetic field is shown in Figure 5-8 at a voltage of 96.5 kV and 40 A.

Attempting to extract the segmented alpha for each quadrant proved to be much more difficult than expected. The experimental error was so high (±15%) that measuring any differences in quadrant to quadrant alpha as shown from MICHELLE simulations

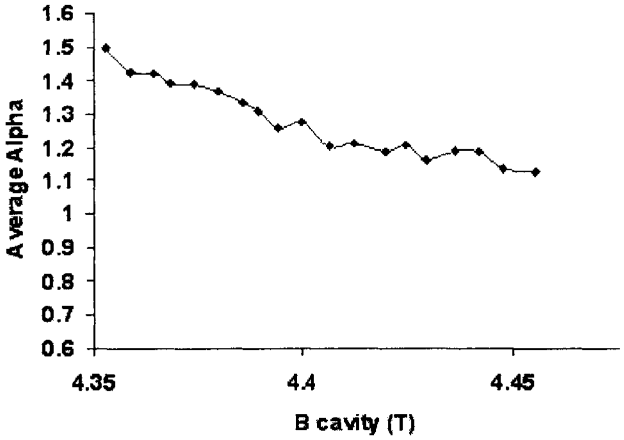

Figure 5-8: Measured average beam alpha over all quadrants for the high power operating points at varying cavity magnetic fields.

($\pm 2\%$) was impossible. In addition, though the matrix of eqn. 5.5 worked very well in simulation, it had difficulty producing physical answers when the inverse was taken with experimental data. Besides complications due to experimental error, there were also two important differences in the simulation and in the proposed experiment. First, the current in the experiment is not uniform for each quadrant. The actual current is a continuous distribution, but the average current for each quadrant is used for the input to the matrix of eqn. 5.5. The results of Figs. 5-4 and 5-5 were calculated with MICHELLE using the average current for each quadrant uniformly over that quadrant. Second, since the model in MICHELLE is a completely symmetric system, the capacitances of all the probes were exactly the same, with a perfectly aligned beam, and a correctly orientated magnetic field. The real experiment has capacitance differences between the probes of $\pm 10\%$, and a beam that is not perfectly centered on axis. These two important differences, along with a generally high experimental error, rendered the matrix method unusable with experimental data. A different method had to be used.

Instead of the more complicated matrix method, a simpler probe voltage correction was implemented to compute the segmented alpha values. The new method had less sensitivity to experimental error but provided a less accurate solution theoretically. This simple probe voltage correction expressed for probe 1 as

$$V_{p1corrected} = V_{p1}\left(\frac{M_{11}I_1}{M_{11}I_1 + M_{12}I_2 + M_{13}I_3 + M_{14}I_4}\right) \tag{5.7}$$

This trivial ratio of currents gives a more accurate representation of the probe voltage than would be seen by a probe if all the probe voltage was induced by the current in that same quadrant. For example, $V_{p1corrected}$ is the probe voltage that would be seen on probe 1 if all the voltage was induced by current I_1 in quadrant 1. $V_{p1corrected}$ is then inputted into equation 5.1 as with a single probe. $M_{i,j}$ are the same cross-voltage induction factors as in section 5.2.2. Equation 5.7 must also be applied to the probe voltages when finding the capacitances as well for the solution to make sense. This correction does roughly account for the cross-voltage induction between a probe and other quadrants through differences in current, but it does not account for differences in parallel velocities and capacitances of quadrants. Consequently, this equation is an estimate at best.

Incorporating the correction of equation 5.7 to all probes and capacitances, the segmented alpha values for the high power operating point of 96.5 kV and 40 A are shown in Figure 5-9. The quadrant to quadrant alpha ranged from 1.28 to 1.44 with an

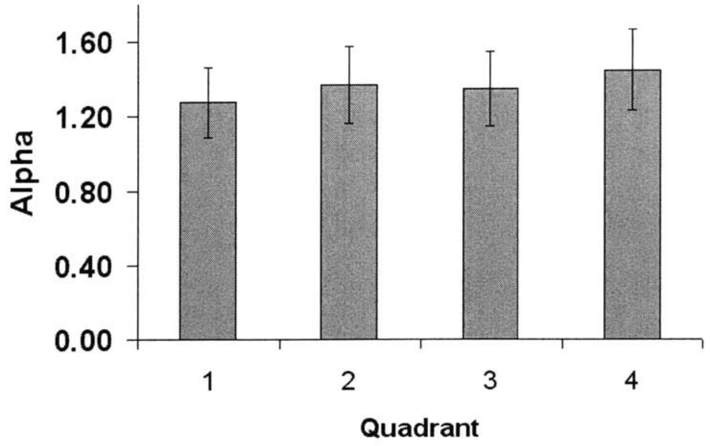

Figure 5-9: Measured alpha for the four azimuthal quadrants at 96.5 kV and 40 A.

average of 1.37. The average alpha of 1.37 is very close to the alpha of 1.4 predicted by simulation, but the high experimental error of ±15% prevented any quadrant to quadrant comparison of alpha to MICHELLE 3-D. Unfortunately, these probes could not validate the small differences in alpha predicted by MICHELLE .

5.4 Low-Frequency Oscillations

Although the segmented alpha probes failed to extract the azimuthal differences in alpha due to high experimental error, another interesting phenomenon was observed nearing the end of the experiment. Taking a closer look at the time domain signal of the alpha probes, there appeared to be coherent noise on the alpha probes signals. This observation prompted an investigation into the low-frequency oscillations seen on the probe signals. Performing the Fourier Transform on the time-domain alpha probe signals showed that low-frequency oscillations existed at a variety of frequencies including 6, 10, 52, and in the range of 100-160 MHz. Most interesting were narrow band oscillations in the 100-160 MHz range that were dependent on the beam parameters of voltage, magnetic field compression, and to a lesser extent the beam current. This frequency range coincides fairly well with the oscillation frequency of adiabatically trapped electrons indicative of potential hazardous beam instabilities.

5.4.1 100 MHz gyrotron oscillations

Over the last decade, there has been visible concern over instabilities caused by adiabatically trapped electrons. Brought to attention by high profile cases such as the 110 GHz Gycom tube for the DIII-D Tokamak at General Atomics [90] and the coaxial cavity gyrotron [91] at FZK in Karlsruhe, Germany, parasitic oscillations have caused disruptions in the diagnostic systems and have a detrimental effect on beam quality. The amplitude of the oscillations has been so great as to cause fear of damage to the RF diagnostic systems, while the presence of the oscillations provides clear indication of trapped electrons producing less than optimal gyrotron efficiency.

The trapped electrons are initially caused by the tail end of the velocity distribution, with a small percentage of electrons being reflected by the magnetic mirror in the gyrotron drift section. The reflected electrons are again reflected from the cathode potential at the gun side creating an adiabatic trap. The electrons will eventually escape either through asymmetries in the electric field or collisions with other electrons spending a total time in the trap from $2T_{||}$ to $10T_{||}$ [92]. The beam will ultimately reach a saturation point where the trapped electrons will be in an equilibrium state. As the reflected electrons accumulate in the trap, the increased space charge at the cathode will effectively decrease the accelerating voltage, lowering the average beam alpha and reducing the number of electrons in the tail end of the velocity distribution that are reflected. Thus the trap will only be able to sustain a certain amount of trapped charge for a given voltage. Liu and Antonsen [93] show that this accumulation of trapped electrons near the cathode surface will not only reduce alpha, but also induce an additional velocity spread of the beam further degrading the beam quality and gyrotron performance. These theoretical claims of beam degradation have been verified experimentally by Tsimring and Zapevalov [94] and Kuftin and Zapevalov [95] showing a decrease in alpha and increase of perpendicular velocity spread with the presence of reflected electrons.

As of now, the only theoretical explanations for the parasitic oscillations involve trapped electrons exciting stationary frequencies at either the cathode or beam tunnel acting as a low Q resonator as in [91]. These frequencies in [91] were found to be between 20 and 80 MHz for this particular gyrotron and had no dependence on beam parameters. The observed 100 MHz frequencies in other experiments have largely been attributed to space-charge potential oscillations in the electron beam numerically calculated with particle-in-cell codes [96-98], but there has not been a thorough theoretical model explaining the presence and physical origination of the oscillations. The root cause is assumed to be that of reflected electrons, but examining the instability causing the oscillations resulting from the trapped electrons is yet to be determined.

5.4.2 Experimental low-frequency oscillation observations

The oscillations observed on the 110 GHz gyrotron at MIT were found by taking the Fourier Transform of the time-domain alpha probe signals of a 500 MHz, 4Gs/s

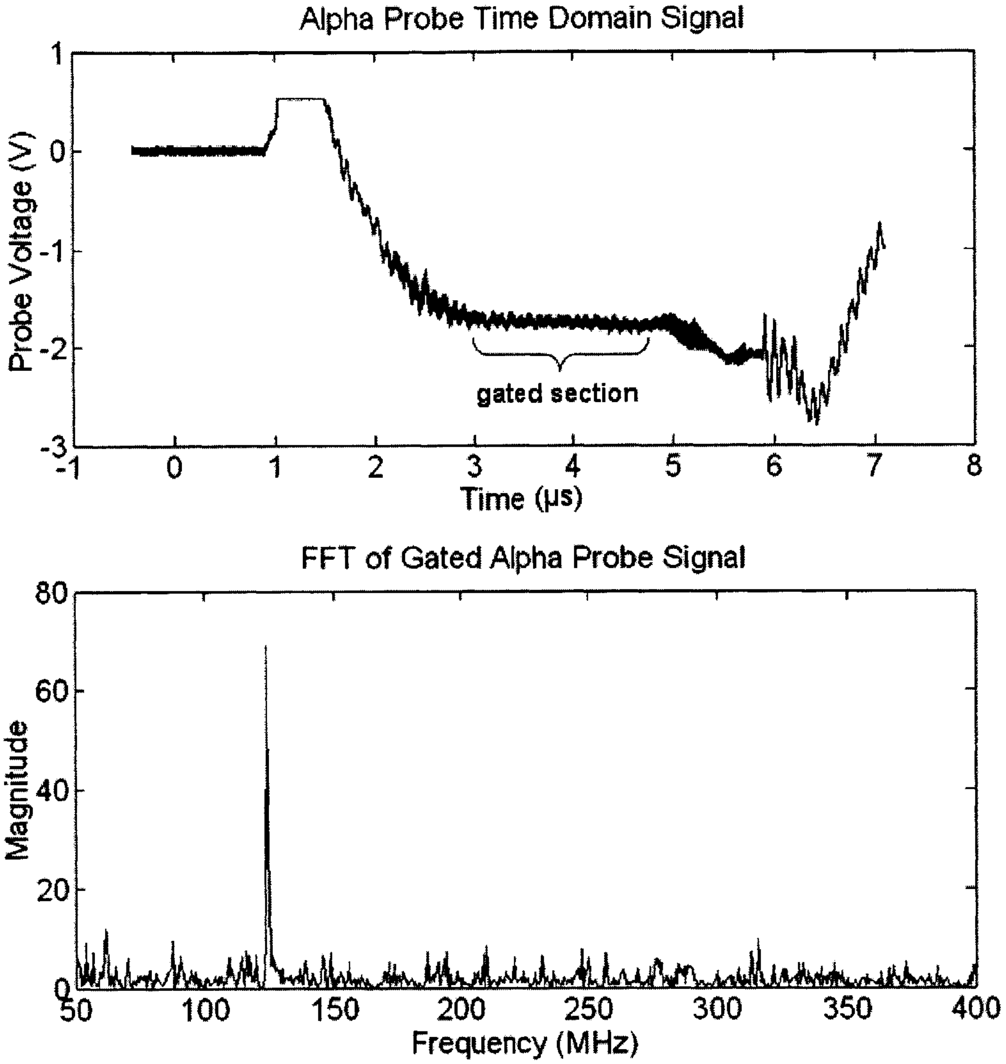

Figure 5-10: Alpha probe signal with low-frequency oscillations and corresponding Fourier transform of flat section of the voltage pulse. Taken at a 65 kV and 38 A.

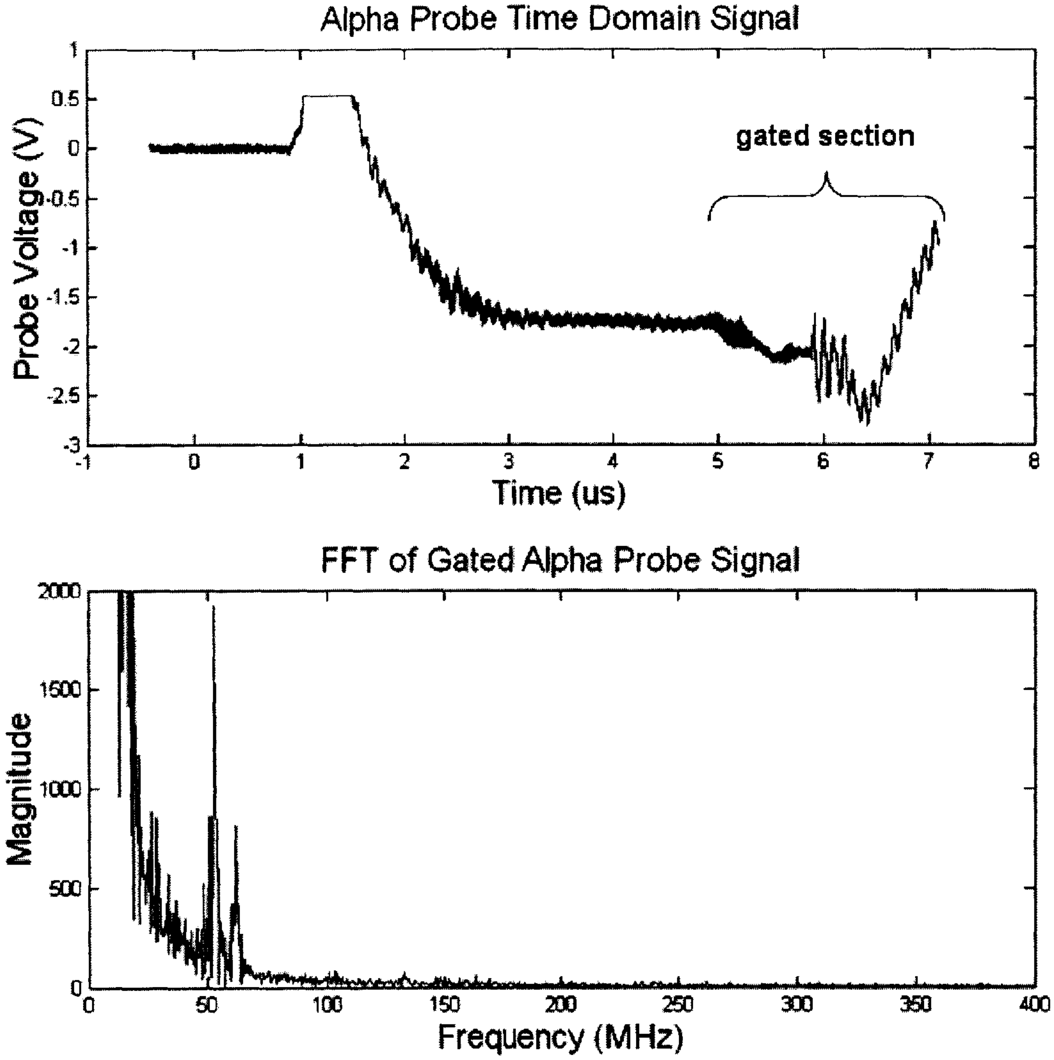

Figure 5-11: Alpha probe signal with low-frequency oscillations and corresponding Fourier transform of the transient section of the pulse. Taken at a 65 kV and 38 A.

oscilloscope as shown in Figure 5-10. The transform was taken over the flat section of the cathode voltage pulse as to ignore any oscillations during the transient phase of the pulse. The low-frequency oscillations had a bandwidth of about 1-2 MHz and varied frequency depending on the beam voltage, beam current, magnetic field, and magnetic compression ratio. Figure 5-11 shows the transform taken over the transient portion of the voltage pulse and shows the stationary frequency content on the alpha probes. Notice that there is a very strong signal around 52 MHz. This signal was mostly seen on the transient section of the pulse and did not change frequency with beam parameters. The 52 MHz signal appeared around 40 kV and was observed to become more pervasive as the voltage or magnetic compression was increased. Figure 11 also shows a strong ~11 MHz signal that was seen on the probes. Again, the ~11 MHz signal did not appear to be dependent on the beam parameters. These other frequencies certainly did exist, but this research focused on the frequency content most closely related to the transit time of the electrons in the adiabatic trap. The rest of the discussion will emphasize the ~100 MHz oscillations.

Though the oscillations were initially found serendipitously on the alpha probes, the oscillations were later found to be seen on the oscilloscope next to the gyrotron without any probes attached. Taking the Fourier Transform of the flat line oscilloscope signal with an open ended connection will produce the same frequencies as when the alpha probes are connected. Moving the oscilloscope away from the gyrotron will reduce the magnitude of the oscillations until no oscillations can be found. Turning off the gyrotron will also stop the oscillations. From these two observations and the fact that the frequency of oscillation changes with beam parameters, it was concluded that the oscillations were indeed coming from inside the gyrotron and not from some other spurious source of MHz radiation such as FM radio or from the voltage modulator used to pulse the gyrotron.

As noted before, the ~100 MHz oscillations are fairly close to the round trip transit time of electrons oscillating in the adiabatic trap assuming the conservation of the adiabatic moment $I_a = v_\perp^2 / B$. As shown by Tsimring [78], in order to find the electron transit time, the inverse of the electron axial velocity must be integrated over as function of the axial position from the cathode to the reflection plane expressed as

$$T = \int_0^{L_p} \frac{dx}{v_z(x)} \tag{5.8}$$

where L_p is the distance from the cathode to the electron reflection plane calculated by

$$L_p = L\left(1 - \sqrt{\frac{t_\perp - 1}{g - 1}}\right) \tag{5.9}$$

and

$$v_z(x) = \sqrt{v^2 - v_\perp(x)^2} = \sqrt{v^2 - v_{\perp 0}^2 \, B(x)/B_0} = v\sqrt{1 - t_\perp \, B(x)/B_0} \tag{5.10}$$

where B(x) is the magnetic field as a function of axial position x modeled as a bell-shaped distribution, v is the total velocity in operation space, L is the distance from the cathode to the interaction region and g is the magnetic compression ratio. $t_\perp$ is defined as the ratio of the perpendicular velocity at the cathode to the critical cathode perpendicular velocity in which electrons will be reflected from the magnetic mirror. Adiabatically,

$$\frac{\gamma_o^2 v_{\perp o}^2}{B_o} = \frac{\gamma_k^2 v_{\perp k}^2}{B_k} \tag{5.11}$$

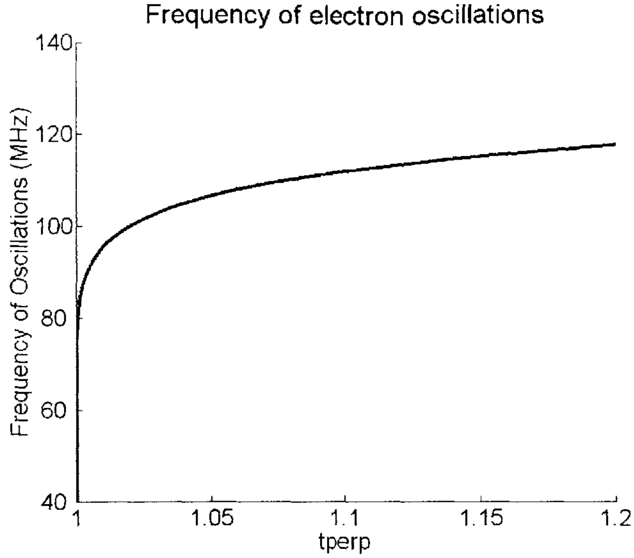

Figure 5-12: Oscillation frequency of a single particle at 70 kV in the adiabatic trap vs. the ratio of perpendicular energy to electron total energy as calculated from [78].

where "o" denotes the interaction space (peak magnetic field) and "k" denotes at the cathode. The perpendicular velocity in operation space from adiabatic theory is then

$$v_{\perp o} = \frac{1}{\gamma_o}\sqrt{\frac{B_o}{B_k}}v_{\perp k} \tag{5.12}$$

Electrons will be reflected when $v_\perp = v_{tot}$ where v_{tot} is determined by the accelerating voltage and is assumed homogeneous for all electrons. There exists a critical perpendicular velocity $v_{\perp k_{critical}}$ at the cathode in which electrons with more perpendicular velocity than this value will be reflected by the magnetic mirror before reaching the peak magnetic field.

$$v_{\perp k_{critical}} = v_{tot}\gamma_o\sqrt{\frac{B_k}{B_o}} \tag{5.13}$$

All the values of $v_{\perp k}$ over $v_{\perp k_{critical}}$ will be reflected. $t_{\perp}$ is then defined as this ratio of

$$t_{\perp} = \frac{v_{\perp k}}{v_{\perp k_{critical}}} \qquad (5.14)$$

$t_{\perp}$ is only useful for values greater than one since if $t_{\perp}$ was less than one, the electron would not be reflected by the magnetic mirror. The electron frequency is then found from the relation of $f_{osc} = 1/2T$ and eqn. 5.8. The trap frequency can be computed for a given voltage, B_0, and compression ratio as shown in Figure 5-12.

Experimentally, the shift in the ~100 MHz oscillation frequency as a function of the beam parameters of voltage, current, and magnetic compression are shown in Figures 5-13 and 5-14. Figure 5-13 depicts the frequency shift as the voltage is increased for a fixed magnetic compression ratio of 25. Unlike other experiments by Kas'yanenko et al. [98], the frequencies observed here decrease as the voltage is increased. The frequencies also increase slightly with increasing beam current. Figure 5-14 shows the frequency dependence on the magnetic compression ratio. At a fixed voltage and current, the parasitic frequency increases with compression, consistent with the motion of the oscillation frequency of an adiabatically trapped electron. As the magnetic compression is increased, alpha increases and in turn the reflection plane for electrons with insufficient axial energy will be decreased. As a result, the length of the adiabatic trap is shortened and the frequency of oscillation of electrons in the trap will increase consistent with the experimental observations. The data compiled in Figures 5-13 and 5-14 displays only the frequency versus different beam parameters. The amplitude of the oscillations at varying beam parameters was not easily quantifiable due to the lack of repeatability. One to three

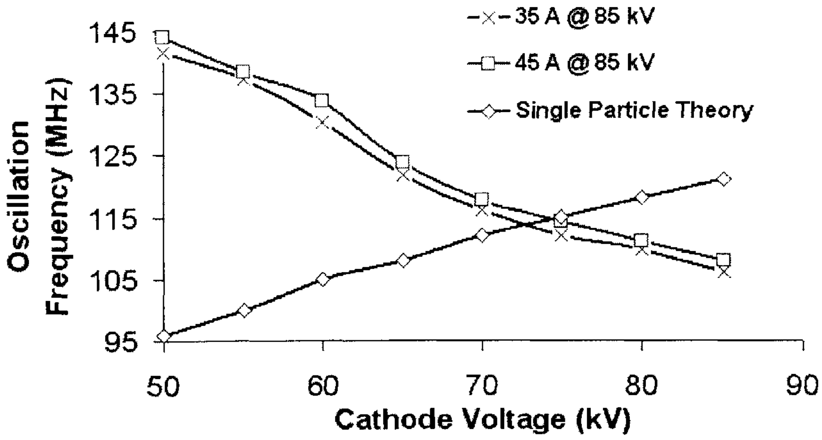

Figure 5-13: Frequency of parasitic oscillations vs. cathode voltage from experiment and for a single adiabatically trapped electron with $t_{\perp} = 1.1$. Experimental data is shown for two different current curves at a magnetic compression of 25. Frequency slightly increases with increased current in experiment.

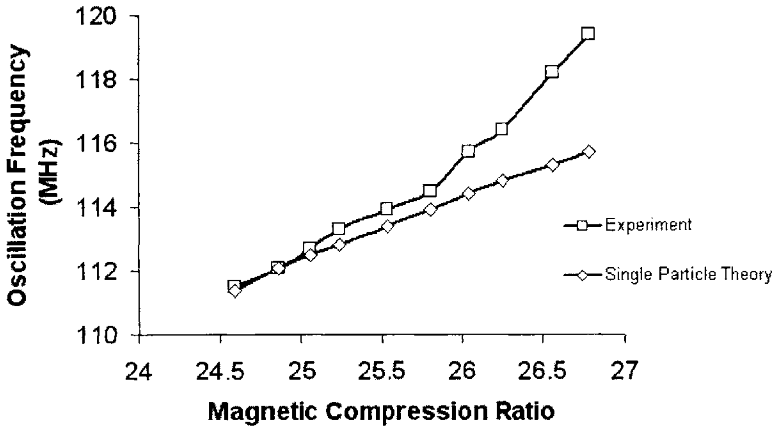

Figure 5-14: Change in parasitic oscillation frequency vs. magnetic compression ratio at a beam voltage of 70kV and current of 36 A and the corresponding shift in the frequency calculated for single adiabatically trapped electron.

orders of magnitude generally separated the noise floor of the Fourier Transform from the oscillation power.

In addition, Figures 5-13 and 5-14 show the change in frequency as predicted theoretically by the oscillation frequency of a single electron. As the voltage is increased, the frequency of a single electron with a fixed $t_\perp$ of 1.1 has the opposite behavior as found in the experiment. Increasing the voltage caused the frequency to decrease in experiment while the single particle theory predicts an increase in frequency due to an increase in average parallel velocity. The simple single particle theory does not, however, account for space charge effects from electrons in the adiabatic trap, nor does it account for changes in the velocity spread of the beam at different voltages. The behavior of the single particle theory as a function of magnetic compression does show the same tendency as seen experimentally of the frequency increasing with compression. Though the magnetic compression behavior is fairly consistent between the single particle theory and experiment, the opposite tendencies of the oscillation frequency as a function of voltage indicate that this phenomenon cannot be well described by this theory in its present form. A more thorough model must be constructed to describe the observed oscillations.

The parasitic oscillations were not observed for all beam operating points. As displayed in Figure 5-15, there exists a fairly defined region in I-V space where stable oscillations occur. Oscillations were unable to be seen below 24 Amps of beam current at 45 kV. The current threshold tended to increase as voltage increased as well. Oscillations were also not seen below 45 kV or above 90 kV. It is possible that above 90 kV, the current threshold was too high to obtain stable oscillations. Due to high pressure

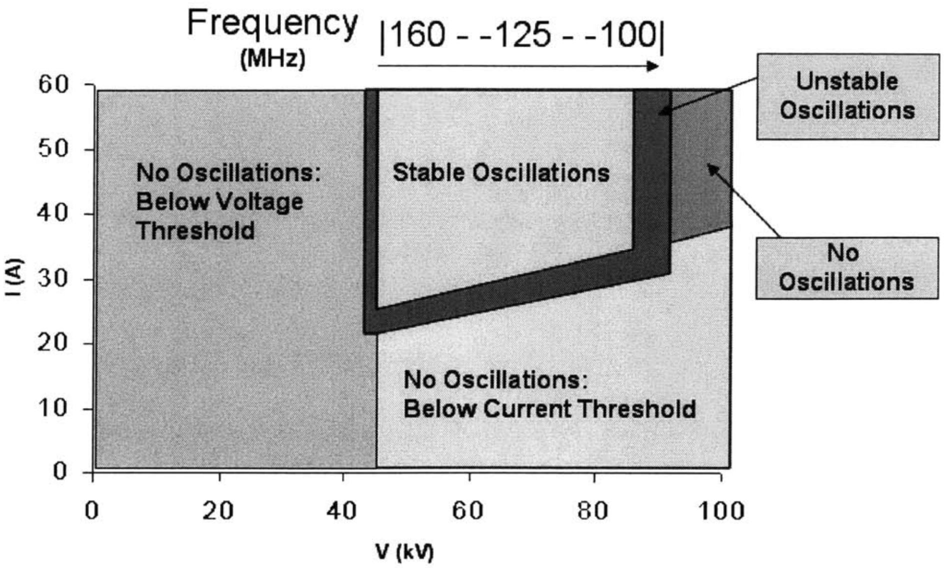

Figure 5-15: Regions of stable, unstable, and absent low-frequency oscillations in I-V space.

in the tube at higher currents, current was generally limited to stay below 50 A.

Attempts to isolate the source of the oscillations unfortunately came with little success. Since the frequency could be detected all around the gyrotron and the alpha probes were located at only one axial position within the tube, it was impossible to determine the oscillation source within the tube. The ~100 MHz oscillations were not seen on other diagnostic equipment such as the RF pulse. The noise floor on the RF was found to be much too high to enable resolution of the oscillation frequency when measured using a heterodyne mixer frequency detection system or the RF diode.

After extensive data was taken, the frequencies continued to be observed in the region shown in Figure 5-15. The oscillations tended to increase slightly with increased pressure in the tube, but remained relatively constant within the two months of data taking. Throughout the entire experimental observation duration, no stable ~100 MHz oscillations were observed at the high-efficiency operating point at 96 kV and 40 A. This could possibly be the result of the current threshold being too high at 96 kV to excite the oscillations. The oscillations seen in this experiment were not as severe as in other experiments [96, 97] and did not cause diagnostic disruption using 3 μs pulses. It is possible that the oscillations could manifest into a greater problem as the pulse length is increased. Further experimental work needs to be done in an effort to suppress the oscillations found in industry and a thorough theoretical framework must be completed to explain the origin of and possible remedies to this phenomena.

5.5 Summary and Conclusions

The motivation, theoretical background, and experimental results were presented for an attempt to experimentally measure beam alpha at full voltage operation in four azimuthally segmented quadrants. Four capacitive probes were implemented in the existing 1.5 MW gyrotron at MIT to measure alpha as the beam entered the resonant cavity. The established theory for alpha measurement of the entire beam using an unsegmented capacitive probe was described in detail. To extend the theory to four azimuthally segmented probes, the voltage induced on each probe from other quadrants must be taken into account by knowing the cross-voltage induction factors. These factors are defined as a ratio of the voltage induced on a quadrant's probe from current in a different quadrant to the voltage induced on the quadrant's probe from the current in that same quadrant. All of the cross-voltage induction factors were found using MICHELLE as a three-dimensional electrostatic field solver. Using the cross-voltage induction factors and solving for alpha for each quadrant using the simulated probes, alpha for each quadrant compared very closely to the alpha for each quadrant obtained directly from the particle trajectories in MICHELLE.

Solving for segmented alpha experimentally proved to be more difficult than in simulation. Experimental error was much too high to have the resolution needed to find the small differences in alpha as predicted by MICHELLE. Consequently, the experiment was unable to verify MICHELLE. Quadrant to quadrant alpha ranged from 1.28-1.44 with an average of 1.37, remarkably close to the design value of 1.4.

In addition to the attempt of measuring segmented alpha, the probes were also used to diagnose the presence of low-frequency oscillations suggesting the existence of an instability on the beam. These frequencies ranged from 100 to 160 MHz and were tunable by changing the beam voltage, current, and the magnetic compression ratio. In addition, the frequencies were only observable for a specific parameter region of voltage and current space. It is hypothesized that adiabatically trapped electrons could potentially be the cause of the instability, but simply modeling the oscillations as the frequency of a trapped electron is not sufficient to explain the tendencies observed in experiment. As of this thesis, trapped electrons have yet to be verified with an adequate model to describe the phenomenon that accurately predicts the experimental data, but still exists as a strong contender for the cause of the instability.

Future segmented alpha probe experiments may want to concentrate on a more direct method of extracting azimuthally dependent alpha. Such an experiment could be similar to velocity spread measurements performed by Glyavin et al. [71], but with an azimuthally segmented collector. These experiments are usually performed in a scaled model regime and are also plagued with a high amount of experimental error. However, more reliable qualitative behavior may be extracted from this type of directly measured experiment that does not have to take into account the accuracy of the cross talk between the probes and other quadrants as in the case of capacitive probes. Regardless of the methods used, non-uniform emission will continue to be studied for its effect on beam quality, mode interaction, and collector performance well into the future.

Upcoming research on the low-frequency oscillations will want to focus on developing a model for the observed oscillations and experimental techniques to suppress the instability. The very existence of the instability is a concern for long-term beam stability for long-pulse and continuous wave operation. Appropriate modeling and gyrotron design must be done to prevent the occurrence of the 100 MHz oscillation for the next generation of high-power fusion gyrotrons.

Chapter 6

Conclusion

This work is comprised of a compilation of recent studies on an azimuthally non-uniform electron beam of a 96 kV, 40 A magnetron injection gun for a 1.5 MW, 110 GHz gyrotron oscillator. Non-uniform emission has been previously theorized to lower efficiency in MW gyrotrons essential to providing experimental tokamak fusion reactors with plasma heating. This research is an effort to correctly model and experimentally validate the detrimental effects on an azimuthally inhomogeneous electron beam on gyrotron efficiency. To do so, a number of experimental and computer simulation tools were employed as discussed in the subsequent paragraphs.

The experimentally obtained emission non-uniformity profile for two cathodes was presented for the 96 kV, 40 A magnetron injection gun used in the 1.5 MW gyrotron at MIT. The first cathode is presently installed on the experimental gyrotron and the second is the first of three separate cathodes identical to the first that are to be tested for emission uniformity. The presently installed cathode's uniformity profile was measured using a slotted collector that rotates on the beam axis while the new cathode was tested on the Calabazas Creek cathode tester. The remaining two cathodes will be tested at CCR as well.

Non-uniform emission has become a potential culprit of poor efficiency and measuring the present uniformity profile was the first step in thoroughly modeling the phenomenon in a 3-D gun code. This experiment accurately assesses the azimuthal cathode emission to serve as an input into MICHELLE 3-D electron trajectory code and to aid in the calculation of experimental azimuthally segmented alpha values. The present cathode was found to have a significantly high level of non-uniformity with azimuthal current differences reaching three to one at certain angles. The measurement of the second cathode is an ongoing effort to characterize the uniformity profile of three new identical cathodes to the one presently installed on the experimental gyrotron. The preliminary results for the first of the new cathodes are presented. Further measurements in the upcoming months will have to be done at CCR to assure full activation of this cathode at measurement time. Once the other two cathodes have been manufactured, they will be similarly tested. The cathode with the best uniformity profile will then be installed on the experimental gyrotron for forthcoming efficiency experiments.

The first full 3-D simulation of a magnetron injection gun from the cathode to the cavity has been presented using MICHELLE 3-D. A uniform MICHELLE 3-D beam has shown very good comparisons in the beam pitch factor and perpendicular velocity spread to EGUN and a 2-D MICHELLE model. MICHELLE 3-D was run using approximately 2.4 million hexahedrons and tetrahedrons providing an adequate self-consistent solution.

After benchmarking to established 2-D codes, MICHELLE 3-D was used to extensively model the effects on alpha and velocity spread of an azimuthally non-uniform emitting beam in contrast to a uniform beam. Using the experimentally obtained azimuthal beam emission profile from the rotating current probe, MICHELLE found that the beam non-uniformity had only a very small effect on the beam alpha and velocity spread. The velocity spread increased from 1.8 % for a uniform beam to 2.05 % for a non-uniform beam and the average pitch factor remained within 1-2% of the design value of 1.4. The very small increase in velocity spread would have a negligible effect on the device efficiency. Modeling with more extreme uniformity, such as a ten to one max to min sinusoidal variation, produces an overall velocity spread of 3.15%, an increase of 1.35 %. This extreme non-uniformity does produce a velocity spread increase capable of decreasing gyrotron efficiency by 1-2 %, but is still rather small compared to the velocity spread increase necessary to produce the efficiency degradations seen in some industrial gyrotrons. The increase of velocity spread at severe non-uniformity is most likely due to the increased local space charge of the high current density regions and the spreading of average perpendicular velocities for regions of different current density.

The motivation, theoretical background, and experimental results were presented for an attempt to experimentally measure beam alpha at full voltage operation in four azimuthally segmented quadrants. Four capacitive probes were implemented in the existing 1.5 MW gyrotron at MIT to measure alpha as the beam entered the resonant cavity. The established theory for alpha measurement of the entire beam using an unsegmented capacitive probe was described in detail. To extend the theory to four azimuthally segmented probes, the voltage induced on each probe from other quadrants must be taken into account by knowing the cross-voltage induction factors. These factors are defined as a ratio of the voltage induced on a quadrant's probe from current in a different quadrant to the voltage induced on the quadrant's probe from the current in that same quadrant. All of the cross-voltage induction factors were found using MICHELLE as a three-dimensional electrostatic field solver. Using the cross-voltage induction factors and solving for alpha for each quadrant using the simulated probes, alpha for each quadrant compared very closely to the alpha for each quadrant obtained directly from the particle trajectories in MICHELLE.

Solving for segmented alpha values experimentally proved to be more difficult than in simulation. Experimental error was much too high to have the resolution needed to find the small differences in alpha as predicted by MICHELLE. Consequently, the experiment was unable to verify MICHELLE. Quadrant to quadrant alpha ranged from 1.28-1.44 with an average of 1.37, remarkably close to the design value of 1.4.

In addition to the attempt of measuring segmented alpha, the probes were also used to diagnose the presence of low-frequency oscillations suggesting the existence of an instability on the beam. These frequencies ranged from 100 to 160 MHz and were tunable by changing the beam voltage, current, and the magnetic compression ratio. The frequencies were only observable for a specific parameter region of voltage and current space. It is hypothesized that adiabatically trapped electrons could potentially be the cause of the instability, but simply modeling the oscillations as the frequency of a trapped electron is not sufficient to explain the tendencies observed in experiment. As of this thesis, trapped electrons have yet to be verified with an adequate model to describe the phenomenon that accurately predicts the experimental data. Upcoming research on the low-frequency oscillations will want to focus on developing a model for the observed oscillations and experimental techniques to suppress the instability. The very existence of the instability is a concern for long-term beam stability for long-pulse and continuous wave operation. Appropriate modeling and gyrotron design must be done to prevent the occurrence of the 100 MHz oscillation for the next generation of high-power fusion gyrotrons.

This research will certainly continue into the future. Many experiments can be designed to further the knowledge of how a non-uniform beam affects gyrotron efficiency such as comparing the gyrotron performance of two identical fully operational gyrotrons with different emission uniformity profiles. MIT will investigate this experiment in the near future by measuring the output power and efficiency of a uniform cathode and compare these results to those measured previously with a three to one varying emission distribution. As computing memory capabilities and processor speed continues to rise, more accurate 3-D modeling can be done with ray-tracing or particle-in-cell codes to continue modeling of 3-D effects in magnetron injection guns. PIC codes may also be employed to simulate the beam instability producing the 100 MHz parasitic oscillations found in this gyrotron.

Bibliography

[1] M. Bellis, "The History of Vacuum Tubes," About *inc.,* 2005 <http://inventors.about.com/library/inventors/blvacuumtubes.htm >

[2] "The Vacuum Tube," *PBS Online*, 1999, <http://www.pbs.org/transistor/science/events/vacuumt.html>

[3] G. R. Kilgore, "Recollections of pre-World War II magnetrons and their applications," *IEEE Trans. Electron Devices*, v. ED-31, pp. 1593-1605, Nov. 1984.

[4] N. C. Luhmann, Jr., G. S. Nusinovich, and D. M. Goebel, "Historical Highlights," in *Modern Microwave and Millimeter-Wave Power Electronics*, edited by R. J. Barker, N. C. Luhmann, J. H. Booske, G. S. Nusinovich, Wiley-IEEE Press, April 2005.

[5] R. H. Varian and S. F. Varian, "A high frequency oscillator and amplifier," *J. Appl. Phys.*, v. 10, pp. 321-337, 1939.

[6] R. Kompfner and N. T. Williams, "Backward Wave Tubes," *Proc. IRE.* v. 51, pp. 1602-1611, 1953.

[7] R. M. Phillips, "The ubitron, a high-power traveling wave tube based on periodic beam interaction in unloaded waveguide, *IRE-ED*, v. ED-7, pp. 231-241, 1960.

[8] L. R. Elias, W. M. Fairbank, J. M. J. Madey, H. A. Schwettman, and T. I. Smith, *Phys. Rev. Lett.* v. 36, pp. 710, 1976.

[9] S. V. Yadavali, "On the performance of a class of hybrid tubes," *Proc. IRE.* v. 48, 263, 1960.

[10] Ta, Yeou, "Generation des ondes Millimetriques et Submillimetriques, in *Tubes pour Hyperfrequences travaue du 5th Congres International*, Paris, pp. 151-156, 1964.

[11] G. Caryotakis, "The klystron: A microwave source of surprising range and endurance," *Phys. Plasmas*, v. 5, no. 5, pp. 1590-1598, May 1998.

[12] V. V. Alikaev, et al., "Electron cyclotron heating at the TM-3 Tokamak," *JETP Lett.* v. 15, pp. 27-29, 1972.

[13] V. E. Golant, et al., "Experiments on microwave heating of plasmas at Tuman-2 installation," *J. Tech. Phys.*, v. 42, pp. 488-496, 1972.

[14] H. J. Wolkstein, *RCA Review*, v. 46, no. 4, pp. 484-495, Dec. 1985.

[15] G. Caryotakis, "Development of X-band klystron technology at SLAC," *Proc. Of the 1997 Particle Acc. Conf.*, v. 3, Piscataway, NJ: IEEE, pp. 2894-2898, 1997.

[16] B. Badelek et al., "The photon collider at TESLA," *Int. J. Mod. Phys.*, v. 19, no. 30, 10, pp. 5097-186, Dec. 2004.

[17] A. Balkcum, E. Wright, H. Bohlen, F. Friedlander, M. Cattelino, L. Cox, E. Eisen, S. Lenci, B. Stockwell and L. Zitelli., "Development of a 10 MW, L-Band Multiple Beam Klystron for TESLA," *IEEE Int. Conf. Plasma Sci.*, Cat. No. 02CH37340, p. 130, 2002.

[18] D. K. Abe, D. E. Pershing, K. T. Nguyen, F. N. Wood, R. E. Myers, E. L. Eisen, M. Cusick, and B. Levush, "Demonstration of an S-Band, 600-kW, Fundamental-Mode Multiple-Beam Klystron," *IEEE Electron Device Lett.* v. 26, no. 8, Aug. 2005.

[19] M. Blank et al., "Demonstration of a 10 kW average power 94 GHz gyroklystron amplifier," *Physics of Plasmas*, v. 6, no. 12, pp. 4405, 1999.

[20] K. E. Hackett, "Active Denial Technology," *Air Force Research Laboratory Technology Horizons Online*, http://www.afrlhorizons.com/Briefs/Sept01/DE0101.html

[21] K. E. Kreischer, C. Farrar, R. Griffin, R. Temkin, and J. Vieregg, "A 250 GHz gyrotron for NMR spectroscopy." In *ICOPS 2000 IEEE Conference Record – Abstracts. 27th IEEE International Conference on Plasma Science*, pp. 198, New Orleans, LA, USA, June 2000.

[22] M. K. Hornstein, V. S. Bajaj, R. G. Griffin, K. E. Kreischer, I. Matovsky, M. A. Shapiro, and R. J. Temkin, "Design of a 460 GHz second harmonic gyrotron oscillator for use in dynamic nuclear polarization," *Conf. Digest, 27th Int. Conf. on Infrared and Millimeter Waves*, Piscataway, NJ: IEEE, pp. 193-4, 2002.

[23] A. L. Goldenberg and A. G. Litvak, "Recent progress of high-power millimeter wavelength gyrodevices," *Phys. Plasmas*, v. 2, no. 6, pp. 2262-2572, June 1995.

[24] W. E. Garrigus and M. I. Glick, "Multi-Octave high-power twt operation," *Microwave Journal*, v. 18, pp. 35-40, May 1975.

[25] S. Choroba, J. Hameister, and S. Jarlkapov, "Performance of an S-band Kylstron at an Output Power of 200 MW," in *Proceedings of the XIX International Linac Conference*, v. 2, p. 917, August 1998.

[26] H. Alfven and D. Romell, "A new electron tube; the strophotron," *Proc. IRE*, v. 42, pp. 1239, 1954.

[27] R. Q. Twiss, Radiation transfer and the possibility of negative absorption in radio astronomy. *Aust. J. Phys.*, v. 11, pp. 564-579, 1958.

[28] J. Schneider, "Stimulated emission of radiation by relativistic electron in magnetic field," *Phys. Rev. Lett.*, v. 2, pp. 504-505, 1959.

[29] A. V. Gaponov, Addendum, *Izv, VUZ Radiofizika*, v. 2, pp. 837, 1959 an addendum to A. V. Gaponov, "Interaction between electron fluxes and electromagnetic waves in waveguides," *Izv. VUZ Radiofizika*, v. 2, pp. 450, 1959.

[30] R. Pantell, "Electron beam interaction with fast waves," *Proceedings, Symposium on Millimeter Waves*, Polytechnic Institute of Brooklyn, March 31- April 2, 1959, Polytechnic Press, New York, 1959.

[31] J.L Hirshfield and J.M. Wachtel, "Electron Cyclotron Maser," *Physical Review Letters*, v. 12, pp. 553-536, May 11, 1964.

[32] K. R. Chu, "The electron cyclotron maser," *Reviews Modern Physics*, v. 76, April 2004.

[33] K. L. Felch, B. G. Danly, H. R. Jory, K. E. Kreischer, W. Lawson, B. Lavush, and R. J. Temkin, "Characteristics and applications of fast-wave gyrodevices," *Proc. IEEE* v. 87, pp 752-781, 1999.

[34] K. Felch, M. Blank, P. Borchard, P. Cahalan, S. Cauffman, T. S. Chu and H. Jory, "Recent Advances in Increasing Output Power and Pulse Duration in Gyrotron Oscillators," in Proceedings of the *Joint 30th Intl. Conf. on Infrared and Millimeter Waves & 13th Intl. Conf. on Terahertz Electronics*, Williamsburg, VA, 2005.

[35] B. Piosczyk, A. Arnold, G. Dammertz, O. Dumbrajs, M. Kuntze, and M. K. Thumm, "Coaxial Cavity Gyrotron- Recent Experimental Results," *IEEE Trans. Plasma Sci.*, v. 30, no. 3, June 2002.

[36] A. G. Litvak, V. E. Myasnikov, S. V. Usachev, L. G. Popov, M. V. Agapova, V. O. Nichiporenko, G.G. Denisov, A. A. Bogdashov, A. Ph. Gnedenkov, V. I. Ilyin, V. N. Ilyin, D. V. Khmara, A. N. Kostyna, A. N. Kuftin, V. K. Lygin, M. A. Moiseev, V. I. Malygin, E. A. Solujanova, V. E. Zapevalov, E. M. Tai, "Development of 170 GHz/1 MW/50%/CW gyrotron for ITER," *Conference Digest of the 29th International Conference on Infrared and Millimeter Waves*, Karlsruhe, Germany, 2004.

[37] K. Sakamoto, A. Kasugai, Y. Ikeda, K. Hayashi, K. Takahashi, S. Moriyama, M. Seki, T. Kariya, Y. Mitsunaka, T. Fujii, and T. Imai, "Development of 170 and 110 GHz gyrotrons for fusion devices," *Nucl. Fusion*, v. 43, pp. 729-737, 2003.

[38] V. S. Bajaj, C. T. Farrar, M. K. Hornstein, I. Mastovsky, J. Vieregg, J. Bryant, B. Elena, K. E. Kreischer, R. J. Temkin, and R. G. Griffin, "Dynamic nuclear polarization at 9T using a novel 250 GHz gyrotron microwave source," *J. Magnetic Resonance*, v. 160, pp. 85-90, 2003.

[39] N. I. Zaystev, T. B. Pankratova, M. I. Petelin, and V. A. Flyagin. "Millimeter- and submillimeter-wave gyrotrons," *Radio Eng. Electron Phys*, v. 19, no. 5, pp. 103-107, May 1974.

[40] M. K. Hornstein, V. S. Bajaj, R. G. Griffin, K. E. Kreischer, I. Mastovsky, M. A. Shapiro, J. R. Sirigiri, and R. J. Temkin, Second harmonic operation at 460 GHz and broadband continuous frequency tuning of a gyrotron oscillator. *IEEE Trans. Electron Devices*, v. 52, no. 5, pp 798-807, May 2005.

[41] T. Idehara, I. Ogawa, S. Mitsudo, M. Pereyaslavets, N. Nishida, K. Yoshida, "Development of Frequency Tunable, Medium Power Gyrotrons (Gyrotron FU Series) as Submillimeter Wave Radiation Sources," *IEEE Tran. Plasma Sci.*, v. 27, no. 2, April 1999.

[42] M. Thumm, "Free electron masers vs gyrotrons: prospects for high-power sources at millimeter and submillimeter wavelengths," *Nucl. Instrum. Methods Phys. Res. A*, v. 483, pp. 186-194, 2002.

[43] ITER Website, < http://www.iter.org/index.htm >, 2005.

[44] M. Thumm, "MW gyrotron development for fusion applications," *Plasma Phys. Control. Fusion*, **v.** 45 A143-A161, 2003.

[45] G. S. Nusinovich, "Introduction to the Physics of Gyrotrons," The John Hopkins University Press, 2004.

[46] M. V. Kartikeyan, E. Borie, M. K. A Thumm, "Gyrotrons: High-Power Microwave and Millimeter Wave Technology," Springer-Verlag Berlin Heidelberg, 2004.

[47] M. I. Petelin, "One century of cyclotron radiation," *IEEE Trans. Plasma Sci.*, **v**. 27, no. 2, pp. 294-302, April 1999.

[48] J. M. Baird, "Gyrotron Theory," in *High-Power Microwave Sources*, edited by V. L. Granatstein, and I. Alexeff, Artech House, 1987.

[49] V. A. Flyagin, A. V. Gaponov, M. I. Petelin, and V. K. Yulpatov, "The Gyrotron," *IEEE Trans. On Micro. Theory and Tech.*, **v**. MTT-25, no. 6, June 1977.

[50] K. R. Chu and J. L. Hirshfield, "Comparative study of the axial and azimuthal bunching mechanisms in electromagnetic cyclotron instabilities," *Phys. Fluids*, **v**. 21, pp. 461-466, 1978.

[51] A. W. Fliflet, "Linear and non-linear theory of the Doppler-shifted cyclotron resonance maser based on TE and TM waveguide modes," *Int. J. Electronics*, v. 61, no. 6, pp. 1049-1080, 1986.

[52] A. V. Gaponov, Instability of a system of excited oscillators with respect to electromagnetic perturbations, *Sov. Phys. JETP* v. 12, 232-236. 1961.

[53] N. A. Krall and A. W. Trivelpiece, Principles of Plasma Physics. McGraw-Hill, New York, 1973.

[54] P. Sprangle and W. M. Manheimer, "Coherent Nonlinear Theory of a Cyclotron Instability," *Phys. Fluids*, v. 18, pp. 224-230, 1975.

[55] V. L. Bratman, N. S. Ginzburg, G. S. Nusinovich, M. I. Petelin, and P. S. Strelkov, *Int. J. Electron.*, v. 51, 541, 1981.

[56] A. W. Fliflet, K. R. Chu, M. E. Read, and R. Seeley, "Self-consistent field theory for gyrotron oscillators: application to a low Q gyromonotron," *Int. J. of Electronics*, v. 53, pp. 505-521, Dec. 1982.

[57] B. G. Danly and R. J. Temkin, "Generalized nonlinear harmonic gyrotron theory," *Phys. Fluids*, v. 29 no. 2, Feb. 1986.

[58] G. S. Nusinovich and R.E. Erm, *Elektron. Tekh.*, Ser. 1, Elektron. SVCh, 55. 1972.

[59] R. L. Schriever and C. C. Johnson, *Proc. IEEE*, v. 54, no. 12, p. 2029, Dec. 1964.

[60] A. V. Gaponov, et al., *JETP Letters*, v. 2, p.267, 1965.

[61] J. M. Baird and W. Lawson, "Magnetron injection gun (MIG) for gyrotron applications," *Int. J. Electronics*, v. 61, no. 6, pp. 953-967, 1986.

[62] J. L. Cronin, "Modern dispenser cathodes," *IEEE Proceedings*, v. 12, pp. 19-32, 1981.

[63] J. Petillo, K. Eppley, D. Panagos, P. Blanchard, E. Nelson, N. Dionne, J. Deford, B. Held, L. Chernyakova, W. Krueger, S. Humphries, T. McClure, A. Mondelli, J. Burdette, M. Cattelino, R. True, K. Nguyen, B. Lavush, "The MICHELLE Three-Dimensional Electron Gun and Collector Modeling Tool: Theory and Design," *IEEE Trans. Plasma Sci.*, v. 30, no.3, June 2002.

[64] W. B. Herrmannsfeldt. EGUN: An electron optics and gun design program. *Technical Report SLAC-0331 UC-28, Stanford Linear Accelerator Center, Stanford,* California, October 1988.

[65] SH. E. Tsimring, "On the spread of velocities in helical electron beams," *Radiophys. Quantum Electron,* v. 15, pp. 952-961, 1972.

[66] Amaze 3D Simulation Suite, Field Precision Inc. 2004, www.fieldp.com.

[67] A. S. Gimour Jr., "Microwave Tubes," Artech House, Inc., Norwood, MA, 1986.

[68] G. S. Nusinovich, A. N. Vlasov, M. Botton, T. M. Antonsen, Jr., S. Cauffman, K. Felch, "Effect of the azimuthal inhomogeneity of electron emission on gyrotron operation," *Phys. Plasmas,* vol. 8, no. 7, pp. 3473-3479, 2001.

[69] J. G. Pagonakis and J. L. Vomvoridis, "Evolution of an Electron Beam With Azimuthal Density Nonuniformity in a Cylindrical Beam Tunnel," *IEEE Trans. Plasma Sci.*, v. 32, no. 3, June 2004.

[70] T.L. Grimm, K. E. Kreischer, and R. J. Temkin, "Experimental study of a megawatt 200-300 GHz gyrotron oscillator," *Phys. Fluids B,* v. 5, no. 11, pp. 4135-4143, 1993.

[71] Dammertz et al., "Experimental Results on the 140 GHz, 1MW, CW Gyrotrons for the Stellerator W7-X," *Proc. of the International Conference on Infrared and Millimeter Waves,* Williamsburg, VA 2005.

[72] M. Y. Glyavin, A. L. Goldenberg, A. N. Kuftin, V. K. Lygin, A. S. Postnikova, and V. E. Zapevalov, "Experimental studies of gyrotron electron beam systems," *IEEE Trans. Plasma Sci.*, v. 27, no. 2, pp. 474-483, April 1999.

[73] J. P. Anderson, S. E. Korbly, and R. J. Temkin, "Design and Emission Uniformity Studies of a 1.5-MW Gyrotron Electron Gun," *IEEE Trans. Plasma Sci.*, vol.30, pp. 2117-2123, Dec. 2002.

[74] R. Advani, J. P. Hogge, K. E. Kreischer, M. Pedrozzi, M. E. Read, J. R. Sirigiri, and R. J. Temkin, "Experimental investigation of a 140-GHz coaxial gyrotron oscillator," *IEEE Trans. Plasma Sci.*, v. 29, no. 6, pp. 943-50, Dec. 2001.

[75] M. Botton, T. M. Antonsen Jr., B. Levush, A. Vlasov, and K. Nguyen, "MAGY: A time dependent code for simulation of electron beam devices," *IEEE Trans. Plasma Sci.*, v. 26, no. 3, pp. 882-892, June 1998.

[76] J. P. Anderson, R. J. Temkin, and M. A. Shapiro, "Experimental Studies of Local and Global Emission Uniformity for a Magnetron Injection Gun," *IEEE Trans. Plasma Sci.*, v. 52, no. 5, May 2005.

[77] R. L. Ives and G. Miram, "Improved Cathodes for High Frequency RF Devices," in *Proc. of the International Conference on Infrared and Millimeter Waves*, Williamsburg, VA 2005.

[78] Sh. E. Tsimring, "Gyrotron electron beams: velocity spread and energy spread and beam instabilities," *Int. J. Infrared and Millimeter Waves*, v. 22, no. 10, Oct. 2001.

[79] ICEM CFD Engineering Homepage (2005, Nov.). [Online]. Available: http://www.ansys.com/products/icemcfd.asp.

[80] C. Liu, T. M. Antonsen Jr., B. Levush, "Simulation of the Velocity Spread in Magnetron Injection Guns," *IEEE Trans. Plasma Sci.* v. 24, no. 3, June 1996.

[81] W. C. Guss, M. A. Basten, K. E. Kreischer, and R. J. Temkin, "Velocity spread measurements on a magnetron injection gun beam," *J. Appl. Phys.*, v. 76, no. 6 September 1994.

[82] B. Piosczyk, *Proc. SPIE,* v. 2104, 450, 1993

[83] E. G. Avdoshin, L. V. Nikolaev, I. N. Platonov, and Sh. E. Tsimring, *Radiophys. Quantum Electron.* v. 16, no. 461, 1973.

[84] W. C. Guss, T. L. Grimm, K. E. Kreischer, J. T. Polevoy, and R. J. Temkin, "Velocity ratio measurements of a gyrotron electron beam," *J. Appl. Phys.*, v. 69, no. 7, April 1991.

[85] J. P. Calame, J. Cheng, B. Hogan, W. Lawson, C. D. Striffler, P. E. Latham, and V. Irwin, "Measurements of Velocity Ratio in a 90 MW Gyroklystron Electron Beam," *IEEE Trans. Plasma Sci.*, v. 22, no. 4, August 1994.

[86] R. P. Fischer and A. W. Fliflet, "Velocity Ratio Measurements on a 20-60 kV Quasi-Optical Gyrotron Electron Beam," *IEEE Trans. Plasma Sci.*, v. 28, no. 3, June 2000.

[87] Tricomp 2D Simulation Suite, Field Precision Inc. 2004, www.fieldp.com.

[88] Maxwell 2D Student Version, Ansoft Inc., 2005, http://www.ansoft.com/products/em/max2d/.

[89] E.M. Choi, C. Marchewka, I. Mastovsky, M. A. Shapiro, J. R. Sirigiri, and R. J. Temkin, "Megawatt Power Level 120 GHz Gyrotrons for ITER Start-Up," *Journal of Physics: Conference Series, Third IAEA Technical Meeting on ECRH Physics and Technology in ITER*, v. 25, 1-7, 2005.

[90] I. Gorelov, J. M. Lohr, D. Ponce, R. W. Callis, H. Ikezi, R. A. Legg, and S. E. Tsimring, "Gyrotron Performance on the 110 GHz Installation at the DIII-D Tokamak," in *Proc. of 24th International Conference on Infrared and Millimeter Waves*, Monterey, CA, September 1999.

[91] B. Piosczyk, A. Arnold, G. Dammertz, O. Dumbrajs, M. Kuntze, and M. K. Thumm, "Coaxial Cavity Gyrotron—Recent Experimental Results," *IEEE Trans. Plasma Sci.*, v. 30, no. 3, June 2002.

[92] P. V. Krivosheev, V. K. Lygin, V. N. Manuilov, "Numerical Simulation of the Dynamic Processes in the Gyrotron Adiabatic Trap." in *proc. of the International University Conference "Electronics and Radiophysics of Ultra-High Frequencies,"* Saint-Petersburg, May 1999.

[93] C. Liu and T. M. Antonsen, "Implication of DC-space-charge-induced velocity spread on gyrotron gun performance," *IEEE Trans. Plasma Sci.*, v. 26, no. 3, pp. 825-834, June 1998.

[94] Sh. E. Tsimring and V. E. Zapevalov, "Experimental Study of intense helical electron beams with trapped electrons," *Int. J. Electronics*, v. 81, no. 2, pp. 199-205, 1996.

[95] A. N. Kuftin and V. E. Zapevalov, "Experimental Study of Trapped Electrons Influence on the Helical Electron Beam Parameters for Millimeter Wave Range Gyrotrons," in *Proc. of the 12th Int. Conf. on "High-Power Particle Beams,"* v. 2, pp. 780-783, Haifa, Israel, 1998.

[96] D. V. Borzenkov and O. I. Luksha, "Numerical simulation of space-charge dynamics in a gyrotron trap," *Tech. Phys.*, v. 42, no. 9, September 1997.

[97] O. I. Louksha, G. G. Sominski, D. V. Kas'yanenko, "Experimental Study and Numerical Simulation of Electron Beam in Gyrotron-Type Electron-Optical System," in *Proc. Int. University Conf. "Electronics and Radiophysics of Ultra-High Frequencies"*, St. Petersburg, Russia, pp.130-133, May 1999.

[98] D. V. Kas'yanenko, O. I. Louksha, B. Piosczyk, G. G. Sominsky, and M. Thumm, "Low-Frequency Parasitic Space-Charge Oscillations in the Helical Electron Beam of a Gyrotron," *Radiophysics and Quantum Electronics*, v. 47, no. 5-6, 2004.